

UNCLASSIFIED

AD NUMBER

AD367907

CLASSIFICATION CHANGES

TO: unclassified

FROM: confidential

LIMITATION CHANGES

TO:

Approved for public release, distribution unlimited

FROM:

Distribution: DoD only: others to Naval Research Lab., Washington, D. C. 20390.

AUTHORITY

May 1969, Group-4, DoDD 5200.10; NRL ltr, 26 Feb 2001.

THIS PAGE IS UNCLASSIFIED

CONFIDENTIAL

367907
206298

SUMMARY OF NAVY STUDY PROGRAM
FOR
F4H-1 and F8U-3 WEAPON SYSTEMS
(Appendices to NRL Memo Report 754)

VOLUME II

DEC 17 1965
RECEIVED
NSA

Equipment Research Branch
Radar Division
Naval Research Laboratory

DOWNGRADED AT 3-YEAR INTERVALS
DECLASSIFIED AFTER 12 YEARS
DOD DIR 5200.10

CONFIDENTIAL

4. "DOC AVAILABILITY NOTICE" - This document contains information on how to obtain copies of this document. Other qualified users should contact the Director, Naval Research Laboratory, Washington, D. C., 20340.

SECURITY

This document contains information affecting the national defense of the United States within the meaning of the Espionage Laws, Title 18, U.S.C., Sections 793 and 794. The transmission or the revelation of its contents in any manner to an unauthorized person is prohibited by law.

CONFIDENTIAL



APPENDIX 'I'

NAVY MISSILE STUDY TECHNICAL REPORT #1

FILE-1 STABILITY DERIVATIVES (WIND AND BODY AXES) AND
DYNAMIC CHARACTERISTICS

(90114)

(PROPRIETARY INFORMATION)

(MCDONNELL AIRCRAFT CO.)

4-24/1m

by
R. B. Tucker
5/1/57

CONFIDENTIAL



TABLE OF CONTENTS

	<u>Page</u>
I. Synopsis	3
II. Description of F4H-1	3
III. Basic Aircraft Data	3
<u>Appendix I.</u>	10
<u>Appendix II.</u>	14
References	20

**I. SYNOPSIS**

This memorandum contains basic aircraft data for the F4H-1. The stability derivatives of the F4H-1 in both wind axes and body axes are presented along with the airplane characteristics for both the lateral and longitudinal modes. A brief description of the F4H-1 is also given.

II. DESCRIPTION OF F4H-1

The F4H-1 is a two-seat, high performance, all-weather fighter that is powered by two General Electric J79-GE-2 or -3 turbo jet engines with after-burners. It is capable of attaining high supersonic speeds and high altitudes. The basic armament that the F4H-1 will carry are four Sparrow III missiles, but it is also capable of carrying a variety of external stores. The F4H-1 has thin, highly swept wings of low aspect ratio, and thin swept tail surfaces.

III. BASIC AIRCRAFT DATA

The stability derivatives were obtained for six different flight conditions. They were for both maximum speed and cruise speed of the F4H-1 at altitudes of 1,000 ft., 30,000 ft., and 50,000 ft. Figure 1 gives the speed profile for the F4H-1. The velocities in the speed profile which were used in obtaining the stability derivatives will be indicated by cross marks.

The stability derivatives in wind axes are presented in Table I. Also included in this table are the airplane characteristics for both the lateral and longitudinal stick-fixed modes. Table II contains the stability derivatives in body axes. There were several coefficients for which either the data available was insufficient, or no data at all was available. These coefficients will be indicated in the tables.

In Appendix I, the force or moment equations are given from which the wind axes stability derivatives were derived. With each equation a reference is given to show where each coefficient was obtained. Also included in this Appendix are the equations of motion in wind and body axes form.

The pertinent angles of the F4H-1 are shown in Figure 2.

In appendix 2, the performance functions of the lateral and longitudinal variables as influenced by δ_e , δ_a , and δ_r are given. The method of obtaining these performance functions is also given.



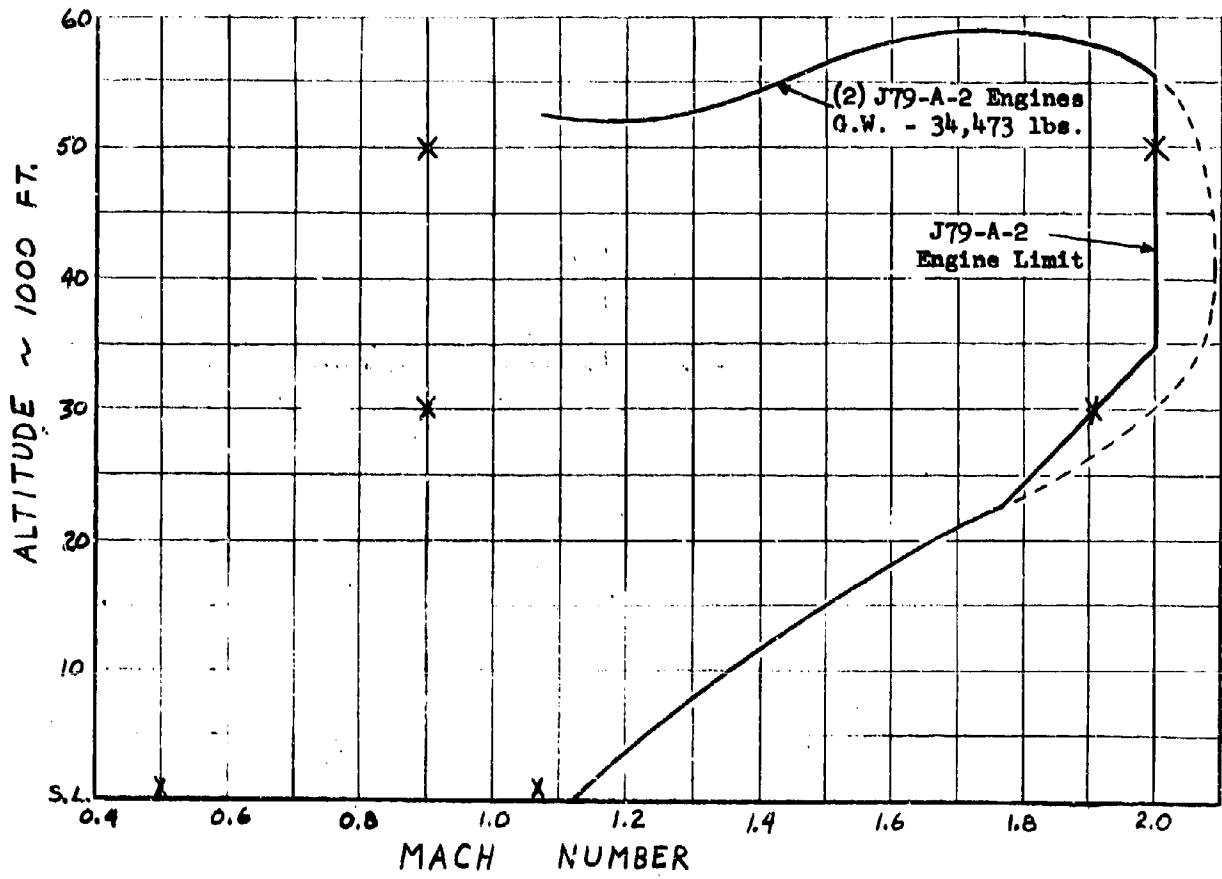
MODEL F4H-1

V_{max} vs. Altitude

G. W. = 35,000 lbs.

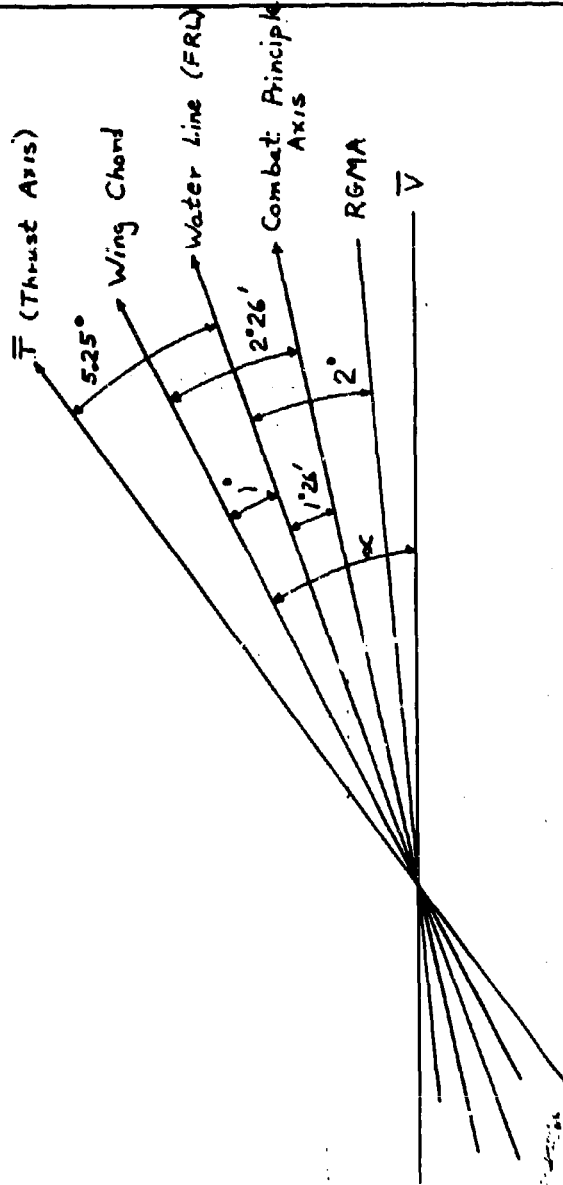
VERY PRELIMINARY

Clean + (4) Sparrow JET's



X - Indicates points at which Stability Derivatives were evaluated.

Figure I



α = Aerodynamic angle of attack

$\alpha_p = \alpha_w - 2^\circ 26'$

where α_p is angle of attack about combat principle axis line

Figure 2



TABLE I

FIG-1 LATERAL STABILITY DERIVATIVES - WIND AXES

Altitude (ft.)	1,000	30,000	50,000	1,000	30,000	50,000
Mach No.	1.07	1.91	2.00	0.50	0.90	0.90
C_L	.040	.041	.096	.183	.183	.473
Velocity (ft/sec)	1188.77	1896.63	1940.0	555.5	893.7	873.0
I_x (slug ft ²)	22,225	22,172	22,135	22,156	22,131	22,796
I_y (slug ft ²)	102,437	102,437	102,437	102,437	102,437	102,437
I_z (slug ft ²)	117,661	117,714	117,751	117,730	117,755	117,090
I_{xz} (slug ft ²)	3,062	2,080	- 875	-1,668	- 609	-7,972
q (lbs/ft ²)	1631.5	1599	679.3	356.3	355	137.6
λ_p	-3.4023	-1.7384	-0.97053	-2.3074	-1.5571	-0.65906
λ_r	+0.73837	+0.47991	+0.25901	+0.55649	+0.36263	+0.22932
λ_β	-19.347	+48.522	+12.886	-14.813	-16.912	-10.978
λ_{δ^*}	-89.461	-27.915	-11.274	-17.963	-21.868	-8.2261
λ_{δ^a}	+3.9890	+3.1849	+1.9675	+1.9864	+2.3572	+0.14736
n_p	+0.07183	+0.05818	+0.02510	-0.02872	-0.02226	-0.02692
n_r	-0.52416	-0.45337	-0.21265	-0.22351	-0.15753	-0.06679
n_β	+20.310	+18.011	+9.6069	+6.7757	+6.6452	+3.1376
n_{δ^*}	0	0	0	0	0	0
n_{δ^a}	-2.7176	-2.3443	-1.8833	-4.1817	-3.5791	-1.5960
y_p	+0.00016	+0.00005	+0.00005	0	0	0
y_r	+0.00286	+0.00119	+0.00054	+0.00287	+0.00124	+0.00054
y_β	-0.42365	-0.25546	-0.10908	-0.18435	-0.13050	-0.05377
y_{δ^*}	-0	0	0	0	0	0
y_{δ^a}	+0.01049	+0.00478	+0.00387	+0.03356	+0.01732	+0.00790
Roll Time Constant	0.29 sec	0.56	1.10	0.42	0.61	1.39
Spiral " "	- 523 sec	- 65	-110	-639	+1240	+5,562
Dutch Roll - %	10.1%	7.7%	4.9%	6.4%	3.7%	2.1%
ω_n (rad/sec)	4.49	4.36	3.09	2.68	2.62	2.00

b



TABLE I (Cont.)

FIG-1 LONGITUDINAL STABILITY DERIVATIVES - WIND AXES

Altitude Velocity (ft/sec)	1,000	30,000	50,000	1,000	30,000	50,000
	1188.77	1896.63	1940.0	555.5	893.7	873.0
$m_{\dot{q}}$	-3.3017	-1.2585	-0.18305	-1.2266	-0.88949	-0.35283
$m_{\dot{\omega}}$	-1.5731	-0.10113	-0.01900	-0.6197	-0.47387	-0.21294
$m_{\dot{\alpha}}$	-128.17	-109.68	-13.663	-8.2835	-11.675	-4.5237
$m_{\dot{\beta}}$	-4.8774	+5.0156	+3.0163	-0.20709	-3.9800	-2.9701
$m_{\dot{\delta}_a}$	-107.13	-60.866	-24.502	-19.901	-21.843	-8.1636
l_q	+0.01781	+0.00300	+0.00112	+0.01280	+0.00566	+0.00230
$l_{\dot{\omega}}$	+2.9617	+1.0696	+0.11749	+1.0352	+0.79088	+0.31372
$l_{\dot{u}}$	-0.02985	+0.00333	+0.01177	+0.12235	+0.12546	+0.11651
$l_{\dot{\delta}_e}$	+0.41782	+0.13848	+0.05365	+0.14294	+0.11081	+0.04396
$d_{\dot{\omega}}$	+0.05520	+0.04122	+0.04195	+0.05818	+0.04646	+0.04763
$d_{\dot{u}}$	+0.10277	+0.03833	+0.01710	+0.00414	+0.00346	+0.01204
$d_{\dot{\delta}_e}$	0	0	0	0	0	0
Short Period						
τ_1 (sec)	33.5%	11.5%	7.2%	46.8%	30.8%	21.1%
τ_2 (sec)	11.6	10.5	6.6	3.1	3.5	2.2
Phugoid						
T_1 (sec)	7.7				13.2	15.1
T_2 (sec)	-35.5				15.4	20.6
ζ						
$\zeta_{\dot{u}}$ (rad/sec)		67.6%	38.5%	1.3%		
		.030	.026	.070		

NOTE: Combat weight at 60% fuel plus 4 Sparrow III missiles, e.g. 30% M.A.C. = 34,500 lbs.
 * Definition of $l_{\dot{\delta}_a}$: Aileron defined as 1° of down going aileron yields 1.5° up going spoiler.

** No data was available.

*** Only data available was with $\alpha = 0^\circ$.



TABLE II
F4U-1 Lateral Stability Derivatives - Body Axes (Principal Axis)

	1,000	30,000	50,000	1,000	30,000	50,000	1,000	30,000	50,000
Altitude (ft)									
Each No.	1.07	1.91	2.00	0.50	0.90	0.90	0.90	0.90	0.90
Velocity (ft/sec)	1188.77	1896.63	1940.0	555.5	393.7	393.7	873.0	873.0	873.0
α (deg)	-1.8361	-1.2761	+0.5211	+1.000	+0.365	+0.365	+4.799	+4.799	+4.799
γ (deg)	0	0	0	0	0	0	0	0	0
D, lbs.	34,588	29,915	13,322	4,313	4,478	4,478	4,520	4,520	4,520
I_x slug ft ²	22,127	22,127	22,127	22,127	22,127	22,127	22,127	22,127	22,127
I_y slug ft ²	117,759	117,759	117,759	117,759	117,759	117,759	117,759	117,759	117,759
I_z slug ft ²	102,437	102,437	102,437	102,437	102,437	102,437	102,437	102,437	102,437
xu	-0.10556	-0.03944	-0.01679	-0.00231	-0.00263	-0.00263	-0.00357	-0.00357	-0.00357
xw	-0.12044	-0.04705	-0.02170	+0.01513	+0.00538	+0.00538	+0.01566	+0.01566	+0.01566
xq	-0.67850	-0.12365	+0.01995	+0.12109	+0.03222	+0.03222	+0.16785	+0.16785	+0.16785
$x\dot{\alpha}$	-15.917	-5.7134	+0.95233	+1.3861	+0.53087	+0.53087	+3.2105	+3.2105	+3.2105
yv	-0.42368	-0.25548	-0.10909	-0.18436	-0.13951	-0.13951	-0.05378	-0.05378	-0.05378
yp	+0.65566	+0.14986	+0.09383	-0.02783	-0.00708	-0.00708	-0.03911	-0.03911	-0.03911
yr	+3.3807	+2.2534	+1.0410	+1.5943	+1.1121	+1.1121	+0.46940	+0.46940	+0.46940
$y\dot{\alpha}$	+12.476	+9.0574	+7.5052	+18.869	+15.485	+15.485	+6.8966	+6.8966	+6.8966
$z\dot{\alpha}$	0	0	0	0	0	0	0	0	0
$z\ddot{\alpha}$	-2.9862	-1.0833	-0.42122	-1.0415	-0.49644	-0.49644	-0.32702	-0.32702	-0.32702
zu	-0.08246	-0.02613	-0.00809	-0.10419	-0.12039	-0.12039	-0.09021	-0.09021	-0.09021
zq	-21.165	-5.6834	-2.1806	-7.1089	-5.9579	-5.9579	-1.9993	-1.9993	-1.9993
$z\dot{\alpha}$	-496.51	-262.61	-104.09	-79.401	-99.043	-99.043	-38.244	-38.244	-38.244



TABLE II (cont.)

F4E-1 Longitudinal Stability Derivatives - Body Axes

Altitude (ft)	1,000	30,000	50,000	1,000	30,000	50,000
Velocity (ft/sec)	1188.77	1896.63	1940.0	555.5	893.7	873.0
l_y	-0.01343	+0.02673	+0.00640	-0.02783	-0.01918	-0.0150
l_p	-3.3808	-1.7250	-0.97448	-2.3172	-1.5589	-0.63454
l_r	+0.76068	+0.46594	+0.26054	+0.53753	+0.35810	+0.20846
l_{sa}	-89.818	-27.968	-11.278	-17.985	-21.873	-8.4460
l_{sr}	+3.5417	+2.9194	+2.0599	+2.3774	+2.4794	+0.85778
m_y	-0.00756	+0.00140	+0.00178	-0.0011	-0.00437	-0.00296
m_p	-0.10763	-0.05787	-0.02249	-0.01492	-0.01309	-0.00545
m_r	-0.00132	-0.00005	-0.00003	-0.00112	-0.00053	-0.00024
m_{sa}	-0.00004	0	0	+0.00002	0	+0.00002
m_{sr}	-3.3017	-1.2585	-0.48305	-1.2266	-0.88949	-0.35283
n_y	+0.01716	+0.00939	+0.00496	+0.01211	+0.00741	+0.00336
n_p	+0.07535	+0.05535	+0.02327	-0.03241	-0.02313	-0.03200
n_r	-0.53061	-0.45636	-0.21196	-0.22219	-0.15724	-0.06537
n_{sa}	+0.54091	+0.11460	-0.01948	-0.05902	-0.02636	-0.13351
n_{sr}	-2.7384	-2.3562	-1.8800	-4.1737	-3.5761	-1.5792

Note: (1) Combat weight at 60 percent fuel plus 4 Sparrow III missiles, c.g. 30 percent M.A.C. = 34,500 lbs.

(2) All angles are measured in radians.

(3) All velocities are measured in ft/sec.



APPENDIX I

This appendix includes the force and moment equation from which the wind axes stability derivatives were obtained. These are given in Table III. Also given in the table is a reference as to where each coefficient required by these force and moment equations was obtained.

The equations of motion in terms of wind axes and in terms of body axes are also included.

TABLE III
CALCULATION OF STABILITY DERIVATIVES (WIND AXES)

LATERAL

Coefficient	Force and Moment Equation	Units	Reference for FlH-1 Coefficient
$C_{L\beta}$	$L_{\beta} = C_{L\beta} sqb$	lb.ft./rad	Ref. 1, pages 10.10, 11, 12
$C_{L\delta_a}$	$L_{\delta_a} = C_{L\delta_a} sqb$	lb.ft./rad	Ref. 1, pages 10.16, 17
$C_{L\delta_r}$	$L_{\delta_r} = C_{L\delta_r} sqb$	lb.ft./rad	Ref. 1, pages 15.19, 20
$C_{N\beta}$	$N_{\beta} = C_{N\beta} sqb$	lb.ft./rad	Ref. 1, pages 11.7, 8, 9
$C_{N\delta_a}$	$N_{\delta_a} = C_{N\delta_a} sqb$	lb.ft./rad	-
$C_{N\delta_r}$	$N_{\delta_r} = C_{N\delta_r} sqb$	lb.ft./rad	Ref. 1, page 11.15
$C_{Y\beta}$	$Y_{\beta} = C_{Y\beta} sq$	lb./rad	Ref. 1, page 11.13
$C_{Y\delta_a}$	$Y_{\delta_a} = C_{Y\delta_a} sq$	lb./rad	-
$C_{Y\delta_r}$	$Y_{\delta_r} = C_{Y\delta_r} sq$	lb./rad	Ref. 1, page 15.21
C_{L_p}	$L_p = C_{L_p} sqb^2/2v$	lb.ft.sec./rad.	Ref. 2, page 17.11
C_{L_r}	$L_r = C_{L_r} sqb^2/2v$	lb.ft.sec./rad.	Ref. 1, pages 15.13, 14, 15
C_{N_p}	$N_p = C_{N_p} sqb^2/2v$	lb.ft.sec./rad.	Ref. 1, pages 15.24, 25
C_{N_r}	$N_r = C_{N_r} sqb^2/2v$	lb.ft.sec./rad.	Ref. 1, page 15.22
C_{Y_p}	$Y_p = C_{Y_p} sqb/2v$	lb.sec./rad.	Ref. 1, page 15.26, 27
C_{Y_r}	$Y_r = C_{Y_r} sqb/2v$	lb.sec./rad.	Ref. 1, page 15.23



TABLE III (Cont.)

LONGITUDINAL

Coefficient	Force and Moment Equation	Unit	Reference for F4H-1 Coefficient
$C_{m_{\dot{\alpha}}}$	$M_{\dot{\alpha}} = C_{m_{\dot{\alpha}}} s q \bar{c}$	lb.ft./rad	Ref. 1, page 9.17
C_{m_u}	$M_u = C_{m_u} s q \bar{c}$	lb.ft./rad.	Ref. 1, page 15.4
$C_{m_{\dot{\delta}_e}}$	$M_{\dot{\delta}_e} = C_{m_{\dot{\delta}_e}} s q \bar{c}$	lb.ft./rad	Ref. 1, page 9.24
C_{m_q}	$M_q = C_{m_q} s q \bar{c}^2 / 2V$	lb.ft.sec./rad	Ref. 1, page 15.2
$C_{m_{\dot{\alpha}}}$	$M_{\dot{\alpha}} = C_{m_{\dot{\alpha}}} s q \bar{c}^2 / 2V$	lb.ft.sec./rad	Ref. 1, page 15.8
$C_{L_{\dot{\alpha}}}$	$L_{\dot{\alpha}} = C_{L_{\dot{\alpha}}} s q$	lb./rad.	Ref. 1, page 8.33
$C_{L_{\dot{\delta}_e}}$	$L_{\dot{\delta}_e} = C_{L_{\dot{\delta}_e}} s q$	lb./rad.	Ref. 1, page 9.23
C_{L_u}	$L_u = C_{L_u} s q$	lb./rad.	Ref. 1, page 15.6
C_{L_p}	$L_p = C_{L_p} s q \bar{c} / 2V$	lb.sec./rad	Ref. 1, page 15.10
$C_{D_{\dot{\alpha}}}$	$D_{\dot{\alpha}} = C_{D_{\dot{\alpha}}} s q$	lb./rad	Ref. 1, page 15.7
$C_{D_{\dot{\delta}_e}}$	$D_{\dot{\delta}_e} = C_{D_{\dot{\delta}_e}} s q$	lb./rad	-
C_{D_u}	$D_u = C_{D_u} s q$	lb./rad	Ref. 1, page 15.3

For the F4H-1, the remaining unknowns in the force and moment equations of Table III had the following value:

$s = 530 \text{ sq. ft.}$ $b = 38.4 \text{ ft.}$ $\bar{c} = 16.05 \text{ ft.}$

It should be pointed out that the stability derivatives obtained from the force and moment equations in Table III will not have the same value as the values given in Table I. To obtain the values in Table I, it is necessary to divide the above force or moment equations by its respective moment of inertia or by mV .

For the lateral equation of motion, this could be illustrated as follows:

Let

$$\frac{L_p}{I_x} = l_p$$

$$\frac{N_p}{I_z} = n_p$$



$$\frac{Y_p}{mV} = y_p$$

$$\frac{I_{x\dot{x}}}{I_x} = i_{x\dot{x}}$$

$$\frac{I_{x\dot{y}}}{I_x} = i_{\dot{y}x}, \text{ and so on.}$$

Similarly for the longitudinal equations, let

$$\frac{M_\alpha}{I_y} = m_\alpha$$

$$\frac{L_f}{mV} = l_f$$

$$\frac{D_u}{mV} = d_u, \text{ and so on.}$$

In the case of wind axes the equations of motion will be written first with the stability derivatives in the form given in Table III and secondly with the stability derivatives in the form of Table I, where the substitutions using the above equations have been made.

Given below are the equations of motion in terms of wind axis.

LATERAL

Roll: $(s^2 - \frac{L_p}{I_x} s) \phi + (-\frac{I_{xz}}{I_x} s^2 - \frac{L_r}{I_x} s) \psi - \frac{L_\beta}{I_x} \beta - \frac{L_{\dot{\alpha}}}{I_x} \dot{\alpha} - \frac{L_{\dot{\gamma}}}{I_x} \dot{\gamma} = 0$

or $(s^2 - l_p s) \phi + (-i_{xz} s^2 - l_r s) \psi - l_\beta \beta - l_{\dot{\alpha}} \dot{\alpha} - l_{\dot{\gamma}} \dot{\gamma} = 0$

Yaw: $(-\frac{I_{yz}}{I_y} s^2 - \frac{N_p}{I_y} s) \phi + (s^2 - \frac{N_r}{I_y}) \psi - \frac{N_\beta}{I_y} \beta - \frac{N_{\dot{\alpha}}}{I_y} \dot{\alpha} - \frac{N_{\dot{\gamma}}}{I_y} \dot{\gamma} = 0$

or $(-i_{yx} s^2 - n_p s) \phi + (s^2 - n_r) \psi - n_\beta \beta - n_{\dot{\alpha}} \dot{\alpha} - n_{\dot{\gamma}} \dot{\gamma} = 0$

Side Force: $(-\frac{Y_p}{mV} s - \frac{g}{V}) \phi + (1 - \frac{Y_r}{mV}) s \psi + (s - \frac{Y_\beta}{mV}) \beta - \frac{Y_{\dot{\alpha}}}{mV} \dot{\alpha} - \frac{Y_{\dot{\gamma}}}{mV} \dot{\gamma} = 0$

or $(-y_p s - g_V) \phi + (1 - y_r) s \psi + (s - y_\beta) \beta - y_{\dot{\alpha}} \dot{\alpha} - y_{\dot{\gamma}} \dot{\gamma} = 0$



LONGITUDINAL

Pitch: $(s^2 - \frac{M_p + M_k}{I_y} s - \frac{M_k}{I_y}) \alpha + (s^2 - \frac{M_k}{I_y} s) \gamma - \frac{M_u}{I_y} u - \frac{M \delta_a}{I_y} = 0$

or $(s^2 - (m_p + m_k) s - m_k) \alpha + (s^2 - m_k s) \gamma - m_u u - m_{\delta_a} \delta_a = 0$

Lift: $(-\frac{l_p}{mV} s - \frac{l_w}{mV}) \alpha + (1 - \frac{l_q}{mV}) s \gamma - \frac{l_u}{mV} u - \frac{l_{\delta_e}}{mV} \delta_e = 0$

or $(-l_p s - l_w) \alpha + (1 - l_q) s \gamma - l_u u - l_{\delta_e} \delta_e = 0$

Drag: $+\frac{D_u}{mV} \alpha + (\frac{D}{V}) \gamma + (s + \frac{D_u}{mV}) u + \frac{D_{\delta_e}}{mV} \delta_e = 0$

or $d_u \alpha + \frac{D}{V} \gamma + (s + d_u) u + d_{\delta_e} \delta_e = 0$

The six equations of motion in body axis terms are listed below:

1) $\dot{u} + wq - vr = x_u u + x_w (W - W_0) + x_p p + x_{\delta_e} \delta_e + \frac{F_x}{m} - g \sin \theta$

2) $\dot{v} + ur - wp = y_v v + y_p p + y_r r + y_{\delta_e} \delta_e + g \cos \theta \sin \phi$

3) $\dot{w} + vp - uq = z_u u + z_w (W - W_0) + z_p p + z_{\delta_e} \delta_e + g \cos \theta \cos \phi$

4) $\dot{p} + (\frac{I_y - I_z}{I_x}) qr = l_v v + l_p p + l_r r + l_{\delta_a} \delta_a + l_{\delta_r} \delta_r$

5) $\dot{q} + (\frac{I_x - I_z}{I_y}) rp = m_u (u - u_0) + m_w (W - W_0) + m_{\dot{w}} \dot{w} + m_p p + m_{\delta_e} \delta_e$

6) $\dot{r} + (\frac{I_y - I_x}{I_z}) pq = n_v v + n_p p + n_r r + n_{\delta_a} \delta_a + n_{\delta_r} \delta_r$



APPENDIX II

This appendix includes the performance functions of the lateral and longitudinal variables influenced by δ_e , δ_r , and δ_a . These quantities define the dynamic relationship of the aircraft variables, i.e.

Longitudinal:

$$\Theta = \{ [PF]_{\alpha, \delta_e} + [PF]_{\gamma, \delta_e} \} \delta_e$$

$$u = [PF]_{u, \delta_e} \delta_e$$

Lateral:

$$\beta = [PF]_{\beta, \delta_r} \delta_r + [PF]_{\beta, \delta_a} \delta_a$$

$$\gamma = [PF]_{\gamma, \delta_r} \delta_r + [PF]_{\gamma, \delta_a} \delta_a$$

$$\phi = [PF]_{\phi, \delta_r} \delta_r + [PF]_{\phi, \delta_a} \delta_a$$

Before listing the values of the performance functions for the F4U-1, the method of obtaining [PF] will be explained.

For the longitudinal case, we refer back to the longitudinal wind axes equations of motion given in Appendix I. We could write these three equations as

α	γ	u	δ_e	
$s^2 - (m_z + m_{\alpha})s - m_{\alpha}$	$s^2 - m_{\gamma}s$	$-m_u$	$-m_{\delta_e}$	$= 0$
$-l_{\dot{\gamma}}s - l_{\alpha}$	$(1 - l_{\dot{\gamma}})s$	$-l_u$	$-l_{\delta_e}$	$= 0$
d_{α}	$\frac{g}{V}$	$s + d_u$	$+d_{\delta_e}$	$= 0$

For a δ_e input to the system, we can rewrite above as

α	γ	u	
$s^2 - (m_z + m_{\alpha})s - m_{\alpha}$	$s^2 - m_{\gamma}s$	$-m_u$	$= m_{\delta_e} \delta_e$
$-l_{\dot{\gamma}}s - l_{\alpha}$	$(1 - l_{\dot{\gamma}})s$	$-l_u$	$= l_{\delta_e} \delta_e$
d_{α}	$\frac{g}{V}$	$s + d_u$	$= -d_{\delta_e} \delta_e$

Using Cramer's rule, we can solve above for an α response to a δ_e input. We would have



$$\alpha = \frac{\begin{vmatrix} m_{\delta_e} \delta_e & s^2 - m_f s & -m_u \\ l_{\delta_e} \delta_e & (1 - l_p) s & -l_u \\ -d_{\delta_e} \delta_e & g_V & s + d_u \end{vmatrix}}{\begin{vmatrix} s^2 - (m_f + m_{\delta_e}) s - m_{\alpha} & s^2 - m_f s & -m_u \\ -l_p s - l_{\alpha} & (1 - l_p) s & -l_u \\ d_{\alpha} & g_V & s + d_u \end{vmatrix}}$$

The denominator of the above is known as the stick fixed characteristic equation and will be abbreviated as Δ .

We can rewrite above equation as

$$\frac{\alpha}{\delta_e} = \frac{\begin{vmatrix} m_{\delta_e} & s^2 - m_f s & -m_u \\ l_{\delta_e} & (1 - l_p) s & -l_u \\ -d_{\delta_e} & g_V & s + d_u \end{vmatrix}}{\Delta} = \frac{N_{\alpha, \delta_e}}{\Delta}$$

where $[PF]_{\alpha, \delta_e} = \frac{\alpha}{\delta_e} = \frac{N_{\alpha, \delta_e}}{\Delta}$

Similarly, $[PF]_{\gamma, \delta_e}$ and $[PF]_{u, \delta_e}$ may be solved for.

The lateral performance functions may be derived in a similar manner, i.e.

$$\beta = \frac{\begin{vmatrix} s^2 - l_p s & -i_{x\beta} s^2 - l_r s & l_{\delta_a} \delta_a + l_{\delta_r} \delta_r \\ -i_{z\beta} s^2 - n_p s & s^2 - n_r s & n_{\delta_a} \delta_a + n_{\delta_r} \delta_r \\ -y_p s - g_V & (1 - y_r) s & y_{\delta_a} \delta_a + y_{\delta_r} \delta_r \end{vmatrix}}{\begin{vmatrix} s^2 - l_p s & -i_{x\beta} s^2 - l_r s & -l_p \\ -i_{z\beta} s^2 - n_p s & s^2 - n_r s & -n_p \\ -y_p s - g_V & (1 - y_r) s & s - y_p \end{vmatrix}}$$

or



$$\beta = \frac{\delta_a \begin{vmatrix} s^2 - l_p s & -i_{x\beta} s^2 - l_r s \\ -i_{\beta x} s^2 - n_p s & s^2 - n_r s \\ -y_p s - \mathcal{N} & (1 - y_r) s \end{vmatrix}}{\Delta} + \frac{\delta_r \begin{vmatrix} s^2 - l_p s & -i_{x\beta} s^2 - l_r s & l_{\beta r} \\ -i_{\beta x} s^2 - n_p s & s^2 - n_r s & n_{\beta r} \\ -y_p s - \mathcal{N} & (1 - y_r) s & y_{\beta r} \end{vmatrix}}{\Delta}$$

$$\beta = [PF]_{\beta \delta_a} \delta_a + [PF]_{\beta \delta_r} \delta_r = \frac{N_{\beta \delta_a} \delta_a}{\Delta} + \frac{N_{\beta \delta_r} \delta_r}{\Delta}$$

The remaining lateral performance functions may be obtained in the same manner.

The performance functions for the F4H-1 for the six flight conditions considered will now be listed:

Case I; $V_p = 1188.77$ fps at 1,000 ft.

Longitudinal

$$\begin{aligned} \Delta &= (s + 0.1292) (s - 0.0282) (s^2 + 7.8108 s + 135.7) \\ N_{u, \delta_a} &= -0.4178 (s - 0.0116) (s + 255.2) (s + 0.1144) \\ N_{y, \delta_a} &= +0.4178 (s + 0.1039) (s + 25.28) (s - 24.97) \\ N_{u, \delta_e} &= +0.01176 (s + 499.0) (s + 1.217) \end{aligned}$$

Lateral

$$\begin{aligned} \Delta &= +0.9964s (s + 3.429) (s - 0.0019) (s^2 + 0.5077s + 20.12) \\ N_{\phi, \delta_a} &= +2.281s (s + 2.015) (s - 0.2762) \\ N_{\phi, \delta_r} &= +0.0105 s (s + 0.00025) (s + 249.96) (s + 3.464) \\ N_{\psi, \delta_a} &= -2.329 (s + 4.078) (s^2 + 0.8949s + 5.178) \\ N_{\psi, \delta_r} &= -2.6138 (s - 0.1623) (s + 3.401) (s + 0.5334) \\ N_{\phi, \delta_a} &= -89.461s (s^2 + 0.9478s + 20.47) \\ N_{\phi, \delta_r} &= +3.6145s (s^2 + 0.3989 s + 7.870) \end{aligned}$$

Case II; $V_p = 1896.63$ fps at 30,000 ft.



Longitudinal

$$\Delta = (s^2 + 0.0402s + 0.00088) (s^2 + 2.427s + 110.7)$$

$$N_{\alpha, \delta_e} = -0.1385 (s + 0.0084) (s + 439.5) (s + 0.0299)$$

$$N_{\gamma, \delta_e} = +0.1385 (s + 0.0376) (s + 19.01) (s - 18.96)$$

$$N_{u, \delta_e} = +0.0034 (s + 746.4) (s + 0.3377)$$

Lateral

$$\Delta = +0.9983s (s + 1.776) (s - 0.0154) (s^2 + 0.6761s + 19.03)$$

$$N_{\beta, \delta_a} = +0.4913s (s + 2.511) (s - 0.1740)$$

$$N_{\rho, \delta_r} = +0.00477s (s + 0.0014) (s + 479.4) (s + 1.721)$$

$$N_{\gamma, \delta_a} = -0.4933 (s^3 + 3.5477s^2 + 0.8920s + 17.287)$$

$$N_{\psi, \delta_r} = -2.2880 (s - 0.6379) (s^2 + 2.554s + 1.9886)$$

$$N_{\phi, \delta_a} = -27.915s (s^2 + 0.7088s + 18.11)$$

$$N_{\theta, \delta_r} = +2.965s (s^2 + 0.4440s + 57.72)$$

Case III, $V_T = 1940$ fps at 50,000 ft.

Longitudinal

$$\Delta = (s^2 + 0.0200s + 0.00068) (s^2 + 0.9466s + 43.81)$$

$$N_{\alpha, \delta_e} = -0.05365 (s^2 + 0.0171s + 0.0003) (s + 456.7)$$

$$N_{\gamma, \delta_e} = +0.05365 (s + 0.0147) (s + 12.14) (s - 12.11)$$

$$N_{u, \delta_e} = +0.00136 (s + 755.1) (s + 0.1273)$$

Lateral

$$\Delta = +0.9997s (s + 1.000) (s - 0.0091) (s^2 + 0.3043s + 9.545)$$

$$N_{\beta, \delta_a} = -0.0843s (s^2 - 1.136s + 0.4717)$$

$$N_{\rho, \delta_r} = +0.00387s (s - 0.00063) (s + 490.6) (s + 0.9554)$$

$$N_{\gamma, \delta_a} = +0.0838 (s^2 + 1.180s + 4.819) (s - 4.449)$$

$$N_{\psi, \delta_r} = -1.898 (s - 0.4748) (s^2 + 1.5015s + 0.7944)$$

$$N_{\phi, \delta_a} = -11.274s (s^2 + 0.3217s + 9.625)$$

$$N_{\theta, \delta_r} = +2.042s (s^2 + 0.0988s + 21.14)$$



Case IV; $V_p = 555.5$ fps at 1,000 ft.

Longitudinal

$$\Delta = (s^2 + 0.0018s + 0.0049) (s^2 + 2.876s + 9.449)$$

$$N_{u,\delta} = -0.1429 (s^2 + 0.0041s + 0.0070) (s + 138.7)$$

$$N_{y,\delta} = +0.1429 (s - 0.0031) (s + 11.69) (s - 11.62)$$

$$N_{u,\delta_e} = 0.000038 (s + 30,066) (s + 0.9756)$$

Lateral

$$\Delta = +0.9989s (s + 2.380) (s - 0.0016) (s^2 + 0.3454s + 7.156)$$

$$N_{p,\delta} = -0.2538s (s + 5.972) (s + 0.1534)$$

$$N_{r,\delta} = +0.03392s (s - 0.0110) (s + 123.9) (s + 2.349)$$

$$N_{y,\delta} = +0.2545 (s - 2.408) (s^2 + 4.619s + 11.50)$$

$$N_{y,\delta_r} = -4.2098 (s^3 + 2.4336 s^2 + 0.2955s + 0.6670)$$

$$N_{\delta,\delta} = -17.9638 (s^2 + 0.4079s + 6.797)$$

$$N_{\delta,\delta_r} = +2.301 s (s^2 - 0.8601s - 21.15)$$

Case V; $V_p = 893.7$ fps at 30,000 ft.

Longitudinal

$$\Delta = (s - 0.0755) (s + 0.0650) (s^2 + 2.166s + 12.35)$$

$$N_{u,\delta} = -0.1108 (s^2 + 0.0034s + 0.0038) (s + 196.9)$$

$$N_{y,\delta} = +0.1108 (s - 0.0032) (s + 12.14) (s - 11.88)$$

$$N_{u,\delta_e} = +0.00116 (s + 872.8) (s + 0.5684)$$

Lateral

$$\Delta = +0.99986 s (s + 1.651) (s + 0.0008) (s^2 + 0.1952s + 6.879)$$

$$N_{p,\delta} = -0.1129s (s + 11.18) (s + 0.0982)$$

$$N_{r,\delta} = +0.0173 s (s - 0.0058) (s + 20.72) (s + 1.597)$$

$$N_{y,\delta} = +0.1131 (s - 2.536) (s^2 + 6.972 s + 18.24)$$

$$N_{y,\delta_r} = -3.5913(s^3 + 1.6644 s^2 + 0.1527 s + 0.3234)$$

$$N_{\delta,\delta} = -21.868 s (s^2 + 0.2880 s + 6.658)$$



$$N_{\phi, \delta_r} = +2.4557 s (s - 4.465) (s + 4.098)$$

Case VI; $V_T = 873$ fps at 50,000 ft.

Longitudinal

$$\Delta = (s - 0.0662) (s + 0.0485) (s^2 + 0.9087s + 4.653)$$

$$N_{\alpha, \delta_e} = -0.04396 (s^2 + 0.0120 s + 0.0037) (s + 192.4)$$

$$N_{\gamma, \delta_e} = +0.04396 (s - 0.0045) (s + 7.545) (s - 7.405)$$

$$N_{u, \delta_e} = +0.00047 (s + 849.6) (s + 0.2248)$$

Lateral

$$\Delta = +0.97628 (s + 0.7180) (s + 0.0002) (s^2 + 0.0855s + 4.008)$$

$$N_{\phi, \delta_a} = -0.55978 (s + 0.8966) (s + 0.0403)$$

$$N_{\theta, \delta_r} = +0.00778 (s - 0.0179) (s + 208.2) (s + 0.6856)$$

$$N_{\psi, \delta_a} = +0.5600 (s^2 + 1.505 s + 1.609) (s - 1.055)$$

$$N_{\psi, \delta_r} = -1.606 (s^3 + 0.6921 s^2 + 0.0237s + 0.3914)$$

$$N_{\phi, \delta_a} = -8.2261 s (s^2 + 0.1206s + 3.139)$$

$$N_{\theta, \delta_r} = +0.70558 (s - 5.221) (s + 4.634)$$



REFERENCES

1. McDonnell Report No. 4873, "Stability and Control Data", Confidential.
2. McDonnell Report No. 4518, Volume II, "Fighter Aerodynamic Status Report", Confidential
3. McDonnell Report No. 4518, Volume I, "Fighter Aerodynamic Status Report", Confidential
4. McCourt, A. W., "Aspects of the Linearized Equations of Aircraft Motion Used in Flight Control System Design", Appendix I, page 84. Doctoral Dissertation, University of Pittsburgh, Pittsburgh, Pennsylvania

CONFIDENTIAL



APPENDIX 'I'

Navy Missile Study Technical Report #2

F4H-1 Basic Performance Data

-90114-

**(Proprietary Information
McDonnell Aircraft Co.)**

5/9/57

**R. B. Tucker
5-8/lm**

CONFIDENTIAL



Table of Contents

	<u>Page</u>
I Synopsis	1
II Description of F4H-1	1
III Basic Performance Data	1
References	16



List of Illustrations

<u>Figure</u>		<u>Page</u>
1	Model F4H-1 Maximum Speed Envelope	3
2	Model F4H-1 Airplane Drag Summary.....	4
3	Model F4H-1 Maximum Useable Lift	5
4	Model F4H-1 Mach Number-Load Factor Envelopes at Combat Weight at Altitude, 35,000 feet, with Maximum Power	6
5	Required and Available Thrust versus Mach Number for Different Load Factors; Altitude - 1,000 feet	7
6	Required and Available Thrust versus Mach Number for Different Load Factors; Altitude - 30,000 feet.....	8
7	Required and Available Thrust versus Mach Number for Different Load Factors; Altitude - 50,000 feet.....	9
8	Model F4H-1 Climb Data versus Altitude.....	10
9	Maximum Reheat Net Thrust for (1) General Electric J-79 Engine	12
10	Military Power Net Thrust for (1) General Electric J-79 Engine	13
11	Normal Power Net Thrust for (1) General Electric J-79 Engine	14
12	Intercept Distance versus Bomber Distance from Ship at time of detection	15



I. Synopsis

This report presents some of the basic performance data which are currently available on the F4H-1 aircraft. These data are presented in the form of graphs. A brief description of the F4H-1 is also given.

II. Description of F4H-1

The F4H-1 is a two seat, high performance all-weather fighter designed for intermediate and long range, high altitude interceptions. As its principal armament, it will carry four Sparrow III missiles, but it is also capable of carrying a variety of external stores.

It is powered by two General Electric J79-GE-2 or -3 turbojet engines with afterburners. It has thin highly swept wings of low aspect ratio and thin swept tail surfaces.

III. Basic Performance Data

The aircraft performance data shown in the following figures are for the basic F4H-1 airplane carrying four Sparrow III missiles semi-submerged on the underside of the fuselage. For comparative purposes, the performance data in some cases are also given for the clean aircraft configuration which is 1,500 pounds lighter than the airplane with four Sparrows. All performance data at altitude are at combat gross weight (60 percent of take-off fuel).

The performance data presented in most of these figures have been given for several different engine specifications. In all cases where the engine had any effect on the presented data, the figures have been labeled to indicate which engine specification was used. In general, all data to be used for further computation are good for the improved J79-GE-2 engine with specification AGT 400.

Figure 1 presents the maximum speed envelope of the F4H-1 for different altitudes. For the J-79-A-2 engine the maximum speeds attainable by the F4H-1 are limited by engine temperature restrictions at altitudes from approximately 23,000 feet to 56,000 feet. Also shown are the maximum speeds attainable by the J79-X-209A engine. At present, this is an experimental engine, but it may be of future interest.

Figure 2 contains the drag summary for this aircraft, where the lift coefficient (C_L) is plotted versus the coefficient of drag (C_D) for various Mach numbers. Figure 3 presents a curve



of the predicted maximum useable lift coefficient for various fighter Mach numbers.

The Mach Number-Load Factor Envelope, which is given in figure 4, outlines the maneuverability of the F4H-1 with maximum power at an altitude of 35,000 feet as limited by buffet and control power. Also included are the available load factors for constant speed turns and for -0.5 and -1.0 g deceleration turns at constant altitude are shown.

In figures 5 through 7, the amount of thrust that is required for the aircraft to sustain different steady state load factors for various fighter speeds is shown. Also given in these figures is the net thrust which is available from maximum, military and normal power settings. The data shown in each figure has been obtained for the aircraft flying at a constant altitude.

Climb data for the F4H-1 at different altitudes are presented in figures 8a and 8b. In figure 8a, the graphs give the rate of climb and also the time to climb to different altitudes. Figure 8b indicates the best subsonic and supersonic Mach Numbers for the F4H-1 to climb.

In figures 9 through 11, the net thrust that is available is given for different altitudes over a range of various Mach numbers. These net thrust figures are for maximum reheat power, military power, and normal power respectively. Also indicated in these figures are the aircraft Mach numbers at which the operation of the engine becomes either pressure limited or temperature limited. The thrust curves presented in these figures are given in terms of only one engine. It should be pointed out that the thrust values on the military power curve for speeds above $M = 1.4$ have been superseded, but the new data for the speeds above $M 1.4$ were not available.

For figure 12, it is assumed that the F4H-1 is on deck alert and is launched when a detected enemy bomber, coming in at $M = 1.0$ at 50,000 feet, is a given distance from the ship. The interceptor climbs to 50,000 feet and dashes out at maximum power to the point of intercept. The graph gives the distance to the point of intercept and the combat time which is available at maximum power for combat at that point.

CONFIDENTIAL



MODEL F4H-1
V_{max} vs Altitude
G.W. - 35,000 lbs.

VERY PRELIMINARY

CLEAN + (4) SPARROW III's

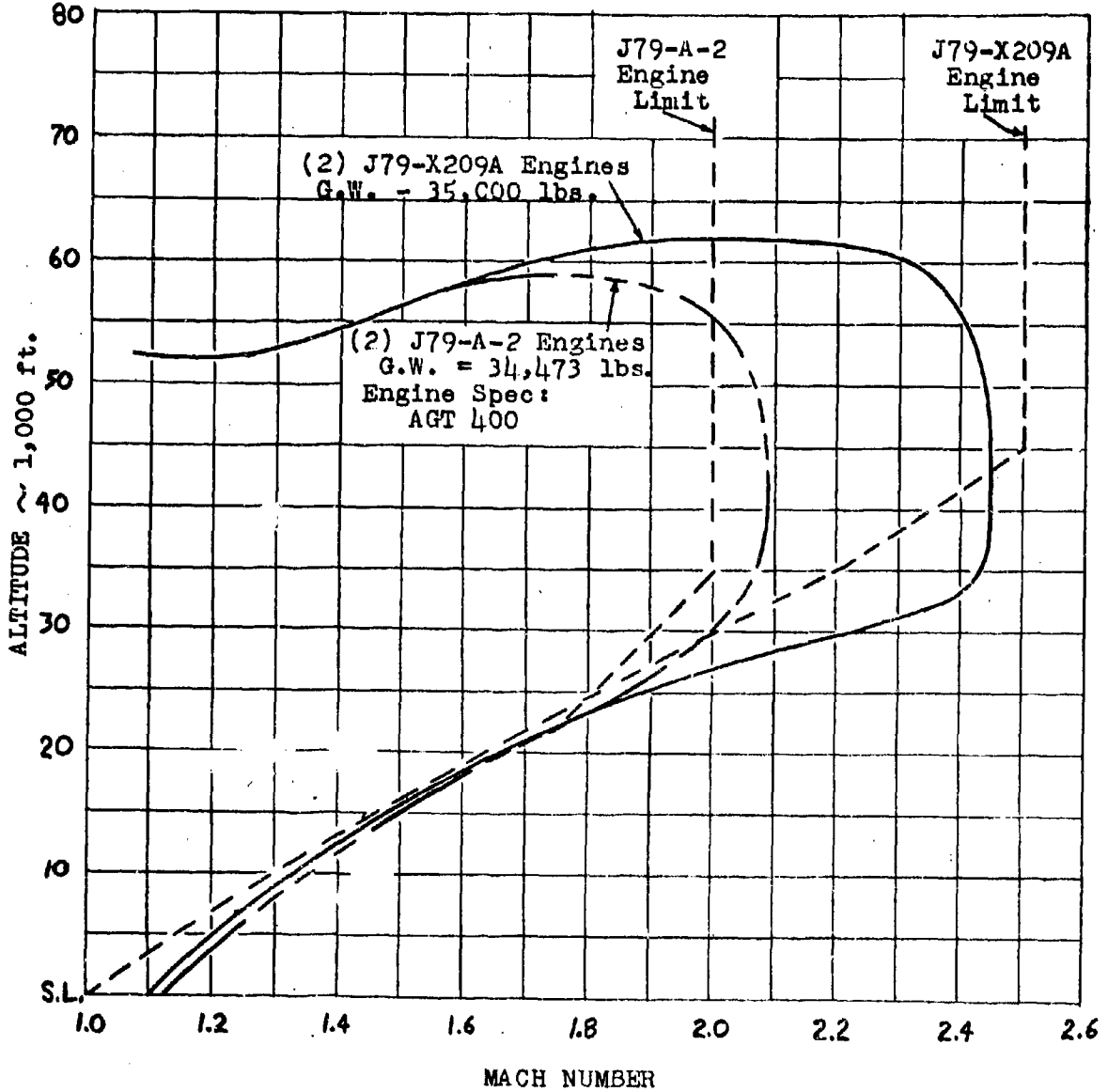


Figure I

CONFIDENTIAL



Model F4H-1 Airplane Drag Summary
(4) Sparrow III Missiles
Trimmed

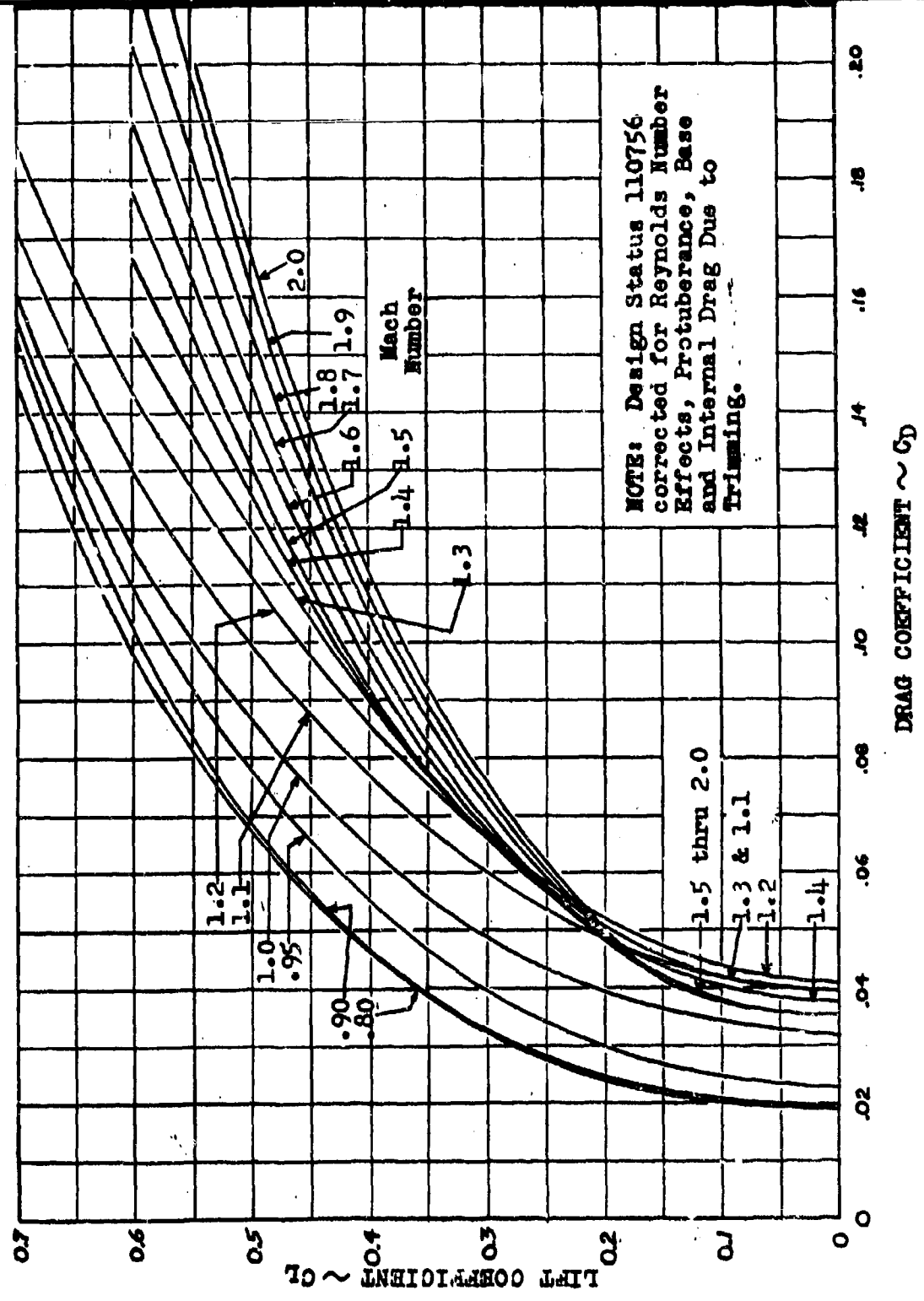


Figure 2



MODEL P4R-1
MAXIMUM USABLE LIFT

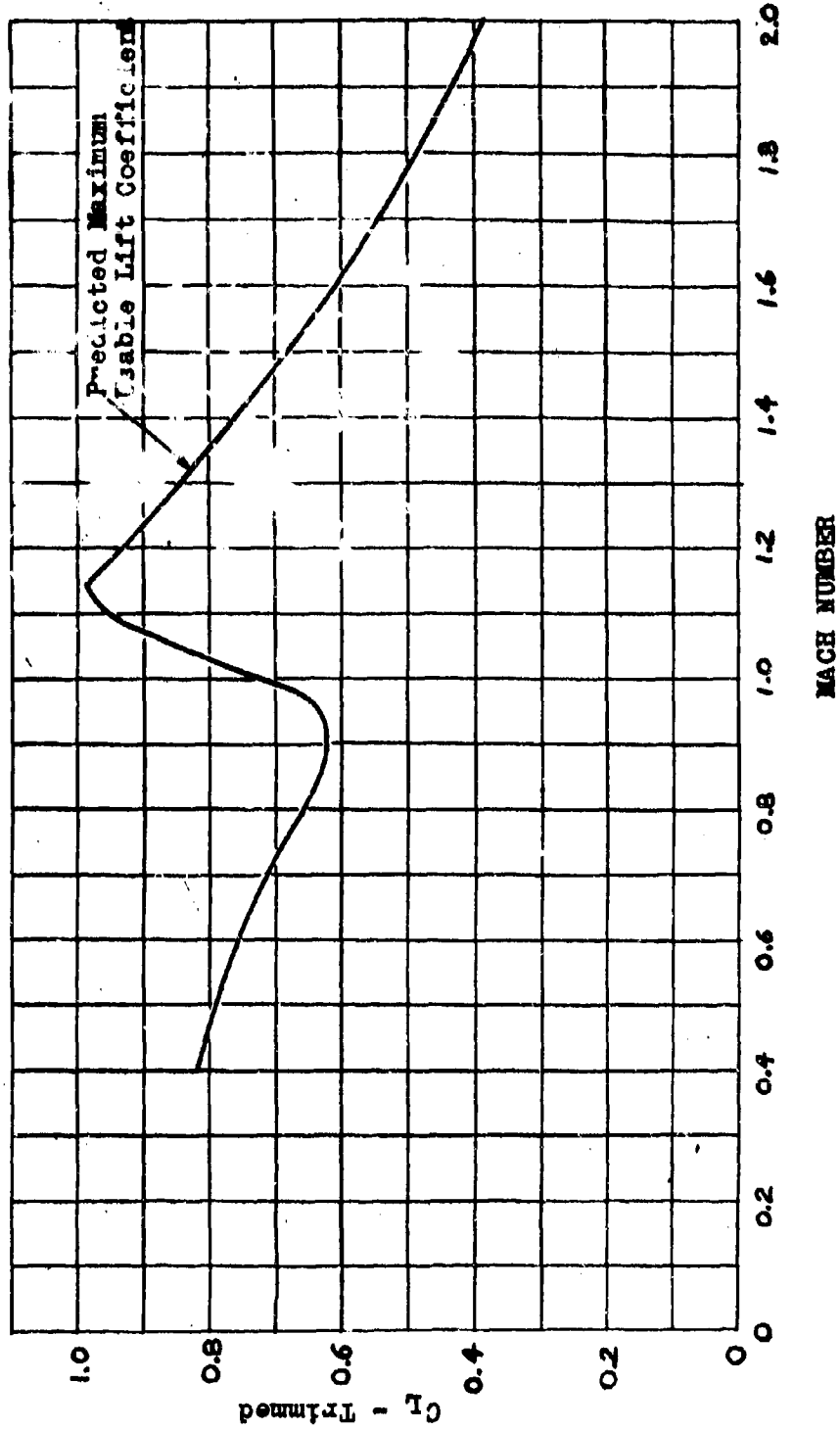
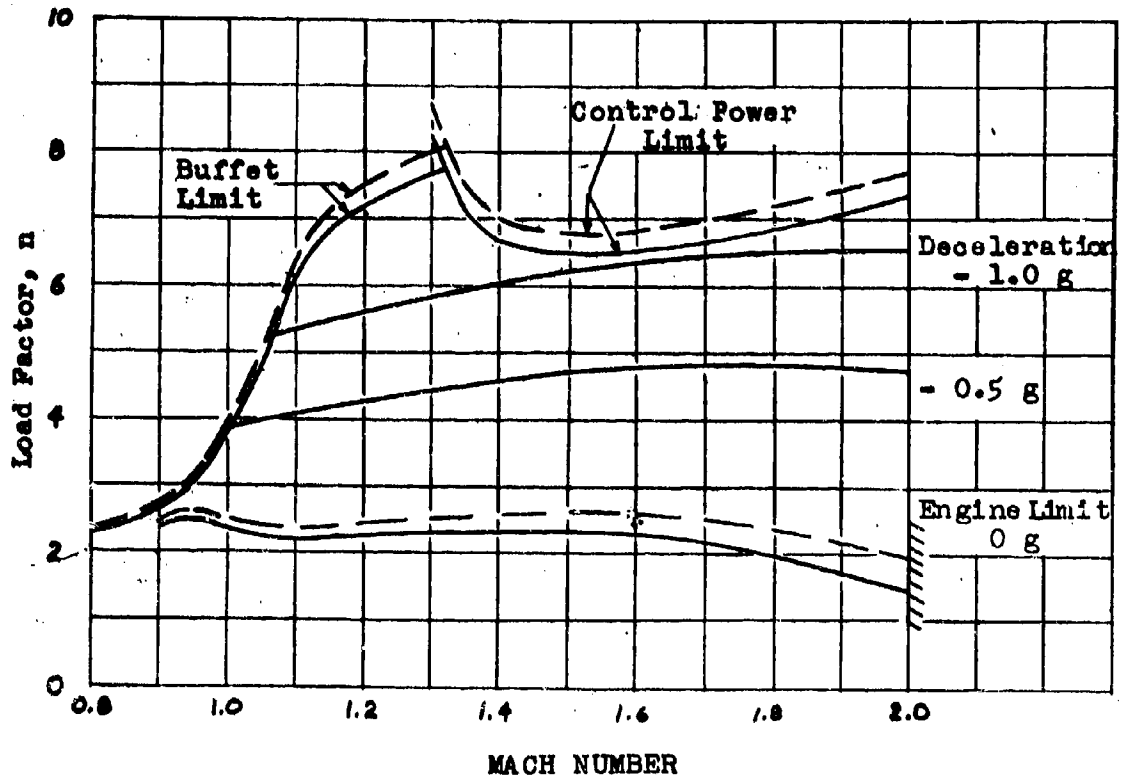


Figure 3



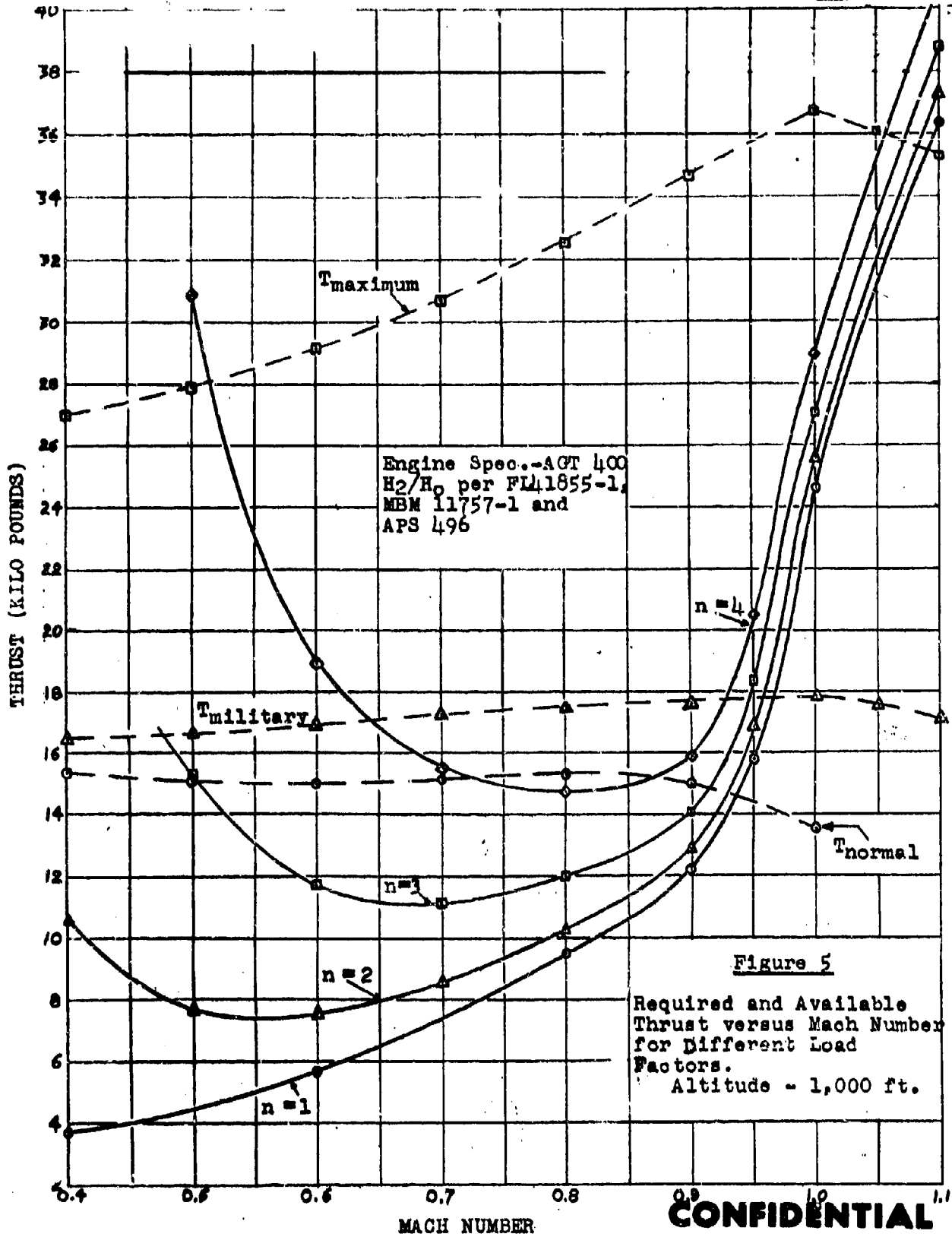
Model F4H-1 Mach Number - Load Factor Envelopes at
 Combat Weight at Altitude, 35,000 ft. with Maximum
 Power.

(2) J79-GE-2 Engines
 Engine Spec.-AGT 78; H₂/H₀: FL 41855-1



NOTE: Structure Designed for	_____ 4 Sparrow III	Gross Wt.
6.5 g at 34,500 lbs. Gross	----- Missiles	34,473
Weight	- - - - Clean	32,973

Figure 4



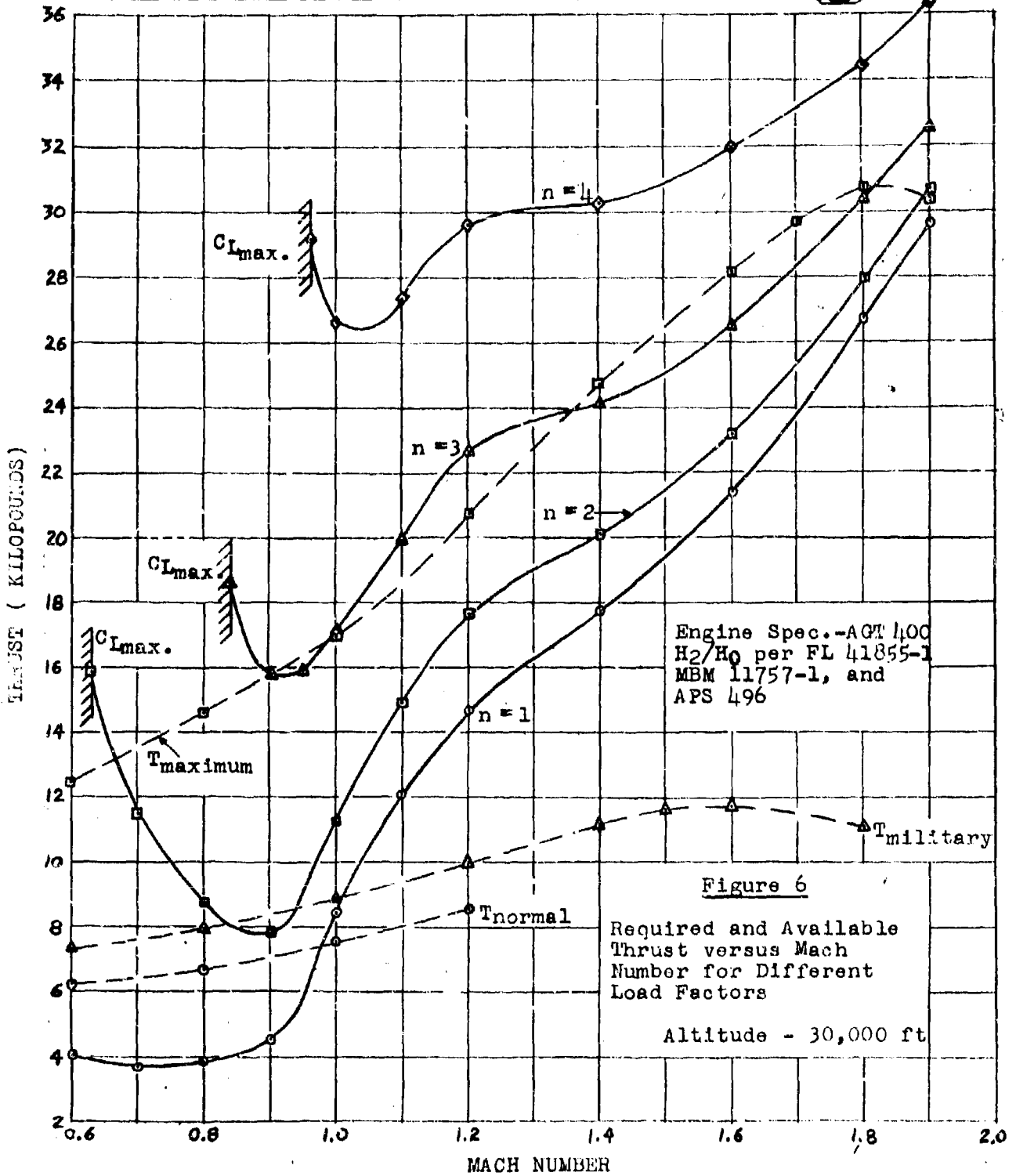


Figure 6

Required and Available Thrust versus Mach Number for Different Load Factors

Altitude - 30,000 ft

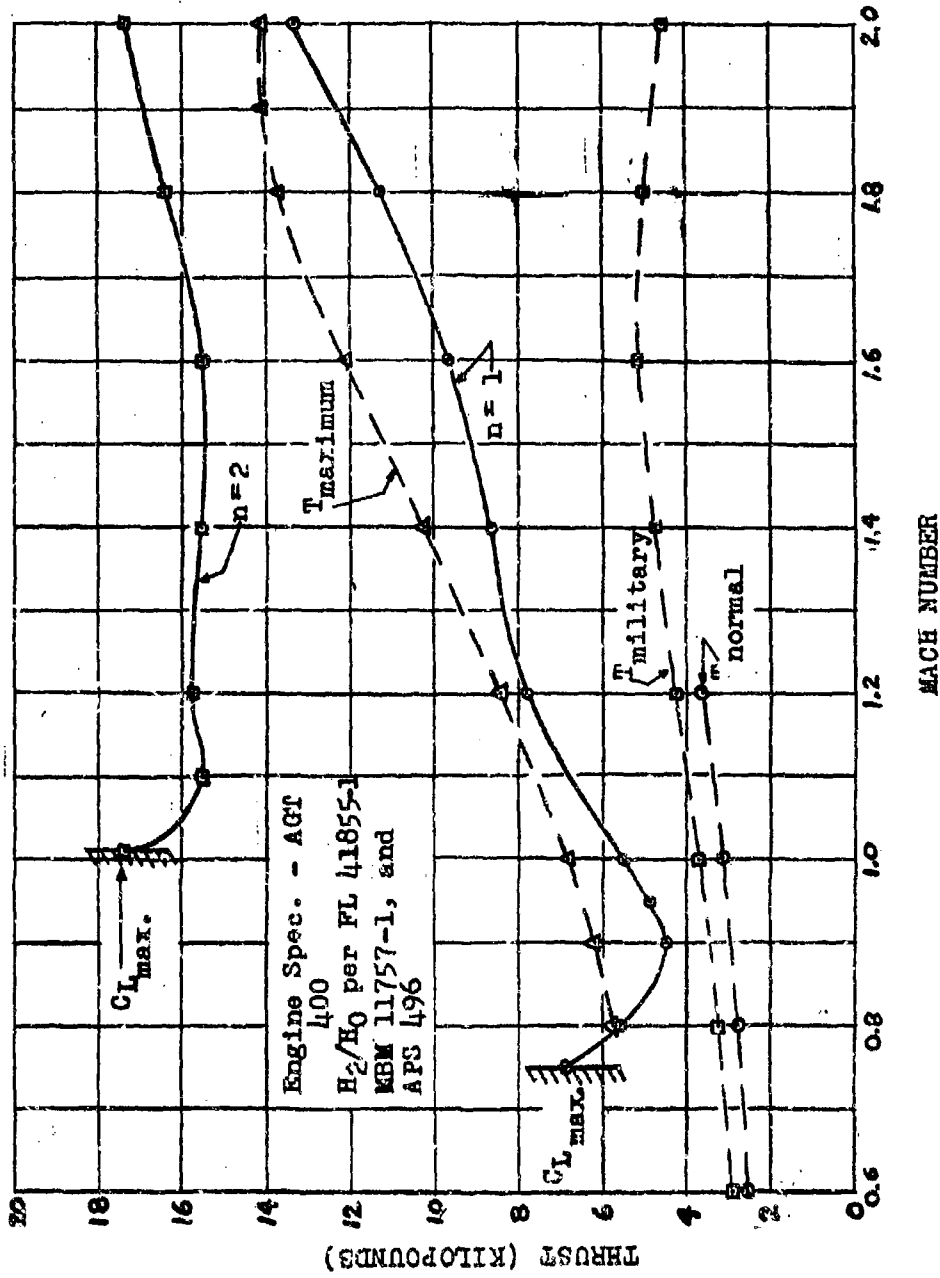
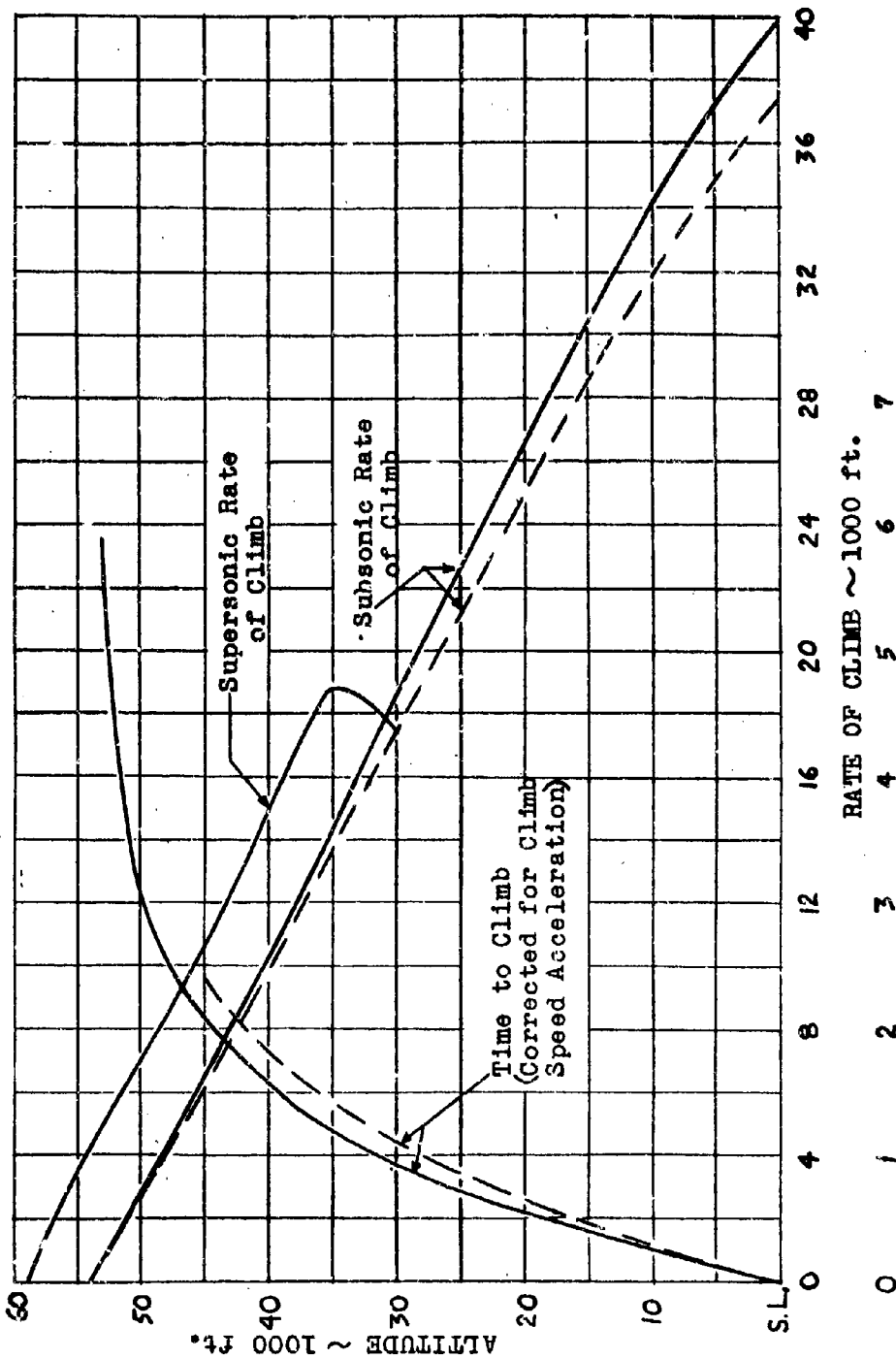


Figure 7. Required and Available Thrust versus Mach Number for Different Load Factors - Altitude = 50,000 ft.



Model F4H-1 Climb Data versus Altitude at Maximum Power
 4 Sparrow III Missiles Combat Gross Weight ~ 34,473 lbs.
 (2) J79-GE-2 Engines
 Current Perf: Drag = D.S. 110656; Engine Spec = AGT 400; H_2/H_0 :
 FL 41855-1 thru M 1.4; DGB 121856-1 beyond M 1.4.
 - - - - MAC Rpt. 4465: Drag = D.S. 62355; Engine Spec. = AGT 78; H_2/H_0 :
 FL 41855-1



TIME ~ MINUTES

Figure 8(a)



Model F4H-1 Climb Data versus Altitude at Maximum

Power

4 Sparrow III
Missiles

Combat Gross Weight -
34,473 lbs.

(2) J79-GE-2 Engines

Current Perf: Drag = D.S. 110656; Engine Spec =
AGT 400; H₂/H₀: FL 41855-1 thru
M 1.4, DGB 121856-1 beyond M 1.4.

- - - MAC Rpt. 4465: Drag = D.S. 62355; Engine Spec =
AGT 78; H₂/H₀: FL 41855-1.

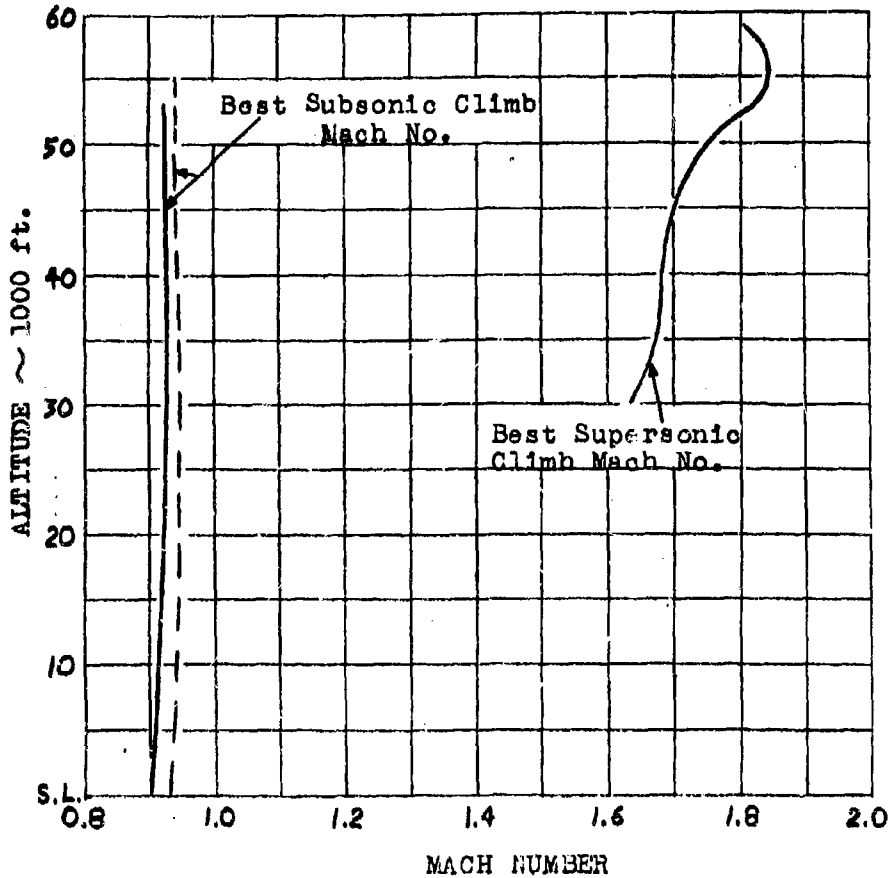
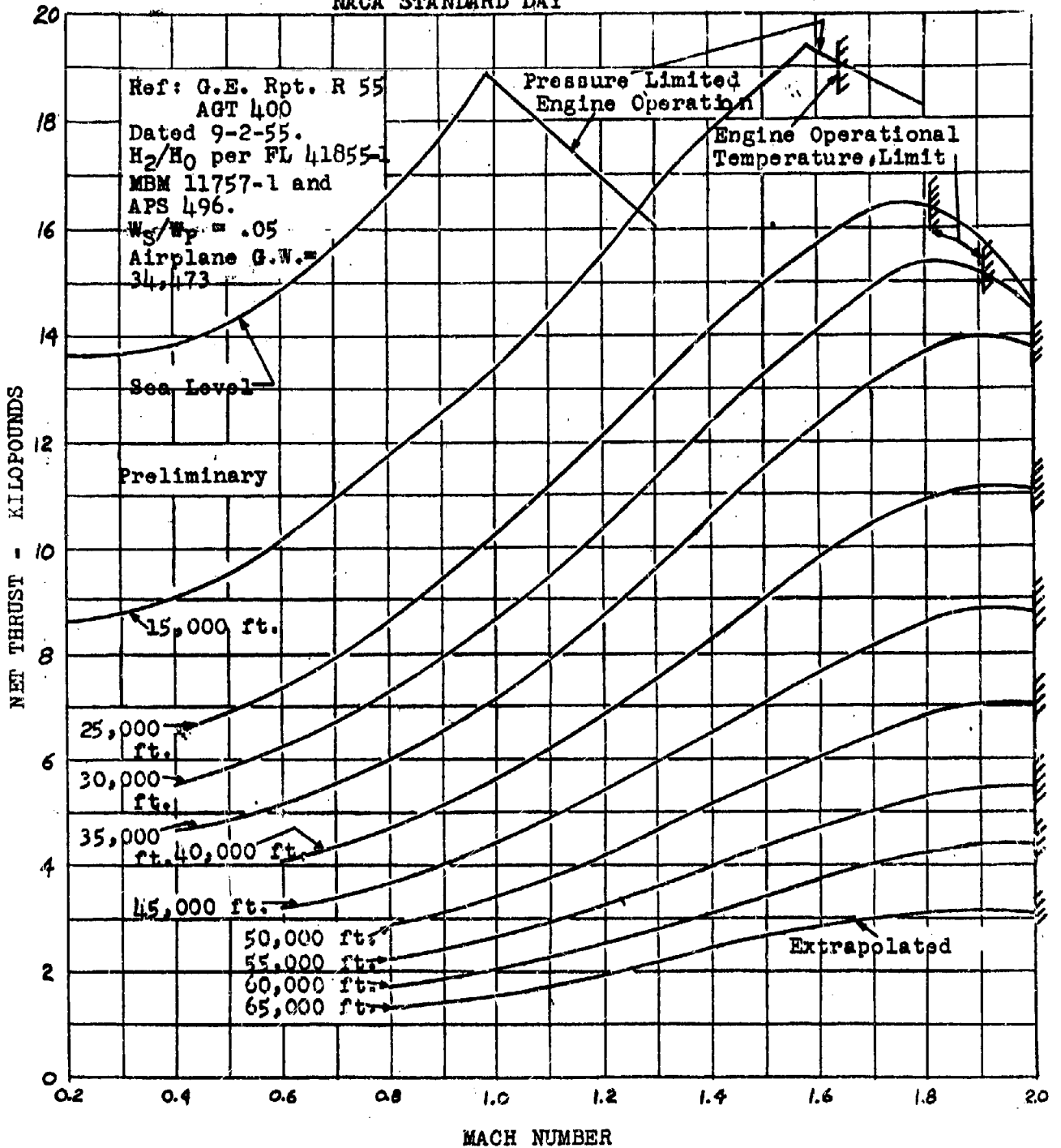


Figure 8(b)

CONFIDENTIAL



MAXIMUM REBERT NET THRUST
(1) GENERAL ELECTRIC J-79 ENGINE
NACA STANDARD DAY

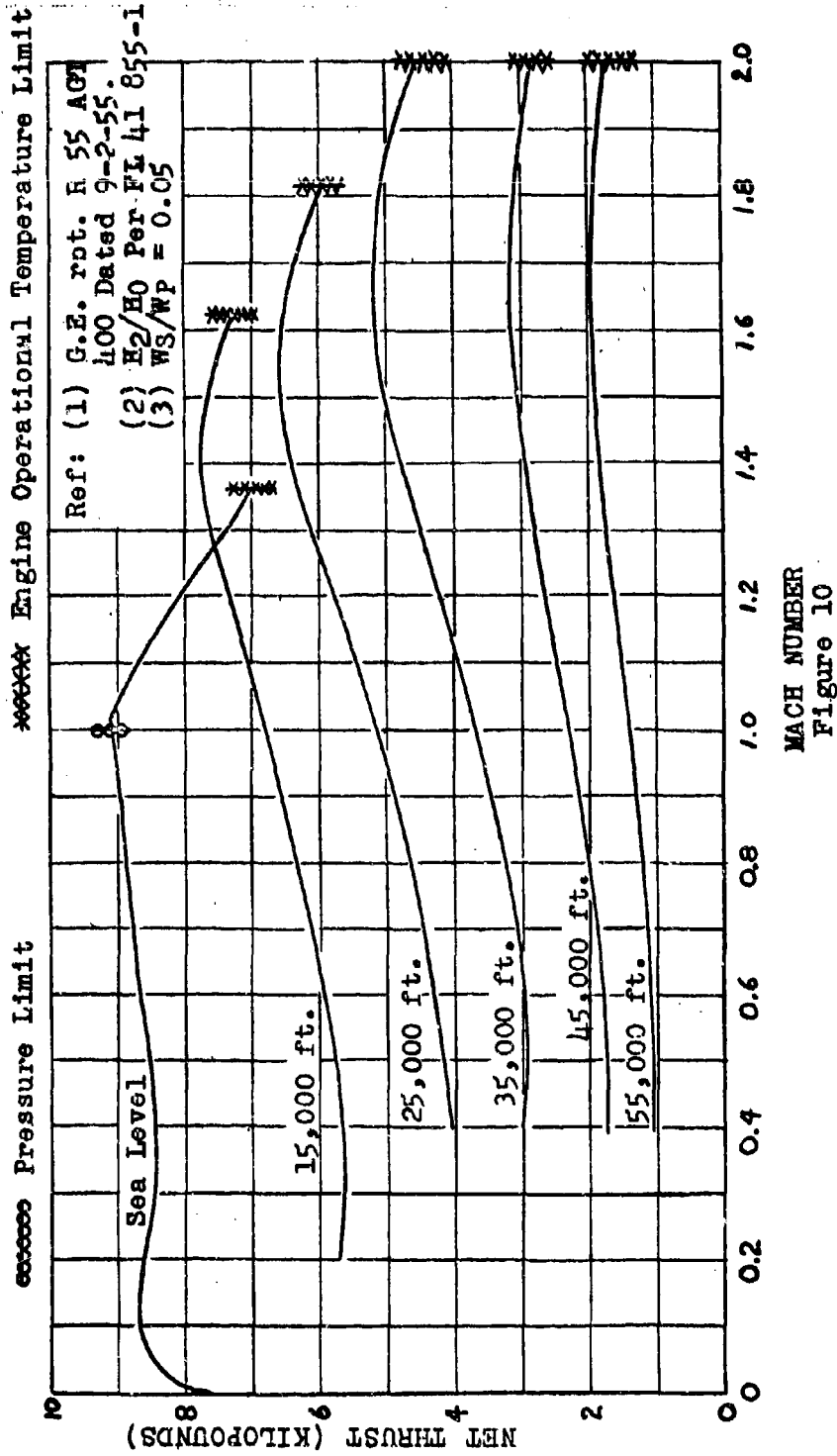


MACH NUMBER
Figure 9

CONFIDENTIAL

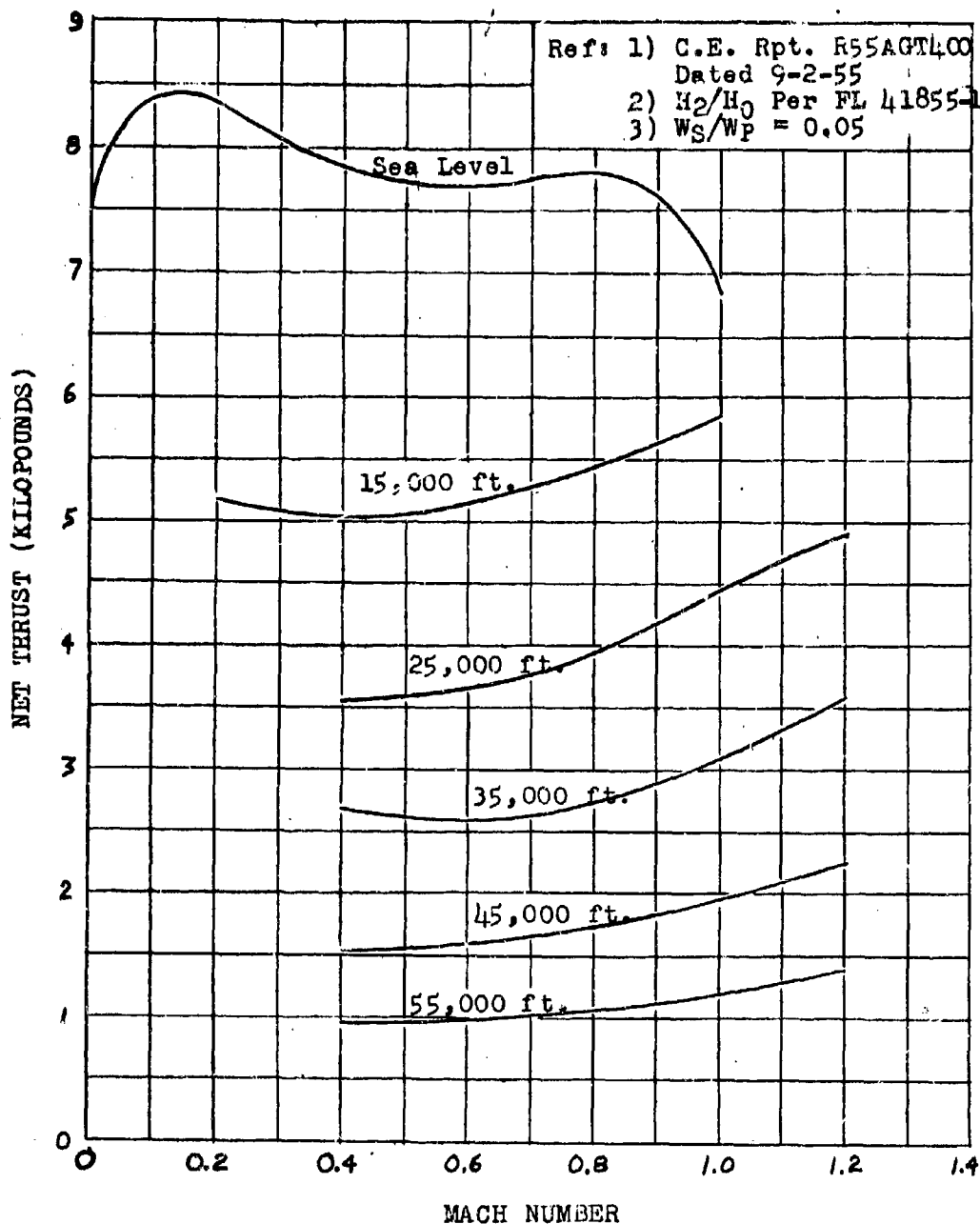


Military Power Net Thrust
(1) General Electric J-79 Engine
NACA Standard Day





Normal Power
Net Thrust
(1) General Electric J-79 Engine
NACA Standard Day

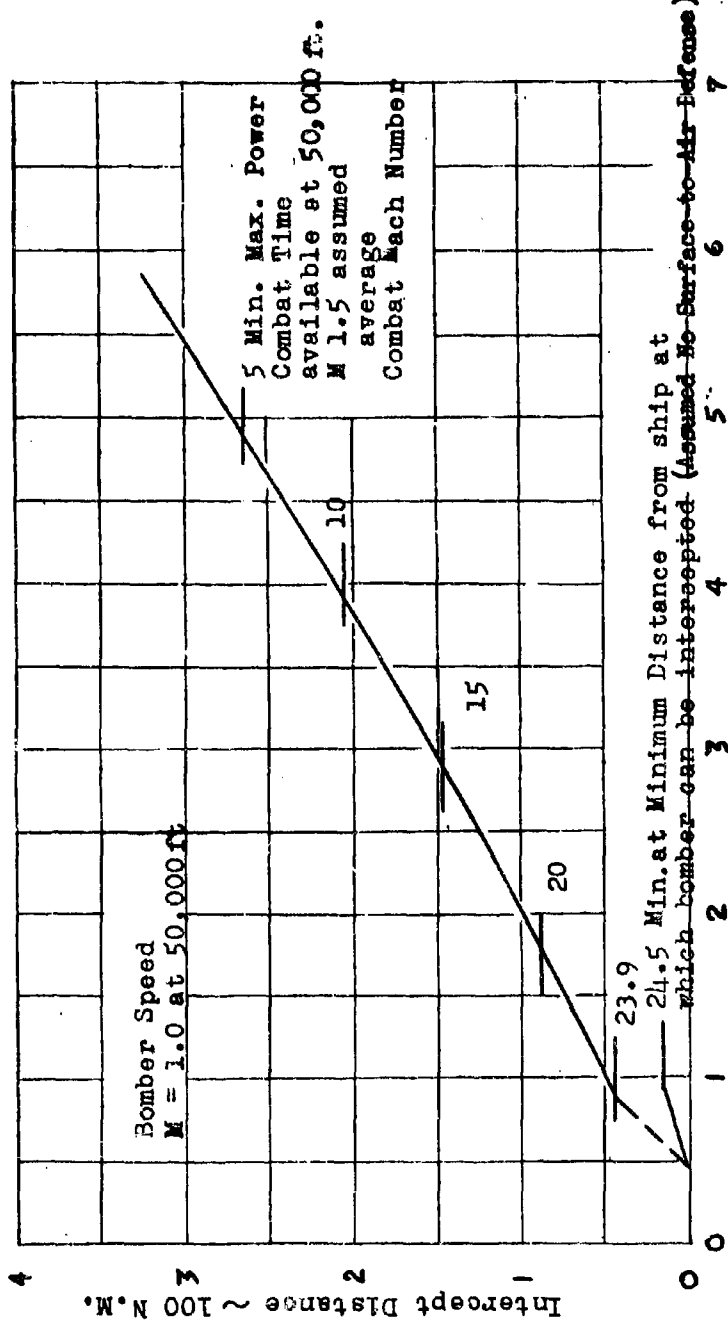


MACH NUMBER
Figure 11



Model F4H-1
 Intercept Distance versus Bomber Distance From Ship at Time of Detection
 (1) Sparrow III Missile Configuration.
 (2) J79-GE-2 Engines, Engine Spec. - AGT 78, H2/H0: FL 41855-1
 Intercept mission, dash at 50,000 feet.

NOTE: Take-off Gross Weight - 39839 lbs.; No External Fuel



Bomber Distance From Ship at Time of Detection ~100 n.m.

Figure 12



References

1. McDonnell Report No. 4518, Volume I, "Fighter Aerodynamic Status Report" Confidential, Dated 16 December 1955, Revised 9 April 56.
2. McDonnell Report No. 4465, "F4H-1 Two Seat Twin Engine All-Weather Fighter and Long Range Attack", Confidential, Dated 3 January 1956, Revised 30 April 1956.
3. McDonnell Report No. APS-519 "Model F4H-1 Current Performance Status Summary", Confidential, Dated 7 February 1957.

CONFIDENTIAL



APPENDIX III

Addendum to Navy Missile Study Technical Report No. 2

F4H-1 Basic Performance Data

-90114-

6/12/57

R. B. Tucker

(Proprietary Information
(McDonnell Aircraft Company))

6-12/lm

CONFIDENTIAL

CONFIDENTIAL



Table of Contents

	Page
I Synopsis	1
II Basic Performance Data	1
References	4

CONFIDENTIAL



Illustrations

Figure		Page
1	Model F4H-1 Lift Curve Slope Variation with Mach Number	2
2	Model F4H-1 Airplane Drag Summary	3

CONFIDENTIAL



I. Synopsis

This addendum contains two graphs that presents further basic performance data on the F4H-1 aircraft.

II. Basic Performance Data

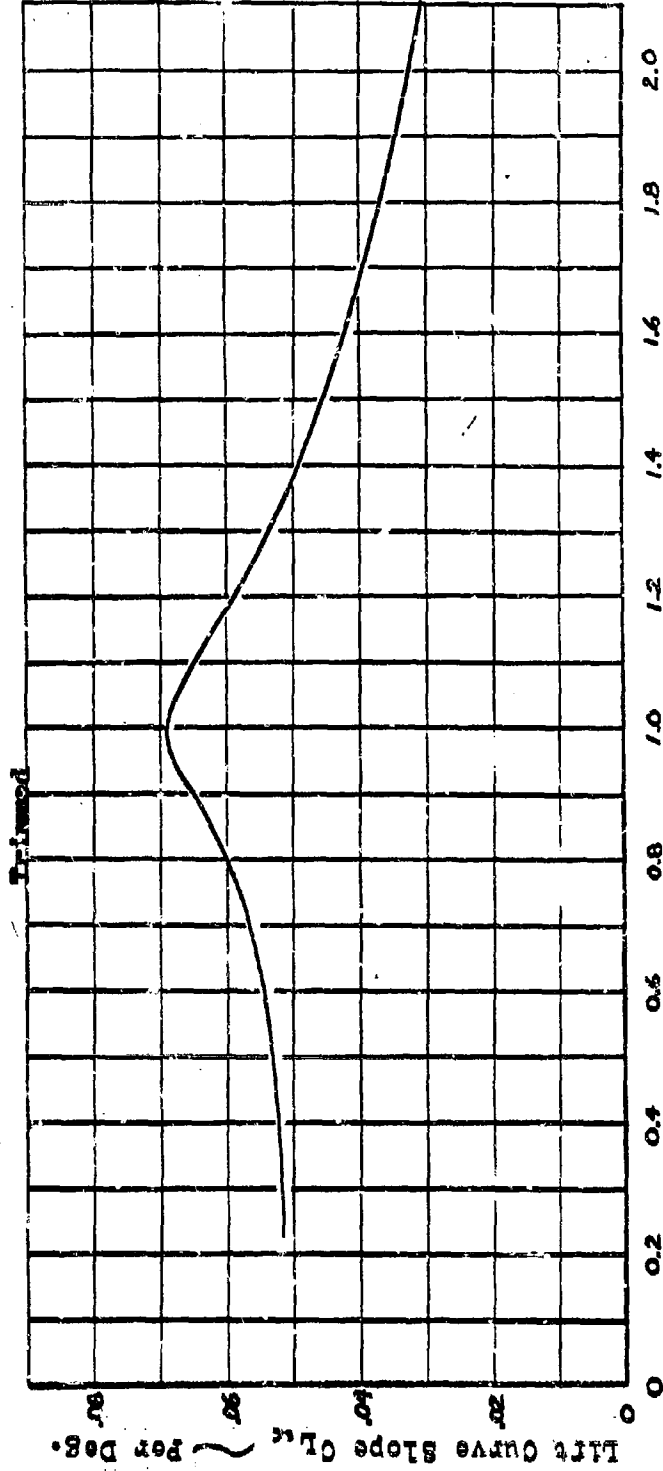
Figure 1 shows the Model F4H-1 lift curve slope variation, ($C_{L_{\alpha}}$), versus Mach Number which was omitted in the original report.

Figure 2 is an extension of the figure 2 contained in the body of NMSTR #2. This figure presents the drag summary for this aircraft, where the lift coefficient (C_L) is plotted versus the coefficient of drag (C_D) for various Mach Numbers of trimmed flight. It was found necessary to have data for C_L above the value of $C_L = 0.7$ to permit analysis at maximum values of C_L . Thus, the data presented in this figure presents the original data plus extrapolated data out to $C_L = 1.0$.

CONFIDENTIAL



Model F4U-1
Lift Curve Slope Variation With Mach Numbers



Mach Number ~ M

Figure 1

CONFIDENTIAL



References

1. McDonnell Report No. 4873, "Model F4H-1 Two-Place All-Weather Fighter Aerodynamic Status Report", Confidential, Dated 3 August 1956, Revised 4 September 1956.
2. Navy Missile Study Technical Report #4, "A Method For Extending the Lift versus Drag Data of Navy Missile Study Technical Report #2 ("F4H-1 Basic Performance Data")" Dated 6-10-57, Confidential.

CONFIDENTIAL

CONFIDENTIAL



APPENDIX IV

Navy Missile Study Technical Report #4

A Method For Extending the Lift vs. Drag Data
Of Navy Missile Study Technical Report #2, F4H-1
Basic Performance Data

-90014-

6/10/57
J. Scott

(Proprietary Information McDonnell
Aircraft Co.)

6-10/lm

CONFIDENTIAL

**SYNOPSIS**

The lift coefficient (C_L) vs. drag coefficient (C_D) curves (Figure 2)* contained in Navy Missile Study Technical Report #2 were extrapolated so that they could be read to the maximum usable lift coefficient (Figure 3)*. The only curves in question were those between and including Mach 1.0 to 1.6.

* Figure number refers to Navy Missile Study Technique Report #2, F4H-1 Basic Performance Data (5/9/57), R. B. Tucker.



I. Introduction

Observing figures 2 and 3 in the Navy Missile Study Technical Report #2, it was noticed that the curves from Mach 1.0 through Mach 1.6 of Figure 2 could not be read to the maximum usable lift coefficient. This paper describes a method by which the C_L vs. C_D curves were extrapolated to make this information available.

II. Discussion of Equation

Referring to Model F4H-1 Two-Place All-Weather Fighter, Aerodynamic Status Report, (First Periodic Revision, 9/4/56), S. K. Lundgraf, Page 4.1:

$$C_{Dtotal} = C_{D0Eff} + C_{D0} + LC_L^2 + C_{Df}(C_L) + C_{Dtrim}$$

Although C_{Dtrim} is a rather large value, it was ignored because the values from these curves are in doubt. C_{D0} was dropped because it is small and constant for any mach number. Looking at the figure on page 4.7 of the above report,

C_{D0Eff} - intersection of the extension of the linear portion of the C_D vs. C_L curve with the zero lift axis.

L - induced drag factor, $\frac{dC_D}{dC_L^2}$

$C_{Df}(C_L)$ - non-parabolic drag

C_{D0Eff} , L and $C_{Df}(C_L)$ were determined from the graphs on pages 4.12a, 4.14 and 4.15 respectively of the above report. The revised equation is as follows:

$$C_D = C_{D0Eff} + LC_L^2 + C_{Df}(C_L)$$

III. Method of Extrapolation

Values of C_D were calculated from the revised equation for various values of C_L at the mach numbers in question. (See table below.) Using these values, a set of C_L vs. C_D curves were plotted. Because of the revision of the equation, this set of curves was displaced, along the drag axis, from the set of curves to be extrapolated. However, the forms of the two sets of curves are similar.

The mach 1.4 curve of Figure 1 will serve as an example of the extrapolation procedure. Curve OA was plotted using the calculated points from the above table. Along side of it, OB, the



C_L	C_D						
	M 1.0	M 1.1	M 1.2	M 1.3	M 1.4	M 1.5	M 1.6
0.1	0.025	0.035	0.036	---	---	---	---
0.2	0.031	0.042	0.044	0.045	0.046	---	---
0.3	0.042	0.055	0.057	0.059	0.059	0.063	0.065
0.4	0.057	0.072	0.075	0.078	0.082	0.084	0.070
0.5	0.076	0.094	0.099	0.100	0.110	0.114	0.120
0.6	0.100	0.120	0.130	0.130	0.140	0.150	0.160
0.7	0.140	0.150	0.150	0.170	0.180	0.190	0.200
0.8	0.190	0.200	0.200	0.210	0.220	0.240	0.260
0.9	0.270	0.260	0.240	0.260	0.270	0.290	0.320
1.0	0.360	0.320	0.290	0.310	0.330	0.320	0.380

curve to be extrapolated, was replotted from Figure 2 of the Navy Missile Study Technical Report #2. Taking into account the relationship of the slopes of curves OA and OB, and making a "by eye" approximation, OB was extended to B'. Thus an extrapolation effectively using the C_{DTrim} estimation of the original curve was made.

IV. Results

The extrapolated curves are shown in Figure 2. For mach 1.0 through 1.2, the curves were extended from a C_L of 0.7 to a C_L of 1.0. For mach values from 1.3 through 1.6 the curves were extended from a C_L of 0.6 to a C_L of 1.0.

Just below mach 1.2 for the higher values of C_L , $C_{Dr}(C_L)$ becomes very large. This effect manifests itself in the convergence of the mach 1.0 and 1.1 curves with the other curves in the group.

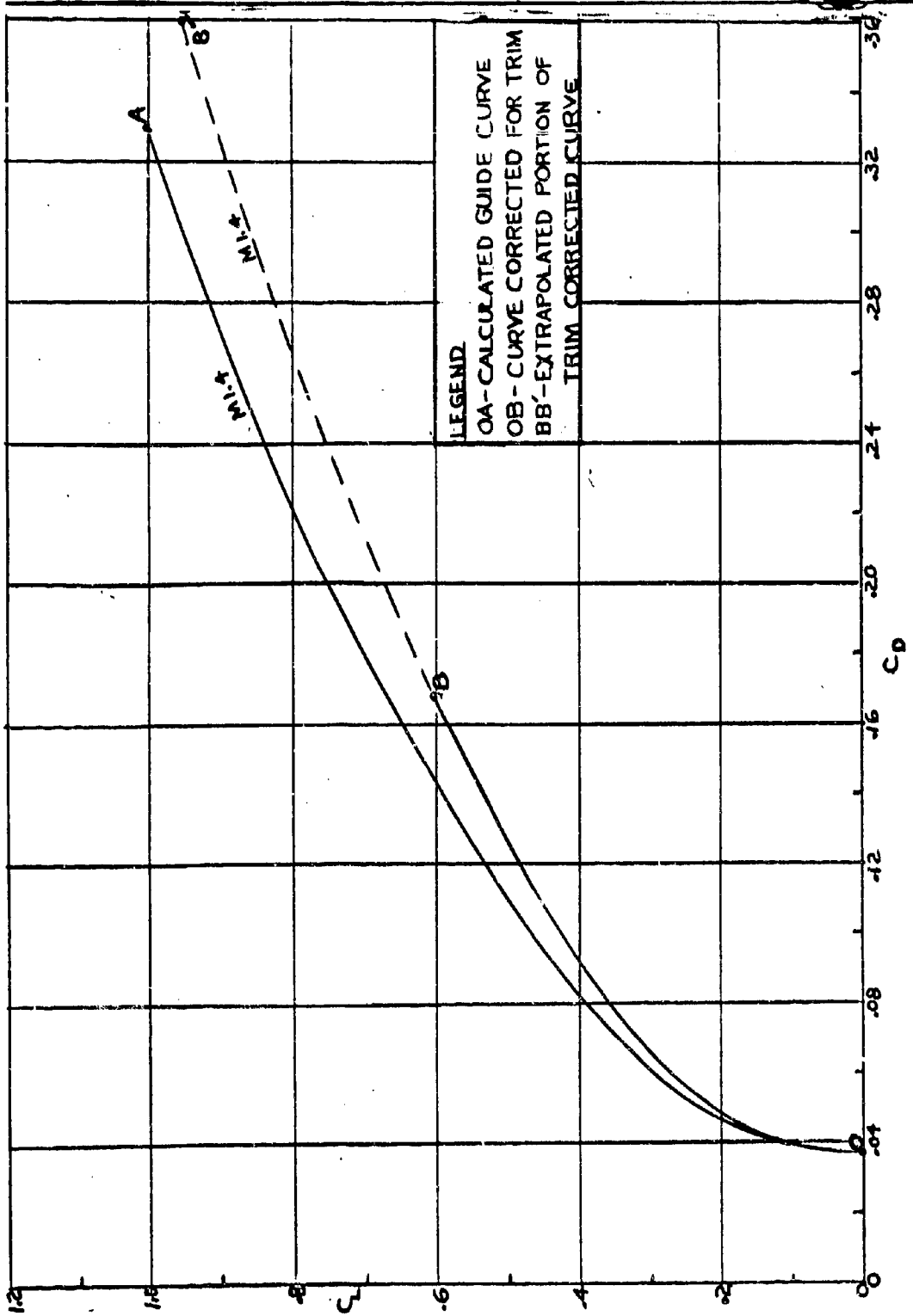
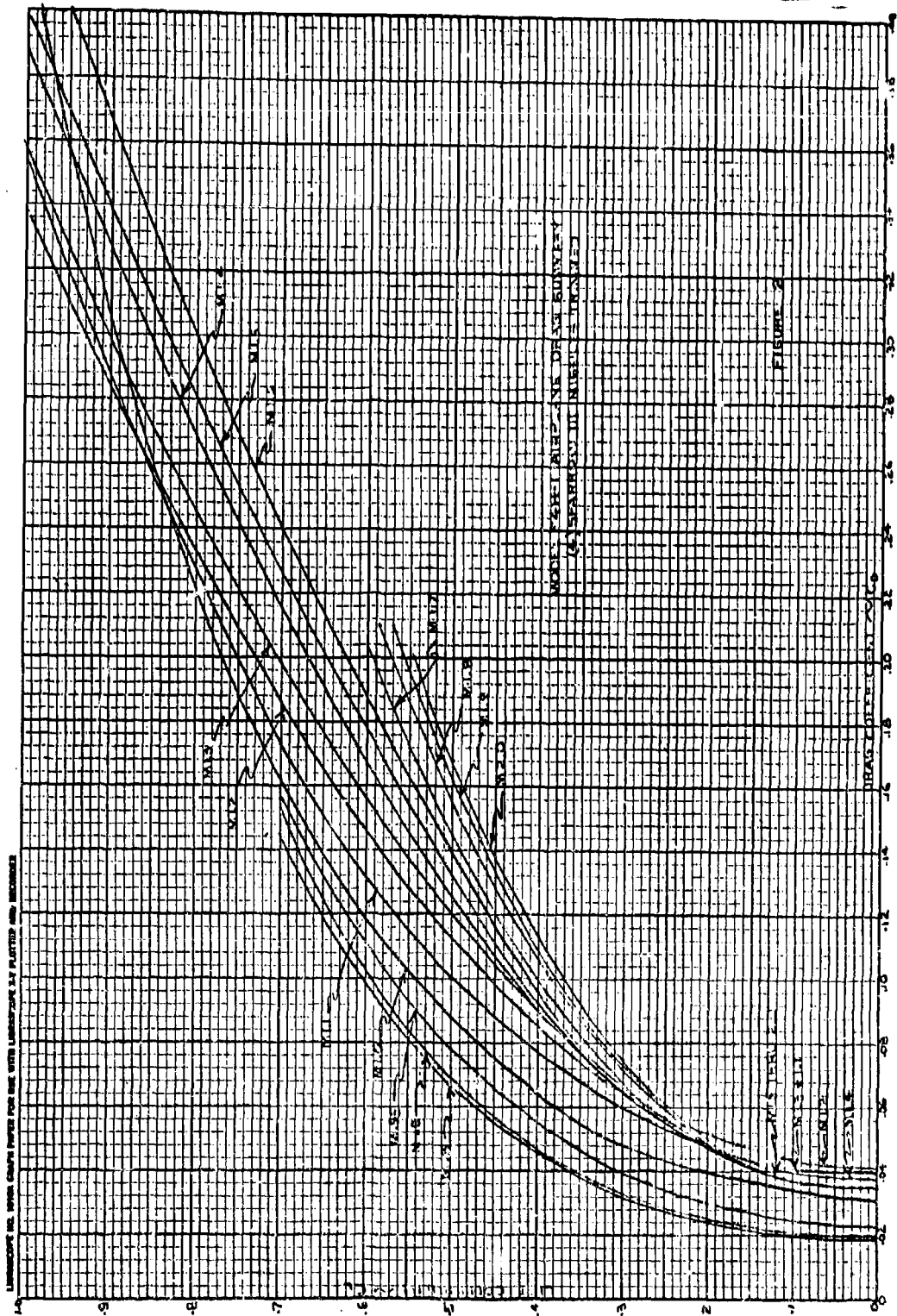


FIGURE 1



MODEL SPECTRA OF PLANETS AND MOONS
(BASED ON DATA FROM SURVEYOR)

Figure 2

LUMINOUS FLUX (WATTS PER METER SQUARED) AT EARTH'S DISTANCE

CONFIDENTIAL



APPENDIX V

Navy Missile Study Technical Report #3

LATERAL AND LONGITUDINAL EQUATIONS DESCRIBING THE SPARROW III
MISSILE TRAJECTORY IN SPACE DURING A COPLANAR ATTACK

by

G. C. Anthony
Navigation and Flight Control Group
May 15, 1957

Charge

003-103-100-C-90114

5/16-1u

CONFIDENTIAL

CONFIDENTIAL



ABSTRACT

This report presents the equations which describe the Sparrow III missile trajectory from missile lock-on until impact. The equations have been presented for coplanar attacks in both the horizontal and vertical planes and assume a non-maneuvering target.

Due to the scarcity of information it was impossible to extend the trajectory to cover the period from launch until lock-on. However, when the required information is made available the necessary modifications will be published in a subsequent report.

CONFIDENTIAL



TABLE OF CONTENTS

	<u>Page</u>
Abstract	1
List of Illustrations	111
Symbols	1v
1. INTRODUCTION	1
2. MISSILE EQUATIONS	1
2.1 Longitudinal	1
2.2 Lateral	3
3. DISCUSSION	8
4. SUMMARY	8



LIST OF ILLUSTRATIONS

	<u>Page</u>
Fig. 1. Missile-target geometry	2
2. Zero lift drag coefficients vs. Mach number	4
3. Drag due to lift vs. Mach number	5
4. Maximum trimmed lift coefficient vs. Mach number	6

SYMBOLS

- a = Speed of sound
- g = Acceleration of gravity
- h = Altitude of Missile
- N_a = Actual normal acceleration of missile (g's)
- N_c = Commanded normal acceleration to missile (g's)
- p = Atmospheric pressure
- P_0 = Atmospheric pressure at sea level (2116.2 lb/ft²)
- q = Dynamic pressure of air
- t = Time
- t_b = Duration of missile boost
- C_D = Drag coefficient of missile
- C_{DB} = Zero lift drag coefficient of missile during boost phase
- C_{DG} = Zero lift drag coefficient of missile during glide phase
- C_L = Lift coefficient of missile
- D = Drag force on missile
- L = Lift force on missile
- M = Mach number of missile
- P = d/dt
- S = Wing area of two panels
- T = Missile Thrust
- V = Velocity of missile
- V_t = Velocity of target
- V_c = Component of the closing velocity falling along the conical scan axis
- ΔV_x = Component of the closing velocity falling along the X axis
- ΔV_z = Component of the closing velocity falling along the Z axis



- W = Missile weight
- W_0 = Missile weight after boost (glide phase)
- W_L = Missile weight at launch
- X = X coordinate of missile
- X_t = X coordinate of target
- Z = Z coordinate of missile
- Z_t = Z coordinate of target
- γ = Flight path angle of missile
- γ_t = Flight path angle of target
- δ = Surface deflection of missile
- ϵ = Angle between the conical scan axis and line of sight from the missile to the target
- λ = Angle between a horizontal plane and the line of sight from the missile to the target
- λ_e = Angle between a horizontal plane and the conical scan axis
- ρ = Density of air
- ρ_0 = Density of air at sea level (.002378 slugs/ft³)
- σ = Density ratio (ρ/ρ_0)

- NOTES: (1) English units (ft. - lb. - sec.) will be used throughout with all angles given in degrees.
- (2) K_5 , K_6 , T_3 , and T_5 are autopilot parameters and are listed in Table I.
- (3) $\frac{\Delta C_D}{C_N^2} C_L^2$ is the component of the drag coefficient due to lift and is described in figure 3.



1. INTRODUCTION

The purpose of this report is to present the longitudinal and lateral equations for the Sparrow III air-to-air missile in a coplanar attack on a non-maneuvering target. The equations describe the space trajectory of the missile from the time of lock-on to the time of impact with the target.

These equations are intended to provide a general set of equations which can be applied to a large number of problems. Furthermore, since the Sparrow III information is rather incomplete it has not been possible to describe the actual missile operation in the detail that one might expect. This supplementary information will be published in a subsequent report.

2. MISSILE EQUATIONS

2.1 Longitudinal

When using the pitch-up launching technique it is possible to obtain altitude differentials of approximately 33,000 feet when the fighter starts the attack at 35,000 feet*. In view of this large variation in altitude it is recommended that the variation of air density, pressure, and speed of sound with altitude be taken into account.

This type of program has already been programmed on the IBM 704 computer and has been completely checked out. It will thus be assumed that this program (AA ATM) will be used in conjunction with the following equations. This program will require altitude (in feet) as an input and will produce pressure ratio, density ratio, and speed of sound (in ft./sec.) as outputs**.

The missile trajectory can thus be defined by the following equations:

$$M = \frac{V}{a} \tag{1}$$

$$q = \frac{1}{2} \rho_0 V^2 \sigma \tag{2}$$

$$L = q S C_L \tag{3}$$

$$D = q S C_D \tag{4}$$

$$\dot{V} = g \left(\frac{L}{W} - \sin \gamma \right) \tag{5}$$

$$\dot{\gamma} = \frac{g}{V} \left(\frac{L}{W} - \cos \gamma \right) \tag{6}$$

$$\dot{X} = V \cos \gamma \tag{7}$$

$$\dot{Z} = -\dot{h} = -V \sin \gamma \tag{8}$$

* "Pitch-up Launching Studies for Sparrow III - F3H-2M Missile-Airplane Combination", U.S. Naval Air Development Center, Johnsville, Pa., Report No. NADC-WR-5622, Dated October 1956. (Secret)

** Temperature in degrees Rankine would also be available if this quantity were required.



Figure 1 shows the missile-target geometry.

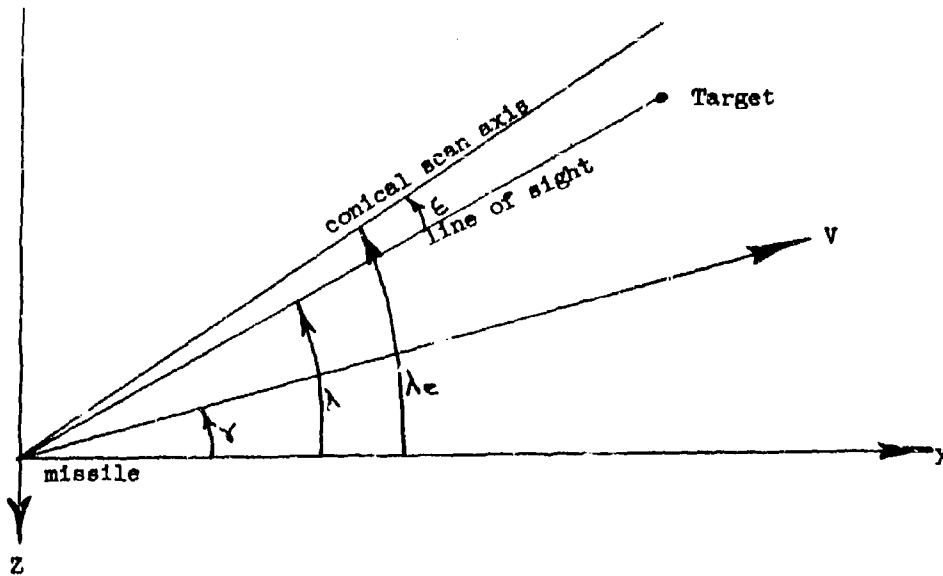


Figure 1. Missile-target geometry

$$\Delta V_x = V \cos \gamma - V_t \cos \gamma_t \quad (9)$$

$$\Delta V_z = -V \sin \gamma + V_t \sin \gamma_t \quad (10)$$

$$V_c = \Delta V_x \cos \lambda_e - \Delta V_z \sin \lambda_e \quad (11)$$

$$\epsilon = \lambda_e - \lambda \quad (12)$$

$$\lambda = \arctan - \frac{Z_t - Z}{X_t - X} \quad (13)$$

$$\dot{Z}_t = 0 \quad (14)$$

$$\dot{X}_t = V_t \quad (15)$$

The autopilot equations are:

$$\delta = - \frac{K_5 T_5}{1 + T_5 P} \left(N_a - \frac{N_c}{1 + T_3 P} + K_6 \dot{\gamma} \right) \quad (16)$$

$$N_a = \frac{L}{W} - \cos \gamma \quad (17)$$

$$N_c = .013 \epsilon V_c \quad (18)$$

$$\dot{\lambda}_e = 6 \epsilon \quad (19)$$



$$C_L = \frac{C_{Lmax}}{\beta} \quad (20)$$

In the above equations W, T, and C_D have different values for the boost and glide phase. These values are:

<u>Boost Phase</u>	<u>Glide Phase</u>
$T = 8889 + \frac{P_0}{5} (1 - \frac{P}{P_0})$	$T = 0$
$C_D = C_{DB} + \frac{\Delta C_D}{C \frac{2}{N}} C_L^2$	$C_D = C_{DG} + \frac{\Delta C_D}{C \frac{2}{N}} C_L^2$
$W = W_L - \left(\frac{W_L - W_G}{t_b} \right) t$	$W = W_G$

In these equations C_{DB} , C_{DG} , $\frac{\Delta C_D}{C \frac{2}{N}}$, and $\frac{C_{Lmax}}{\beta}$ are functions of Mach number, and the approximate nature of their variation can be found in figures 2-4.

Table I also lists the various missile characteristics including the autopilot gains and missile limits which must be used in the above equations. However, since the autopilot gains are set at launch, it is the launching altitude that determines the autopilot gain and not the instantaneous altitude of the missile.

2.2 Lateral

Due to the symmetry of the Sparrow III missile about its longitudinal axis the missile dynamics will be the same in both the lateral and longitudinal planes. Thus the only difference in the equations will be those due to gravity. In view of this fact it becomes necessary to make two types of changes: (1) remove the acceleration due to gravity from the three acceleration equations (equations 5, 6, and 17), and (2) add the drag due to the vertical lift that is required to maintain level flight.

The equations in the previous section can thus be converted into the lateral form by merely making the following changes:

- 1) Replace Z with Y in equations 8, 10, 11 and 13.
- 2) Drop the trigonometric function of γ in equations 5, 6, and 17.
- 3) Replace C_L^2 with $(C_L^2 + C_{Lg}^2)$ in the C_D equations for both the boost and glide phases (where $C_{Lg} = \frac{W}{qS}$).

It should also be noted that these lateral equations describe a constant altitude attack and thus ρ , p , and a are constant.

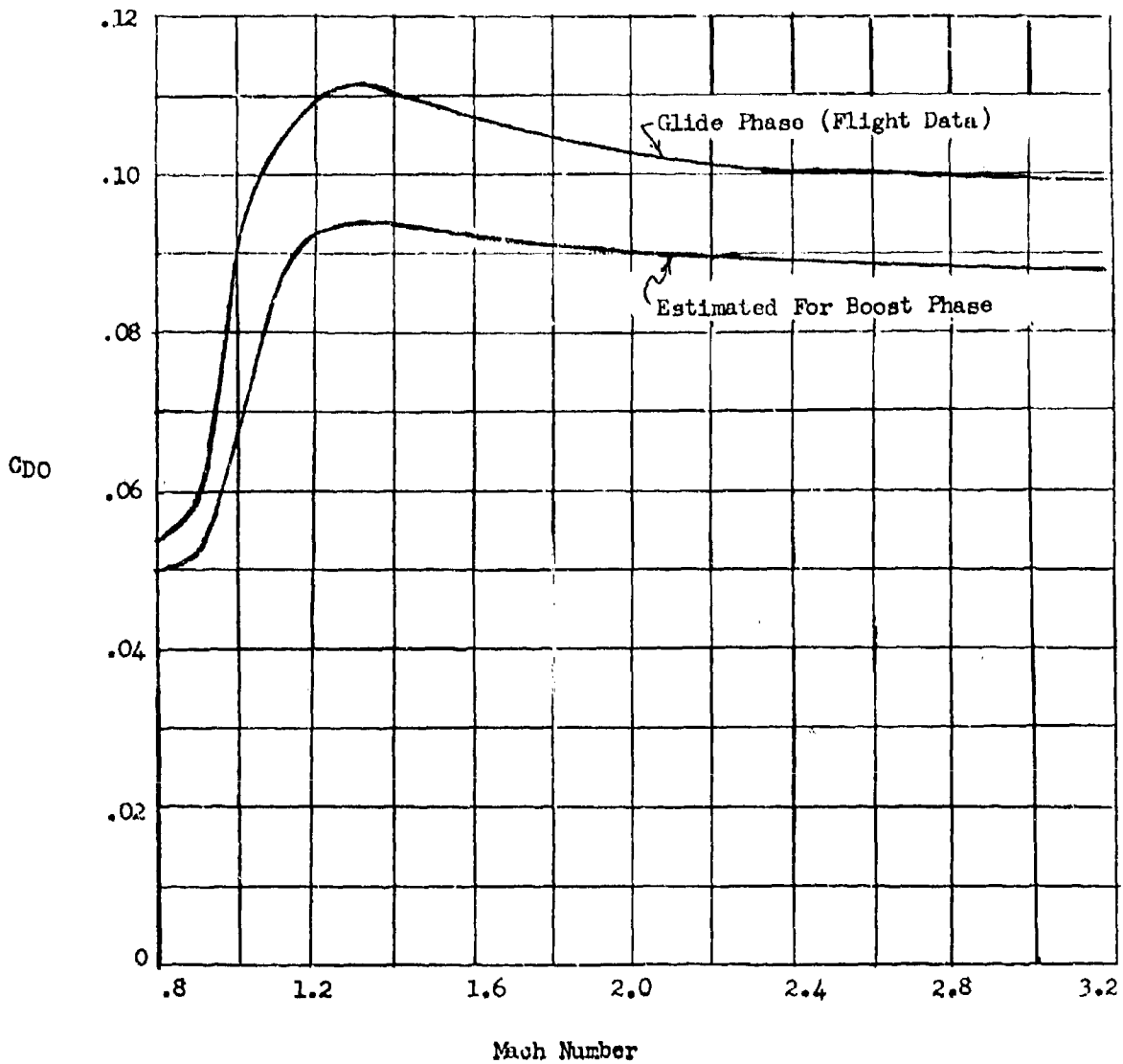


FIGURE 2. SPARROW III-B ZERO LIFT DRAG COEFFICIENTS VS MACH NUMBER

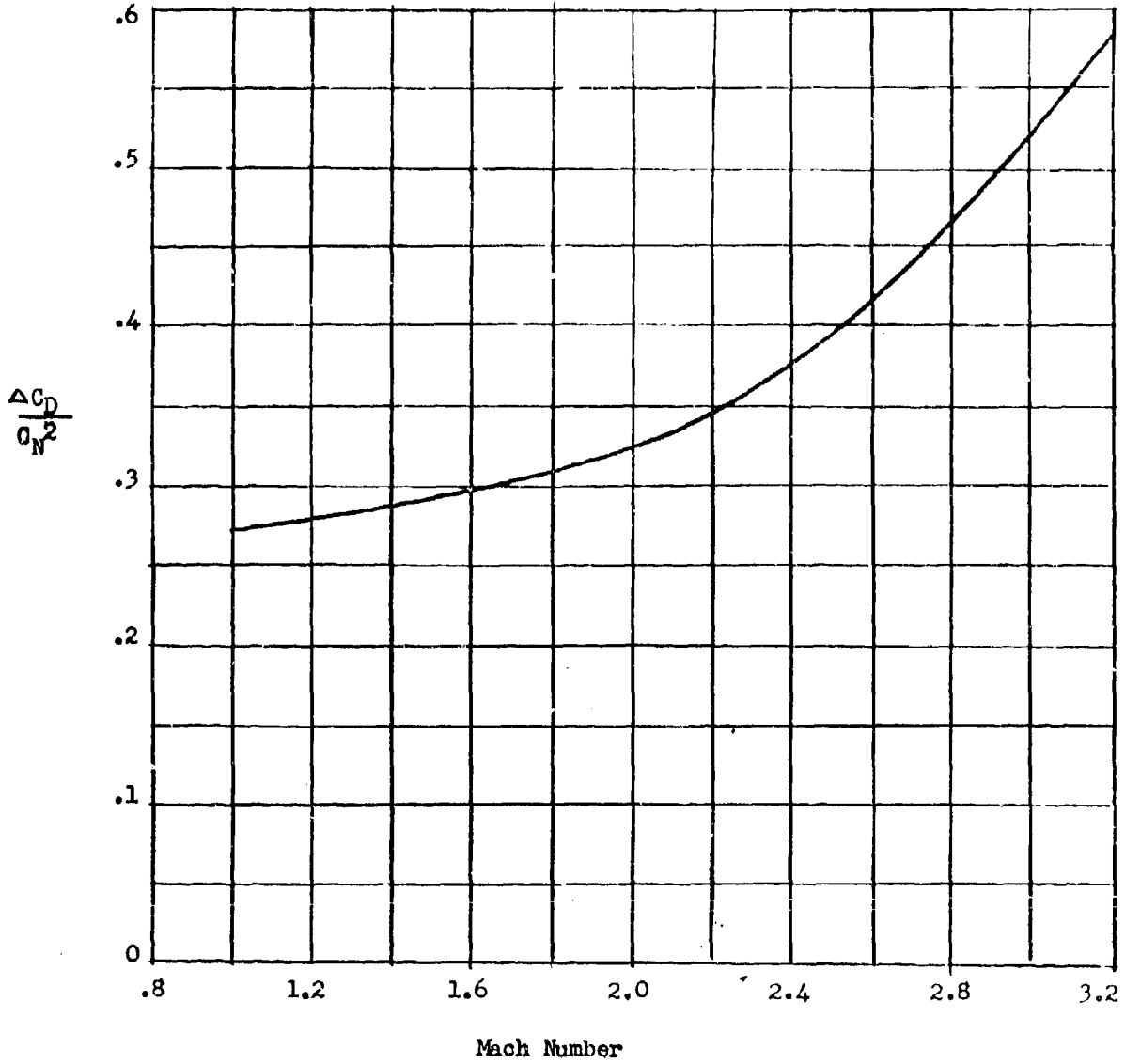


FIGURE 3. SPARROW III-B, DRAG DUE TO LIFT VS. MACH NUMBER

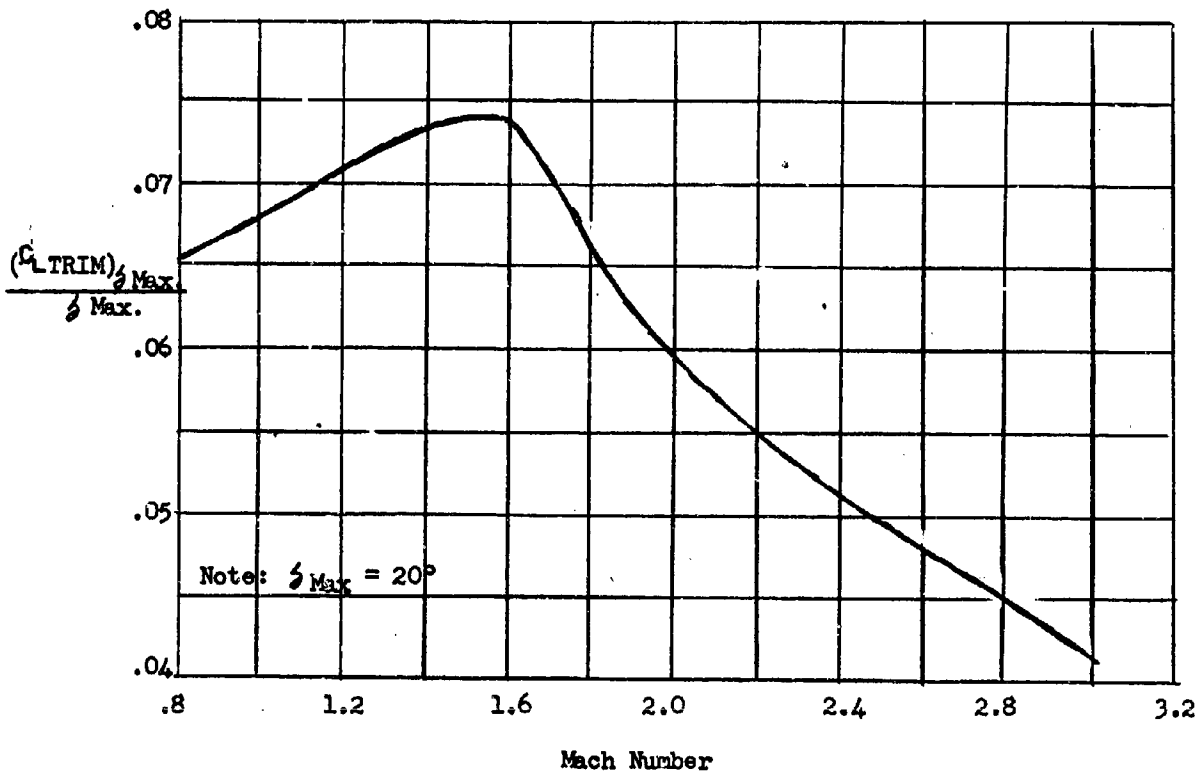


FIGURE 4. SPARROW III-B MAXIMUM TRIMMED LIFT COEFFICIENT VS MACH NUMBER



TABLE I
MISSILE CHARACTERISTICS

Weight	
At launch (W_L)	380 lb.
End of boost (W_G)	309 lb.
Impulse (at sea level)	16,000 lb. - sec.
Duration of boost (t_b)	1.8 sec.
Thrust (at sea level)	8889 lb.
Wing Area (each panel)	1.265 ft ²
Wing movement (each wing)	± 21 deg.
Maximum differential wing movement	5 deg.
Maximum acceleration	15 g's
Antenna gimbal limits	± 50 deg.
Maximum closing speed (V_c)	3500 ft/sec.
Maximum sweep rate of conical scan axis (λ_e)	± 20 deg./sec.

AUTOPILOT GAINS

Altitude Range ft.	K_5 deg/sec/g	K_6 g/deg/sec.	T_3 sec.	T_5 sec.
0 - 17	3.25	.12	.085	2.96
17K-32K	5.05	.12	.085	1.91
32K-46K	8.42	.12	.129	1.73
above 46K	12.33	.12	.129	1.18

CONFIDENTIAL



3. DISCUSSION

The above equations describe the missile trajectory from the time of lock-on until impact, but do not cover the period from launch to lock-on. This limitation was imposed by the fact that the required data is not available as yet.

The Sparrow III employs an "English Bias" signal to provide an open loop attitude command during the boost phase. However, since the exact manner in which this signal is fed to the surfaces and the switching cycles that are employed in the missile are not known, it is impossible to define the initial part of the trajectory at this time.

4. SUMMARY

This report has presented the equations which describe the Sparrow III trajectory from missile lock-on to impact. The equations have been presented for coplanar attacks in both the horizontal and vertical planes and assume a non-maneuvering target. The required English bias and firing sequence information has been requested and will be used to extend the scope of these equations when available.

It should also be noted that in view of the large number of different sources of information all of these missile parameters and assumptions should be approved by the customer before performing any calculations.

CONFIDENTIAL

CONFIDENTIAL



APPENDIX VI

NMSTR #5; Time Required For Pilot To Settle System Errors in X1A Type System

(Proprietary Information)

(McDonnell Aircraft Co.)

by

R. F. Wancowicz

7-15-57

003-103-100-C-90114

CONFIDENTIAL



TABLE OF CONTENTS

	Page
Synopsis	2
Method Used	2
Results and Conclusions	4
Summary	7
References	7
Curves of Radial Error vs. Settling Time	8-15
Tables	17-19
Appendix I - Details of Simulation	20
Appendix II - Calculation of Average G's Required To Reduce an Initial Error of 30° to an Error of 10°	24
Appendix III - Probability Distribution of System Steering Errors at Lock-On	29
Definition of Symbols	37

CONFIDENTIAL



SYNOPSIS

A study was initiated on the REAC to determine the system settling time of an airborne fire control system which flies a lead pursuit course and utilizes air-to-air guided missiles (Sparrow II and Sparrow III). System settling time, in this study, is defined as the time required to reduce the initial error to or below a specified value for a prescribed length of time. This prescribed time, T_s , is related to the time required to launch the missile and pilot delay time.

The results from this study are presented as curves in which the true radial error is plotted as a function of settling time. These results do not include the transient settling time of the radar, computer and auxiliaries. However, when the values of these parameters have been established, they may be added to the settling time curves of this report and the total system settling time can be obtained.

The probable errors to be expected when the interceptor is vectored into the proper zone using a pure collision vectoring technique were calculated. Using this data in conjunction with the settling time curves, the following conclusions were drawn.

1. In the case of an interceptor which has been vectored onto a position 20° off the nose of an oncoming target, the time required to reduce the initial error to or below 10° will be equal to or less than 10 seconds after lock-on for 74% of the cases flown. This time decreases to 8.2 seconds when only 43.5% of the cases flown are considered. Lock-on is assumed to be 15 nautical miles and $T_s = 3$ seconds.
2. In the case of an interceptor which has been vectored onto a position 40° off the nose of an oncoming target, the time required to reduce the initial error to or below 10° will be equal to or less than 10.3 seconds after lock-on for 64.6% of the cases flown. This time decreases to 8.2 seconds when only 38% of the cases flown are considered. As before, lock-on is assumed to occur at 15 nautical miles and $T_s = 3$ seconds.

METHOD USED

The three dimensional, pitch linearized, aerodynamic equations of an F4H-1 aircraft were simulated on the REAC. The values of the stability coefficients corresponded to a fighter velocity of M 1.91 and an altitude of 30,000 feet. These equations were then combined with the simulated equations of a lead pursuit course to provide steering information for the pilot located in the cockpit mock-up. Since the interceptor's weapons are assumed to be missiles, the error equations were mechanized to point the velocity vector rather than the armament control axis. The simulation equations are found in Appendix 1, page 20. The error presentation, in this case, consisted of a dot which the pilot was required to "fly" to the center of an oscilloscope. This was accomplished by actuating a stick which transmitted steering voltages to the airplane equations. The thermal and glint noise of the radar was simulated and added to the elevation and azimuth error signals at

CONFIDENTIAL

CONFIDENTIAL



the pilot's scope. This noise was simulated by shaping white noise through an $\frac{S}{(1 + 0.2 s)^2}$ filter. The magnitude at this point was adjusted to be 4 mil/sec.

RMS. This was then multiplied by $\frac{R}{V_0 + V_F}$ and filtered through $\frac{1}{1 + 0.5 s}$ before

being seen on the scope. The block diagram of the entire simulation is shown in figure 1, page 23.

Due to the limited time available for this study, it would have been impossible to investigate the effect of the variation of all of the parameters which affect settling time. Therefore, most of these parameters were made constant and only the initial angle-off the nose, τ_0 , and the initial error, ϵ_{A_0} , were varied.

The conditions used in this study are as follows:

- (1) $V_F = M 1.91$
- (2) $V_T = M 1.91$
- (3) Angle-off target's nose = $\pm 20^\circ$; $\pm 40^\circ$; $\pm 60^\circ$; $\pm 90^\circ$
- (4) two trained jet pilots
- (5) Noise as described above
- (6) $\epsilon_{A_0} = \pm 10^\circ, \pm 20^\circ, \pm 30^\circ$ (sign is dependent on sign of angle-off)
- (7) 0.5 seconds simple filter on error signals
- (8) scope sensitivity = 7°/inch
- (9) $V_0 = \text{constant} = 1000 \text{ fps}$
- (10) $R_0 = 10 \text{ n.m.}; 15 \text{ n.m.}$

The prescribed time, τ_{95} , was chosen to be 3 sec. and 6 sec. In order to alleviate any bias due to pilot anticipation, the angle-off and the initial errors were randomized. A list of the treatments used is found in Table 1, page 17. 15 runs were taken for each treatment and from the results of these runs, the median settling times and the 85% settling times for five values of allowable error were determined, and plotted versus the radial error. These plots appear in figures 3 to 34, pages 8 to 15. The initial attack picture is shown below in figure 2. All symbols are defined on page 37.

CONFIDENTIAL

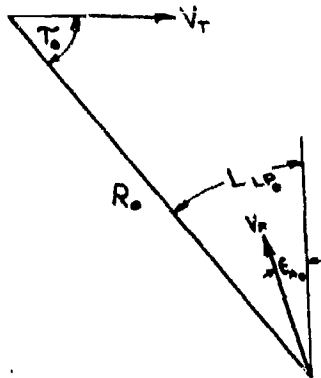


Figure 2: Initial Attack Picture for Settling Time Study

RESULTS AND CONCLUSIONS

Figures 3 to 34, pages 8 to 15 present the results of this study. In these curves, the radial error is plotted as a function of settling time. Instead of plotting curves for both plus and minus angles-off the nose, the data was combined so that only one curve appears for each angle-off.

In several of the cases, the radial error never diminished below a value between 2 and 9 degrees. When this occurred, the curves were extrapolated to this value and the extrapolations are indicated by broken lines on the figures.

For one case in particular ($\tau = +60^\circ$; $R = 10$ n.m.; Somerville) the 20° and 30° initial errors settled to a lower value than the 10° initial error. The explanation for this may be found by considering figure 35, below. In this figure;

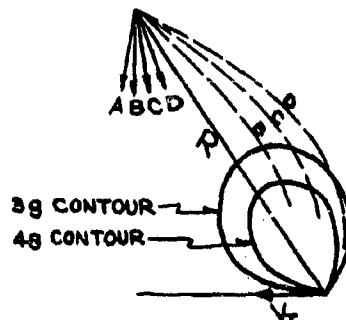


Figure 35: Sketch of Lead Pursuit Geometry Showing G Contours

- A is the interceptor heading on a lead pursuit course.
- B is the interceptor heading on a lead pursuit course with a 10° initial error.
- C is same as B except that the initial error is 20° .
- D is same as B except that the initial error is 30° .

CONFIDENTIAL



The dashed lines indicate the path of the interceptor in relative coordinates on a lead pursuit course. The 3 g contour represents the locus of points on a lead pursuit course at which the interceptor is "pulling 3 g's". It is seen that an initial error of 30° forces the interceptor into the rear of the 3 g contour; thus, the interceptor pilot has more time to reduce the error than he has on a course with only a 10° initial error. Since there is more time available with a 30° initial error than with a 10° initial error, it follows that the error will be reduced to a smaller value on the 30° initial error course.

The question which now arises is why the aforementioned phenomenon appeared in Somerville's runs but did not appear in Nupp's runs. This question is answered by referring to table 2, page 18, which tabulates the average "g's" pulled on each course for each pilot, when reducing an initial error of 30° to an error of 10°. The method by which the average g's were computed is found in Appendix 2, page 24. From the table, it is seen that while Somerville averaged between 3 and 4 g's on this particular course, Nupp averaged between 4 and 5 g's. Since Nupp was pulling more g's, he approached the target faster and brought the interceptor into the forward portion of the 3 g contour which shortened the available time and resulted in a higher value of radial error.

It may seem that the explanation above is contradictory to the old adage of "never pull more than 3 g's". However, this old adage refers to a situation in which the interceptor pilot is performing a precise task (for example; keeping the error zeroed while on course); and, in our case, there is nothing precise about pulling the stick back, rolling the airplane, and watching the error dot drift towards the center of the scope. As far as man and aircraft structural limits are concerned, Reference 1 indicates that an average man can withstand 5 g's of acceleration for 25 seconds (no g suit) without losing consciousness and Reference 2 states that the aircraft structural limitation is 6.5 g's. Since the longest time required to reduce a 30° error to 10° was about 16 seconds, it seems that the above limits have not been exceeded in the study.

In the majority of the radial error vs. settling time curves it is noted that a few seconds are required before the error stays below its initial value. The reason for this is that, initially, the error was increasing faster than the interceptor was turning (i.e., the pilot was not pulling enough g's). Since the pilots did not know initially what course they were going to fly (due to the random order of the courses) and since they could not tell what the initial error was (due to a limiting circuit which always kept the error dot on the scope face), the first second or two of each run was usually flown by "guessability". It is seen that the above phenomenon appeared more often in Somerville's runs than in Nupp's runs. This is to be expected since Somerville habitually pulled less g's than Nupp.

After reviewing Nupp's results on the small angle-off cases ($\tau_0 = 20^\circ$ and 40°) it was decided to increase the initial range, R_0 , to 15 nautical miles for Somerville's runs. It was found that the system was much easier to fly with the larger R_0 (the g requirements were considerably lower and the error was reduced to a lower value than was possible at 10 nautical miles). This fact stresses the importance of greater detection ranges.

The differences between using a V_0 of 1000 ft/sec. rather than $V_0 = 1291$ ft/sec are illustrated in figure 45, page 16. In this figure, lead pursuit courses beginning at $R_0 = 10$ n.m. have been plotted for $\tau_0 = 20^\circ, 40^\circ$ and 60° using values of V_0 of 1091 ft/sec and 1291 ft/sec. The reason that 1091 ft/sec was used instead of

CONFIDENTIAL



1000 ft/sec was that the calculations had previously been made for another study using $V_o = 1091$ ft/sec. Since figure 45 indicates a very small difference between $V_o = 1091$ ft/sec and $V_o = 1291$ ft/sec, it follows that an even smaller difference exists between $V_o = 1091$ ft/sec and $V_o = 1000$ ft/sec.

Appendix III, page 29, by R. B. Tucker of the Analytical Section describes the probable errors to be expected when the interceptor is vectored into the proper zone using a pure collision vectoring technique. Although these calculations were made for $V_F = 1940$ fps. and $V_o = 1291$ fps. the results may be applied to the study without excessive loss in accuracy. Assuming a lock-on range of 15 nautical miles it is seen that for $\tau_o = 60^\circ$ and $V_T = 1.0$, about 48% of all runs will have an

initial error of 30° or greater. This justifies the use of a 30° initial error in the study and also indicates that a more accurate vectoring system is needed if high angles-off are to be used.

Since the curves from Appendix III assumed a lock-on range of 15 nautical miles, they may be incorporated with the radial error vs. settling time curves which used an R_o of 15 nautical miles to provide the following information.

1. In the case of an interceptor which has been vectored onto a position 20° off the nose of an oncoming target, the time required to reduce the initial error to or below 10° will be equal to or less than 10 seconds after lock-on for 74% of the cases flown. This time decreases to 8.2 seconds when only 43.5% of the cases flown are considered. Lock-on is assumed to be 15 nautical miles and $\tau_s = 3$ seconds.
2. In the case of an interceptor which has been vectored onto a position 40° off the nose of an oncoming target, the time required to reduce the initial error to or below 10° will be equal to or less than 10.3 seconds after lock-on for 64.6% of the cases flown. This time decreases to 8.2 seconds when only 38% of the cases flown are considered. As before, lock-on is assumed to occur at 15 nautical miles and $\tau_s = 3$ seconds.
3. Nothing can be said for the case where the interceptor is vectored to 60° off the nose since the settling time data was gathered for an R_o of 10 nautical miles and the curves from Appendix III were drawn for an R_o of 15 nautical miles. Even if numbers could be specified for this condition, their meaning would not be too significant since only 52% of all runs had initial errors of 30° or less when considering the 15 mile lock-on range. This percentage would even be less if a 10 mile lock-on range were considered.

CONFIDENTIAL



SUMMARY

The system settling time of an airborne fire control system utilizing air-to-air guided missiles and flying lead pursuit was determined on the REAC. This settling time is defined as the time required to reduce the initial error to or below a specified value for a prescribed length of time. The results were presented as curves of radial error vs. settling time and the total settling time (including settling time of the radar and computer and effects of allowable launching error) may be found by shifting the ordinates of these curves to allow for the effects of the aforementioned parameters.

The probable errors to be expected when the interceptor is vectored into the proper zone using a pure collision vectoring technique were calculated. Using this data in conjunction with the settling time curves, certain conclusions were drawn which are restated below for convenience.

1. In the case of an interceptor which has been vectored onto a position 20° off the nose of an oncoming target, the time required to reduce the initial error to or below 10° will be equal to or less than 10 seconds after lock-on for 74% of the cases flown. This time decreases to 8.2 seconds when only 43.5% of the cases flown are considered. Lock-on is assumed to be 15 nautical miles and $\tau_s = 3$ seconds.
2. In the case of an interceptor which has been vectored onto a position 40° off the nose of an oncoming target, the time required to reduce the initial error to or below 10° will be equal to or less than 10.3 seconds after lock-on for 64.6% of the cases flown. This time decreases to 8.2 seconds when only 38% of the cases flown are considered. As before, lock-on is assumed to occur at 15 nautical miles and $\tau_s = 3$ seconds.

REFERENCES

1. "High Speed Flight" by E. Ower and J. Nayler; Philosophical Library, New York, 1957
2. McDonnell Report No. 4518, Volume 1, "Fighter Aerodynamic Status Report" Confidential, 12-16-55 (Revised 4-9-56).
3. "NMSTR#1, F4H-1 Stability Derivatives (Wind and Body Axes) and Dynamic Characteristics (Proprietary Information, McDonnell Aircraft Co.)" by R. B. Tucker, 5-1-57.

CONFIDENTIAL

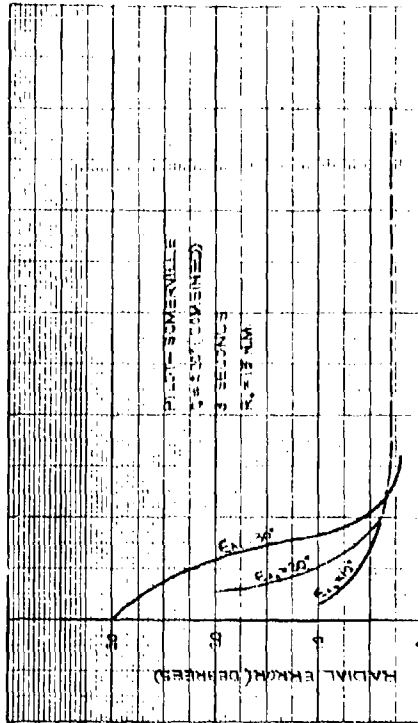


FIGURE 19 - BEST SETTLING TIME CHARACTERISTICS

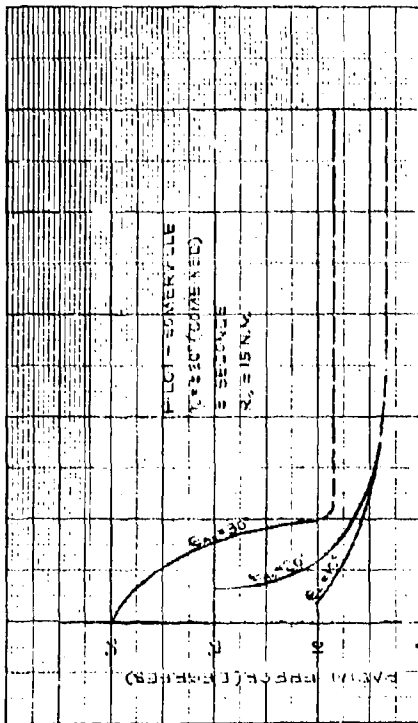


FIGURE 20 - BEST SETTLING TIME CHARACTERISTICS

100

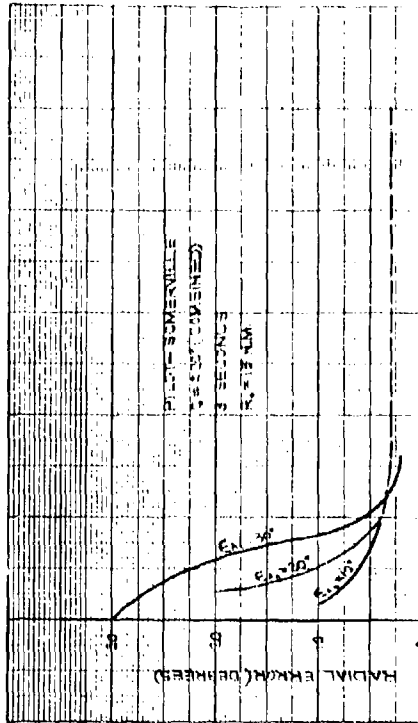


FIGURE 21 - MEDIAN SETTLING TIME CHARACTERISTICS

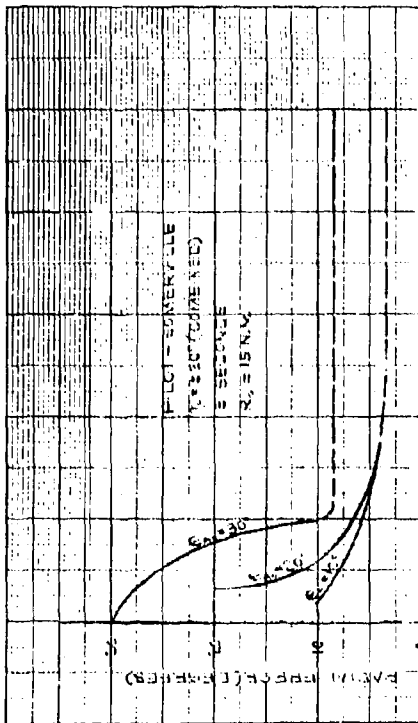
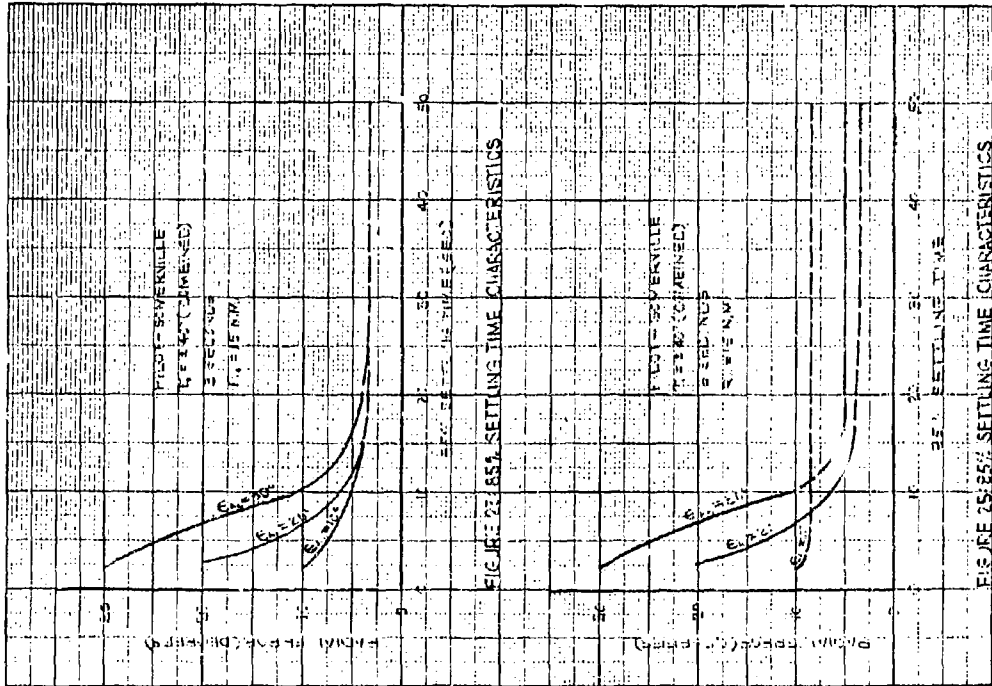
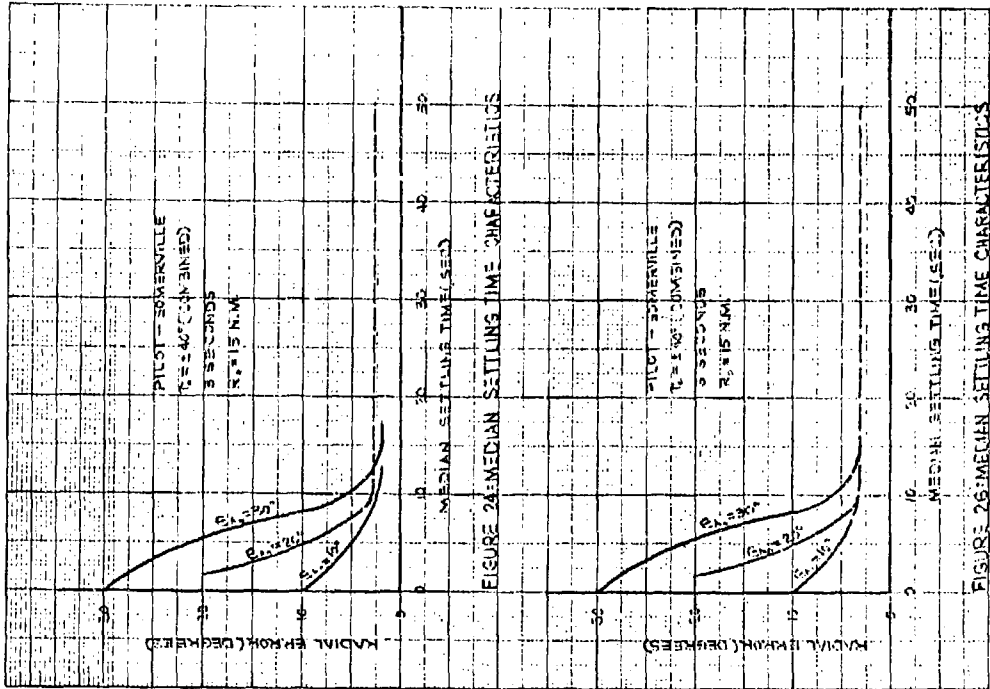


FIGURE 22 - MEDIAN SETTLING TIME CHARACTERISTICS



1 C 1

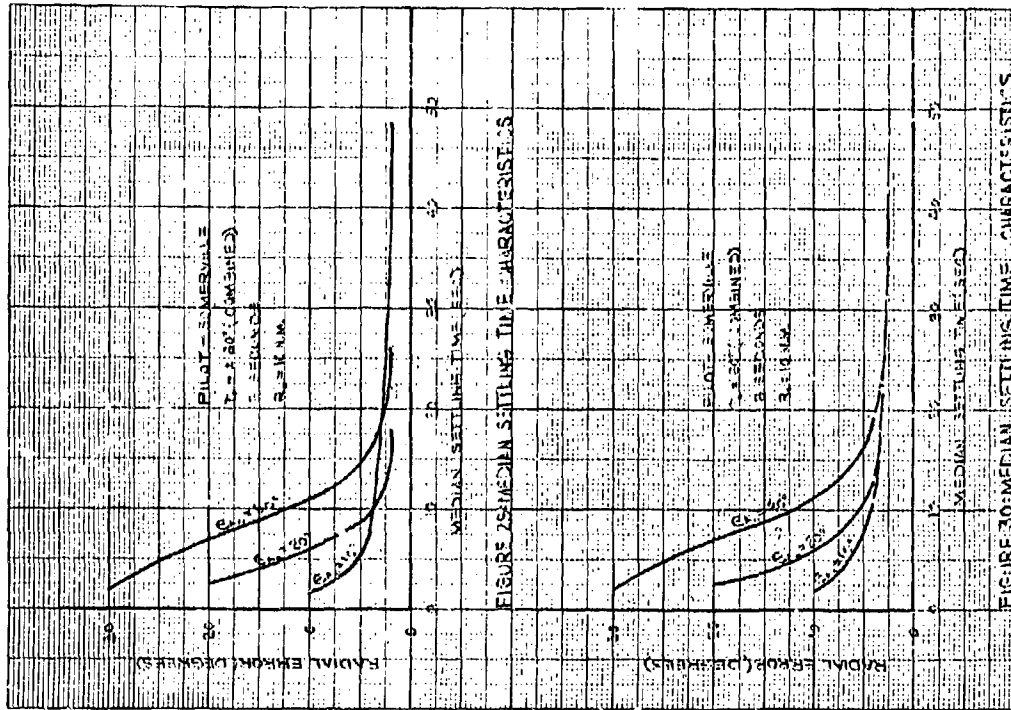


FIGURE 25-MEDIAN SETTLING TIME CHARACTERISTICS

FIGURE 30-MEDIAN SETTLING TIME CHARACTERISTICS

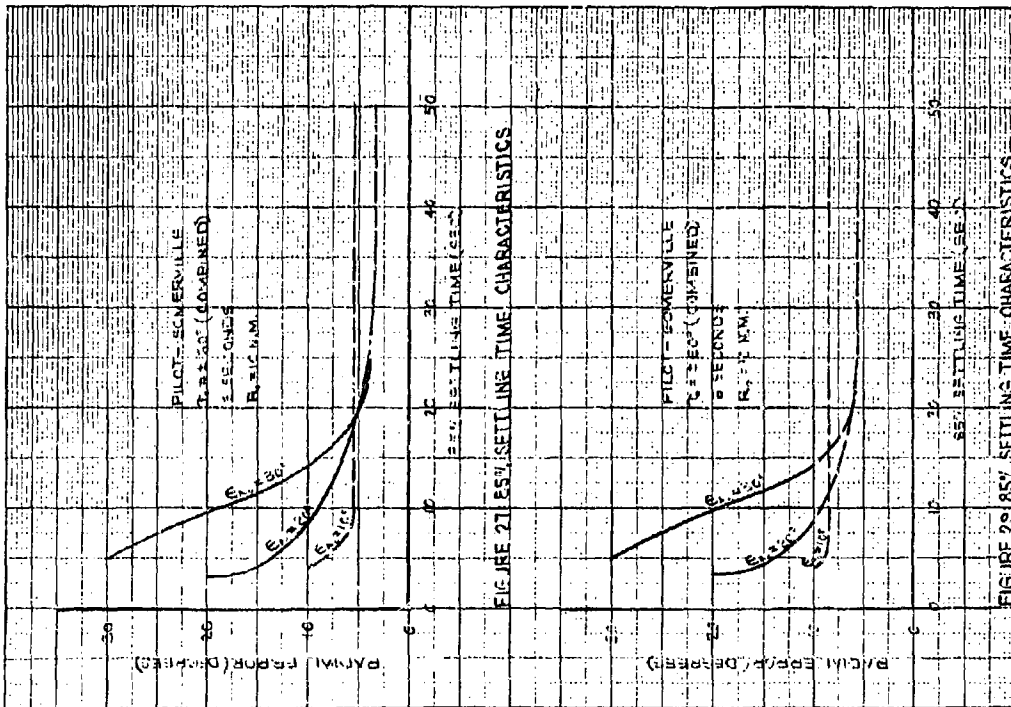
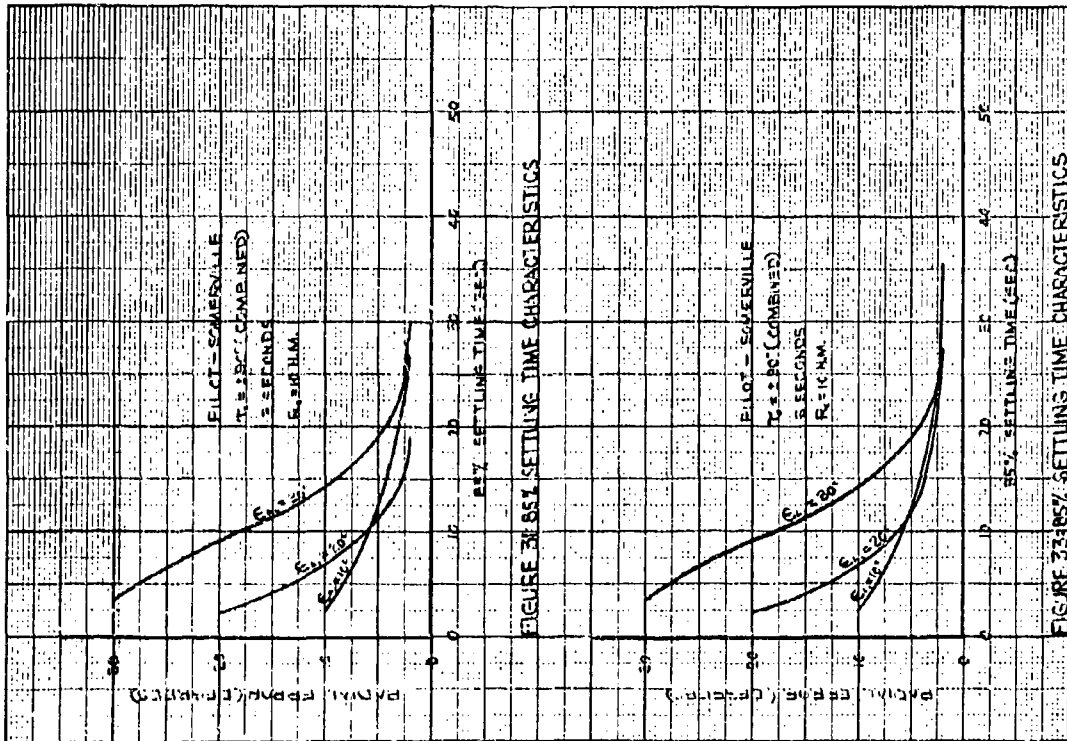
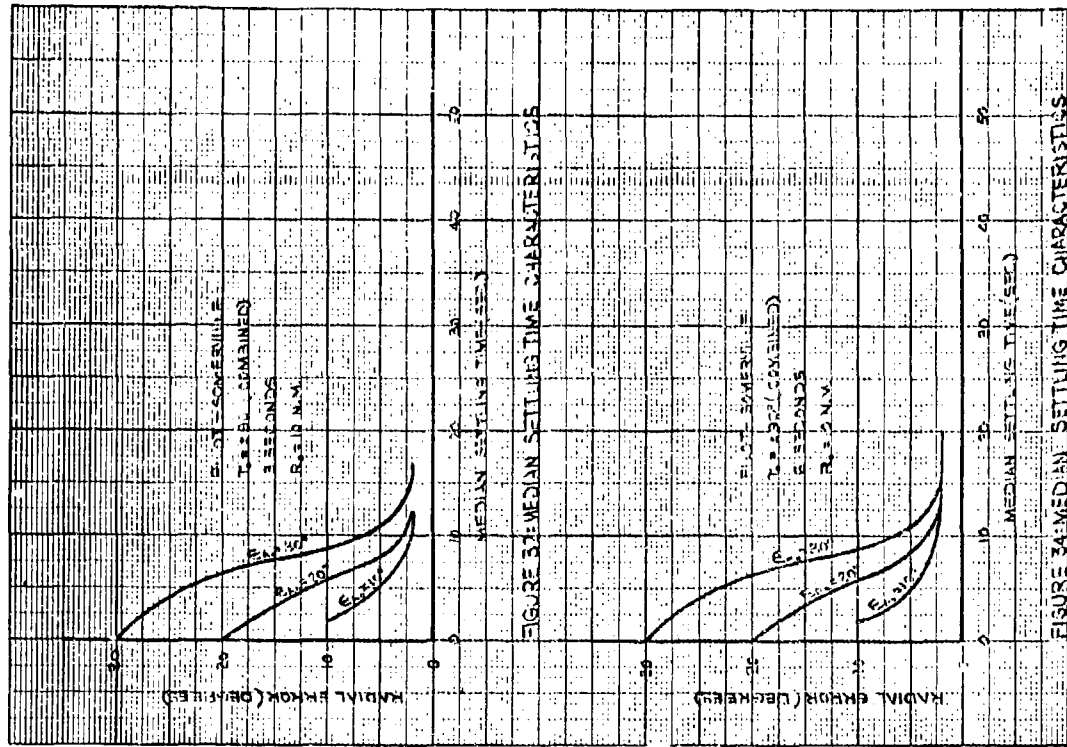


FIGURE 21-85% SETTLING TIME CHARACTERISTICS

FIGURE 20-85% SETTLING TIME CHARACTERISTICS



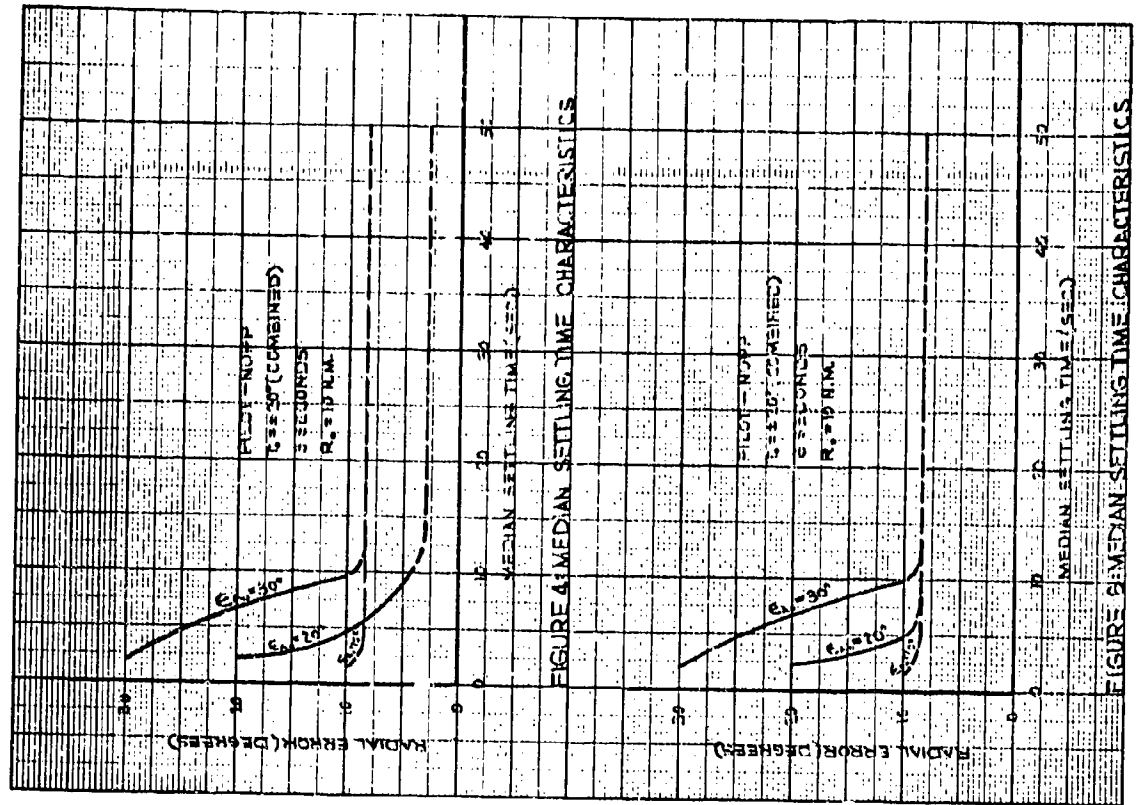


FIGURE 4: MEDIAN SETTLING TIME CHARACTERISTICS

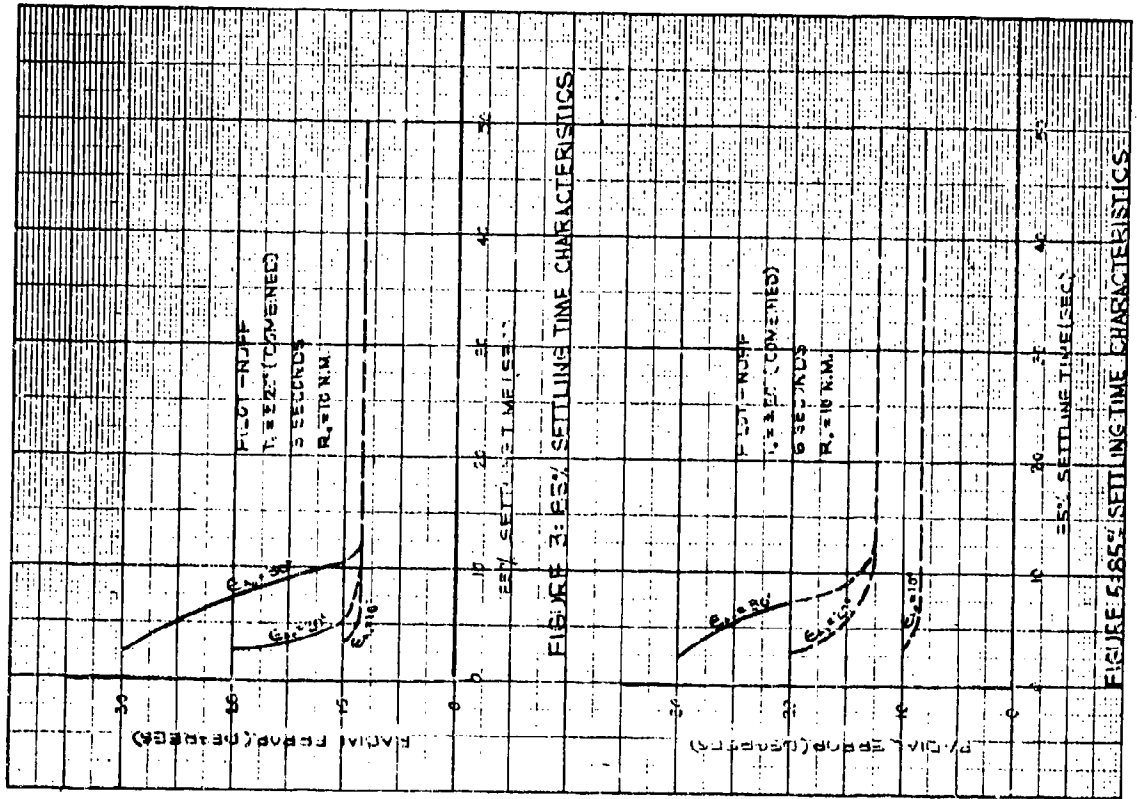
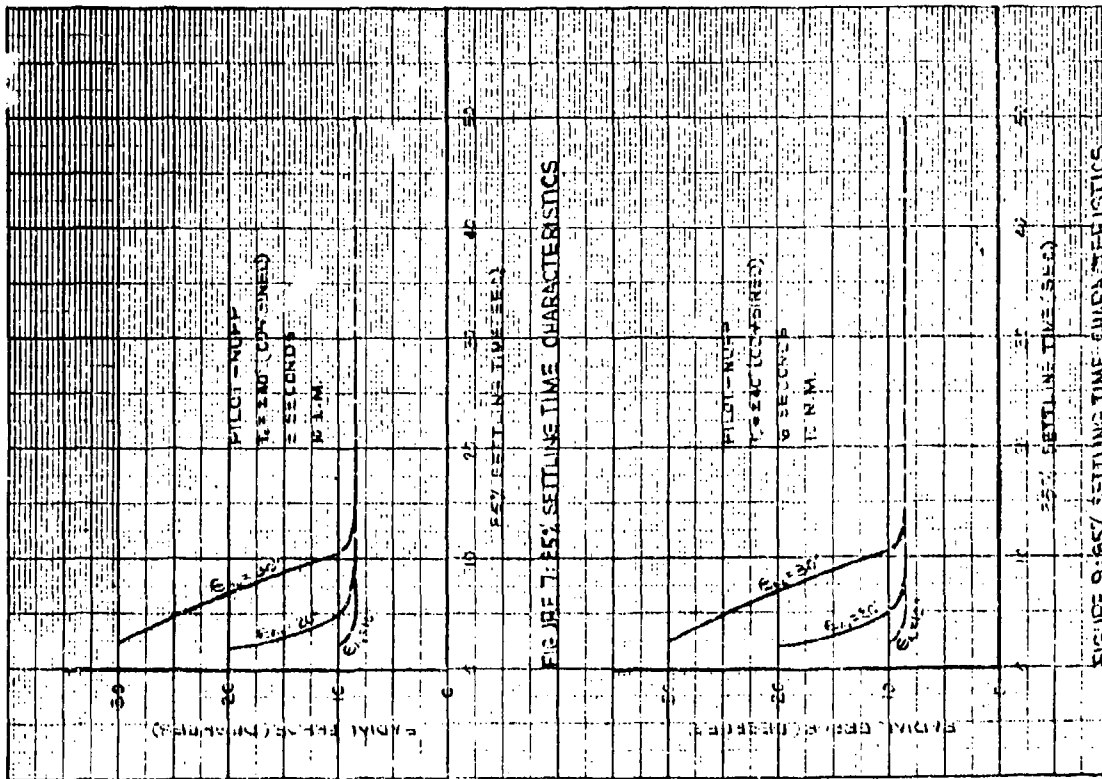
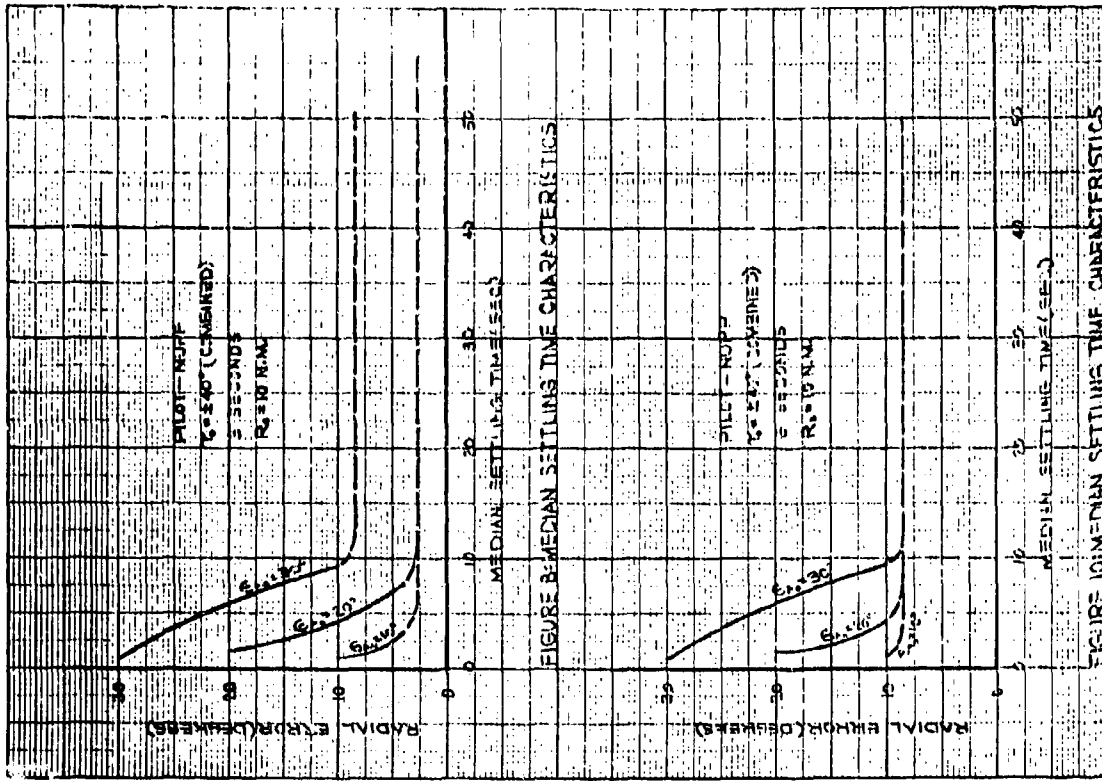


FIGURE 3: 65% SETTLING TIME CHARACTERISTICS



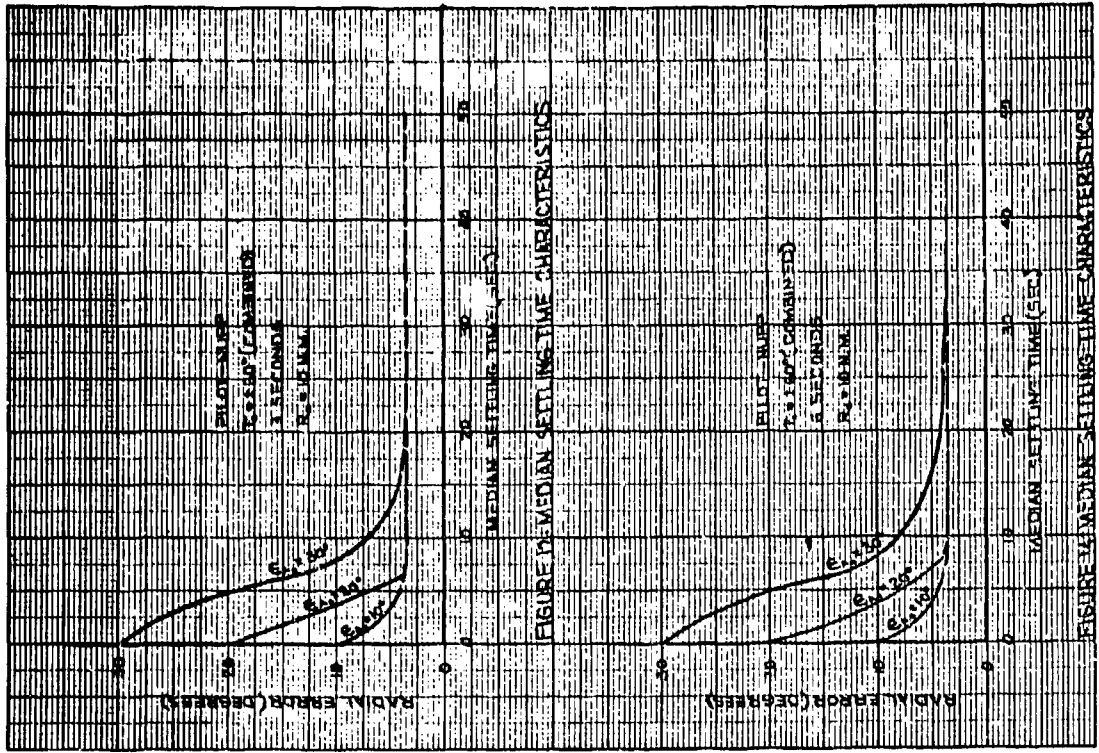


FIGURE 13. MEDIAN SETTLING TIME CHARACTERISTICS

FIGURE 13. MEDIAN SETTLING TIME CHARACTERISTICS

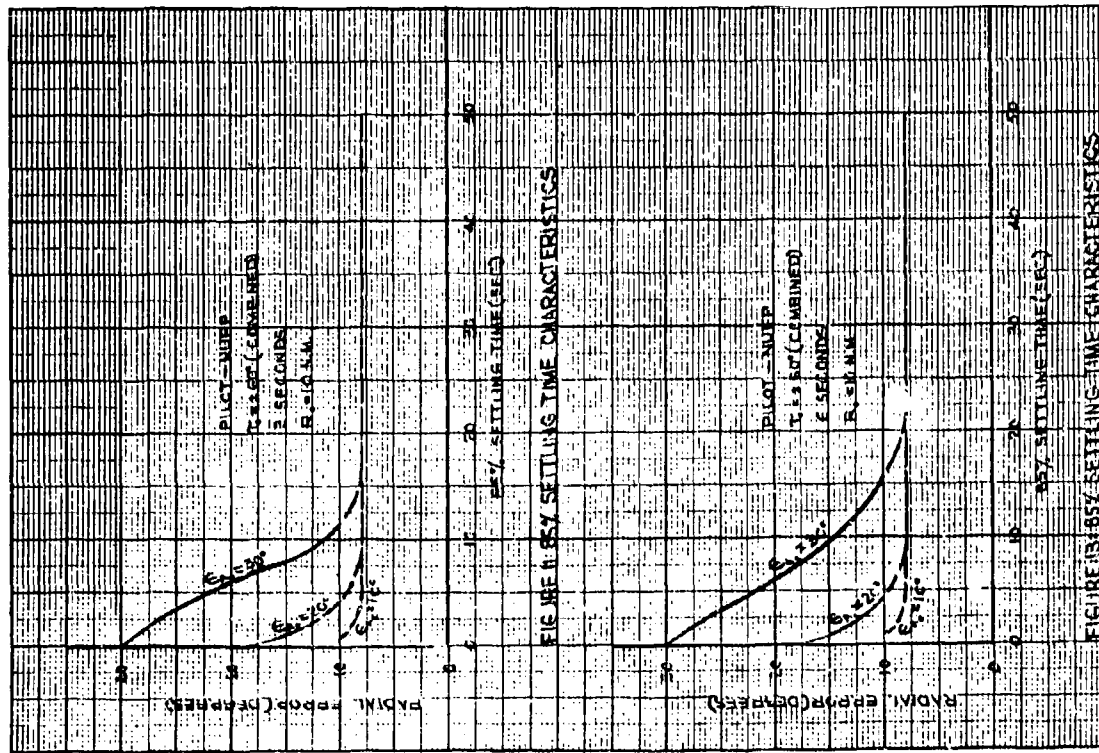


FIGURE 14. 85% SETTLING TIME CHARACTERISTICS

FIGURE 14. 85% SETTLING TIME CHARACTERISTICS

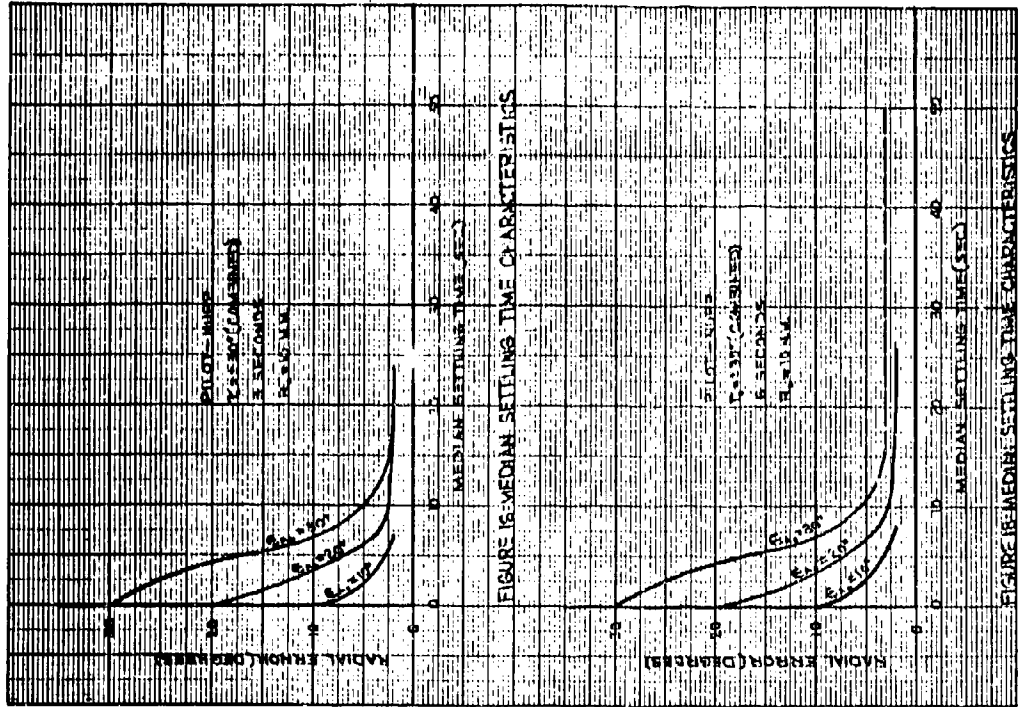


FIGURE 15. MEDIAN SETTLING TIME CHARACTERISTICS

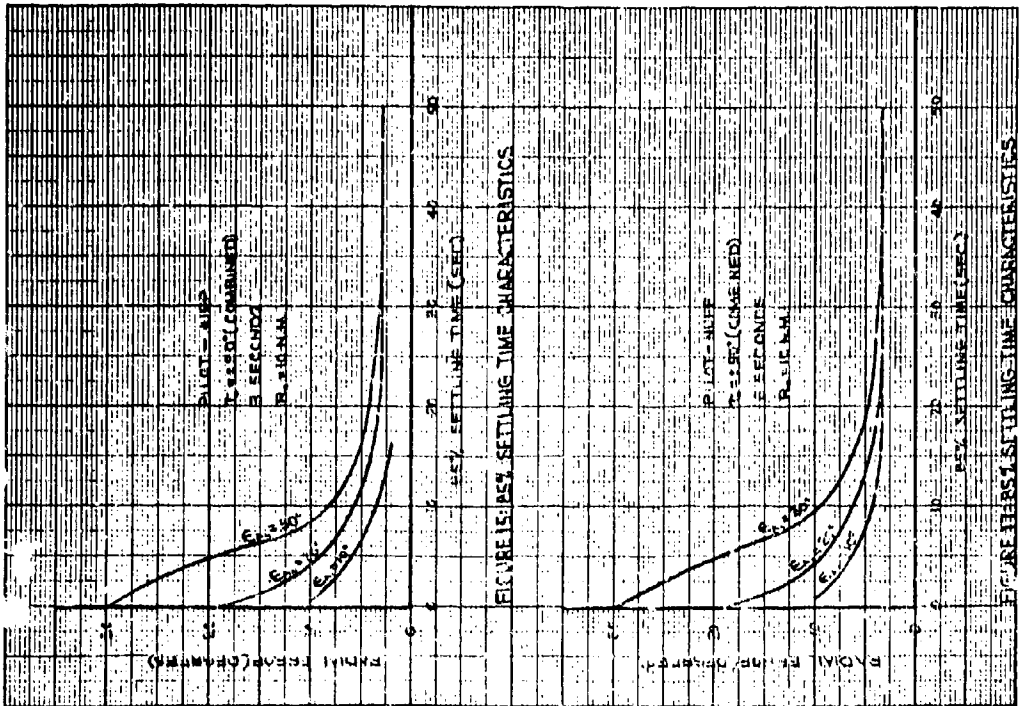


FIGURE 16. 1ST SETTLING TIME CHARACTERISTICS

- 17 -

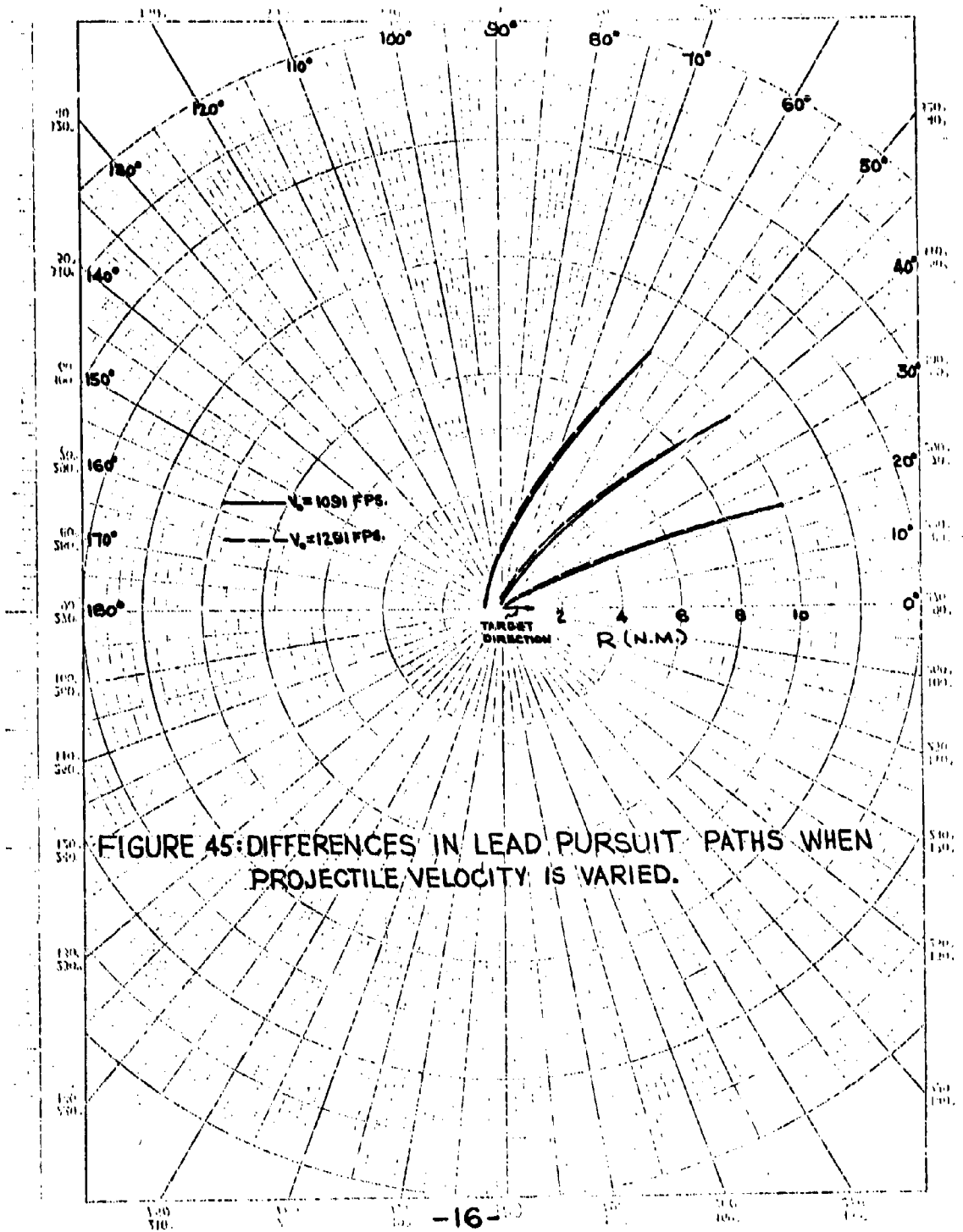


FIGURE 45: DIFFERENCES IN LEAD PURSUIT PATHS WHEN PROJECTILE VELOCITY IS VARIED.



<u>TREATMENT</u>	<u>R₀ (n.m.)</u>	<u>τ₀ (deg)</u>	<u>ε_{A0} (deg)</u>
1, 13	10 ↓	+ 20	+ 10
2, 14		+ 20	+ 20
3, 15		+ 20	+ 30
4, 16		+ 40	+ 10
5, 17		+ 40	+ 20
6, 18		+ 40	+ 30
7, 19		+ 60	+ 10
8, 20		+ 60	+ 20
9, 21		+ 60	+ 30
10, 22		+ 90	+ 10
11, 23		+ 90	+ 20
12, 24		+ 90	+ 30
25, 31	15 ↓	+ 20	+ 10
26, 32		+ 20	+ 20
27, 33		+ 20	+ 30
28, 34		+ 40	+ 10
29, 35		+ 40	+ 20
30, 36		+ 40	+ 30

NOTE: Treatments 1-12, and 25-30 refer to plus value of τ₀ and ε_{A0}
 Treatments 13-24, and 31-36 refer to minus values of τ₀ and ε_{A0}

TABLE 1: LIST OF CONFIGURATIONS USED IN STUDY



<u>R₀</u>	<u>T₀</u>	<u>Pilot</u>	<u>Cumulative Percentage of Runs Settled to 10°</u>	<u>Avg. g's</u>
15	40	S	50	3-4
15	20	S	50	3-4
15	20	S	85	3-4
15	40	S	85	3-4
10	60	S	50	3-4
10	60	S	85	3-4
10	90	S	50	3-4
10	90	S	85	3-4
10	20	N	50	4-5
10	20	N	85	4-5
10	40	N	50	4-5
10	40	N	85	4-5
10	60	N	50	4-5
10	60	N	85	3-4
10	90	N	50	4-5
10	90	N	85	3-4

TABLE 2.- AVERAGE G'S REQUIRED TO REDUCE AN INITIAL 30° ERROR TO AN ERROR OF 10°.



T_0	N_g	t	R_0
20	3	-	10
↓	4	-	↓
↓	5	6.6	↓
40	3	-	↓
↓	4	-	↓
↓	5	7.1	↓
60	3	-	↓
↓	4	10.9	↓
↓	5	6.6	↓
90	3	16.9	↓
↓	4	8.6	↓
↓	5	6.0	↓
20	3	-	15
↓	4	7.4	↓
↓	5	5.3	↓
40	3	-	↓
↓	4	7.8	↓
↓	5	5.5	↓

TABLE 3: TIME REQUIRED TO REDUCE AN INITIAL ERROR OF 30° TO AN ERROR OF 10° WHILE FLYING A CONSTANT LOAD FACTOR COURSE.



APPENDIX I - DETAILS OF SIMULATION

The following equations are those which were used in the interceptor settling time study. The airplane is an F4H-1 flying at 30,000 feet whose velocity is M1.91.

Aircraft Equations

$$\dot{p} = l_{\delta a} \delta a + l_p p + V_F l_v \beta + l_{\delta r} \delta r + l_r r$$

$$\dot{q} = m_{\delta e} \delta e + V_F m_w \alpha + m_q q$$

$$\dot{r} = n_{\delta a} \delta a + n_{\delta r} \delta r + V_F n_v \beta + n_r r$$

$$\dot{\alpha} = z_{\delta e} \delta e + z_w \alpha + z_q q + \frac{57.3 g}{V_F} \cos \phi + \text{BALANCE}$$

$$\dot{\beta} = y_{\delta r} \delta r + y_v \beta + y_r r + \frac{57.3 g}{V_F} \sin \phi$$

Orientation Angles

$$\delta_r = \frac{K_r \Gamma S}{1 + 1.5 S} - K_{ry} \beta$$

where $\begin{cases} K_r = 1.25 \\ K_{ry} = 1.00 \end{cases}$

$$\phi = \frac{1}{3} \left[p + \frac{\theta + \theta_1}{57.3} \psi \right]$$

$$\theta = \frac{1}{3} [q \cos \phi - r \sin \phi]$$

$$\psi = \frac{1}{3} [q \sin \phi + r \cos \phi]$$

$\theta_1 = -1.24^\circ$

Target Velocity in Earth Coordinates

$$\dot{X}_T = \text{CONSTANT} = M 1.91$$

$$\dot{Y}_T = \dot{Z}_T = 0$$

Target Velocity in Aircraft Coordinates

$$u_T = \dot{X}_T \cos \psi$$

$$v_T = \dot{X}_T \left[\left(\frac{\theta + \theta_1}{57.3} \right) \sin \phi \cos \psi - \cos \phi \sin \psi \right]$$

$$w_T = \dot{X}_T \left[\left(\frac{\theta + \theta_1}{57.3} \right) \cos \phi \cos \psi + \sin \phi \sin \psi \right]$$



Range Rate in Aircraft Coordinates

$$\dot{R}_x = U_T - V_F \cos \alpha_o$$

$$\dot{R}_y = V_T - \frac{V_F \beta}{57.3}$$

$$\dot{R}_z = W_T - \frac{V_F \alpha}{57.3} - V_F \sin \alpha_o$$

$$\alpha_o = -1.24^\circ$$

Range Rate in Antenna Coordinates

$$\dot{R} = [\dot{R}_x \cos \lambda_a + \dot{R}_y \sin \lambda_a] \cos \lambda_e - \dot{R}_z \sin \lambda_e$$

$$R\omega_k = -\dot{R}_x \sin \lambda_a + \dot{R}_y \cos \lambda_a$$

$$-R\omega_j = [\dot{R}_x \cos \lambda_a + \dot{R}_y \sin \lambda_a] \sin \lambda_e + \dot{R}_z \cos \lambda_e$$

Lead Angle Rates

$$\dot{\lambda}_a = \omega_k \cos \lambda_e - \omega_i \sin \lambda_e - r$$

$$\dot{\lambda}_e = \omega_j + p \sin \lambda_a - q \cos \lambda_a$$

$$\omega_i = [p \cos \lambda_a + q \sin \lambda_a] \cos \lambda_e - (r + \dot{\lambda}_a) \sin \lambda_e$$

$$\lambda_e = 1.74^\circ$$

True Errors

$$\epsilon_{T_A} = \frac{57.3}{V_o + V_F} [R\omega_k + V_o \sin \lambda_a]$$

$$\epsilon_{T_B} = -\frac{57.3}{V_o + V_F} [R\omega_j + V_o \sin \lambda_e \cos \lambda_a + V_o \cos \lambda_e \left(\frac{\alpha - \Gamma_F}{57.3}\right)]$$

$$\Gamma_F = 0.5^\circ$$



The following table lists the values of the aerodynamic coefficients used in this study. These values were obtained from Reference 3.

$l_{\delta z} = -28.0$	$n_{\dot{r}} = 0.00939$
$l_p = -1.725$	$n_r = -0.456$
$l_r = 0.0267$	$\delta_{\delta z} = -0.138$
$l_{\delta r} = 2.92$	$\delta_{\dot{r}} = 1.0$
$l_r = 0.466$	$\delta_w = -1.083$
$m_{\delta z} = -61.0$	$y_{\dot{r}} = -0.255$
$m_w = -0.0579$	$y_{\delta r} = 0.00478$
$m_z = -1.259$	$y_r = -1.0$
$n_{\delta z} = 0.115$	
$n_{\delta r} = -2.36$	

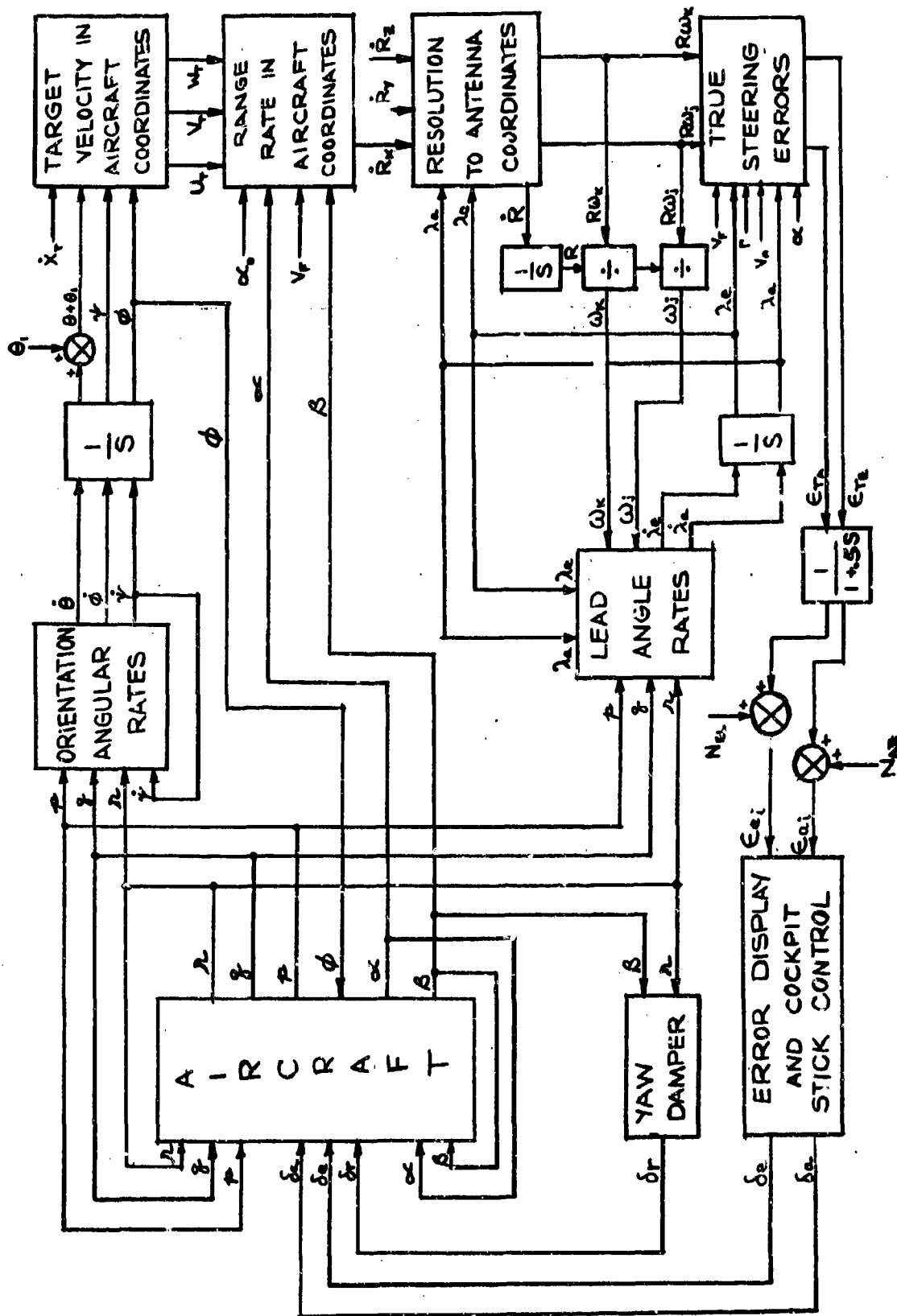


FIGURE 1: BLOCK DIAGRAM OF SIMULATION



APPENDIX II - CALCULATION OF AVERAGE G'S REQUIRED TO
REDUCE AN INITIAL ERROR OF 30° TO AN ERROR OF 10°

The geometrical equations of an interceptor flying a constant load factor course in Cartesian target coordinates were developed by J. F. Buchan of the Analytical Section. These equations appear below. All symbols are defined on page 37.

$$R_x = R_o \cos T_o - \frac{V_t t}{6080} + \frac{V_F}{6080 \psi} [\sin(T_o + L_o) - \sin(\psi t + T_o + L_o)] \quad (1)$$

$$R_y = R_o \sin T_o + \frac{V_F}{6080 \psi} [\cos(\psi t + T_o + L_o) - \cos(T_o + L_o)] \quad (2)$$

$$\psi = \frac{g}{V_F} \sqrt{n_z^2 - 1} \quad (3)$$

$$L_o = L_{LR} - \epsilon_{A_o} \quad (4)$$

$$L_{LR} = \sin^{-1} \left[\frac{V_t}{V_o + V_F} \sin T_o \right] \quad (5)$$

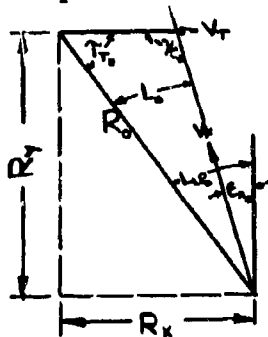
$$T = \tan^{-1} \left[\frac{R_y}{R_x} \right] \quad (6)$$

$$L = \psi t + T_o + L_o - T \quad (7)$$

The assumptions are:

1. $V_F = \text{constant}$
2. Interceptor and target are at the same altitude.
3. Target flies straight line, constant speed course.

The initial space picture is shown below.





For each condition flown on the REAC, the following scheme was used to calculate the average g's required to reduce an initial error of 30° to an error of 10°. A sample set of the intermediate curves needed to perform the calculations is included in this Appendix. The sample condition is one in which $\tau_0 = 60^\circ$; $R_0 = 10$ n.m.; $N_z = 3, 4,$ and 5 g's, $V_F = V_T = 1897$ fps.

Considering first the case where $N_z = 5$, equations (1) to (6) were used to obtain τ for $t = 0, 5, 10, 15, 20, 25$ and 30 seconds. Once τ is known, equation (5) may be used without the subscripts to calculate values of L_{LP} as a function of τ . Also equation (7) may be used to obtain L as a function of τ . Now, L and L_{LP} are plotted vs. τ on the same graph paper as shown in figure 36. From equation (4) (without subscripts), $\epsilon_A = L_{LP} - L$. Therefore, a pair of dividers may be used to find the value of τ at which $\epsilon_A = 10^\circ$. Finally, τ is plotted vs. time (figure 37); thus the time at which $\epsilon_A = 10^\circ$ may be read from this curve. This value of time is the time required to reduce an initial 30° error to a 10° error while pulling a constant 5 g's.

The above procedure was repeated for $N_z = 4$ and $N_z = 3$. The plots of L_{LP} and L vs. τ for these two cases are shown in figures 38 and 39. It is interesting to note that for $N_z = 3$, ϵ_A never diminished to 10° but reached a minimum of 24°. Therefore, it would be impossible to attain a lead pursuit course at these conditions without exceeding 3 g's.

The procedure was again repeated for all of the configurations used in the study. The times to reach 10° were tabulated and appear in Table 3, page 19. The times from Table 3 were then used in conjunction with the radial error vs. settling time curves to predict the average g's pulled for each condition. These average g's are tabulated and appear in Table 2, page 18.

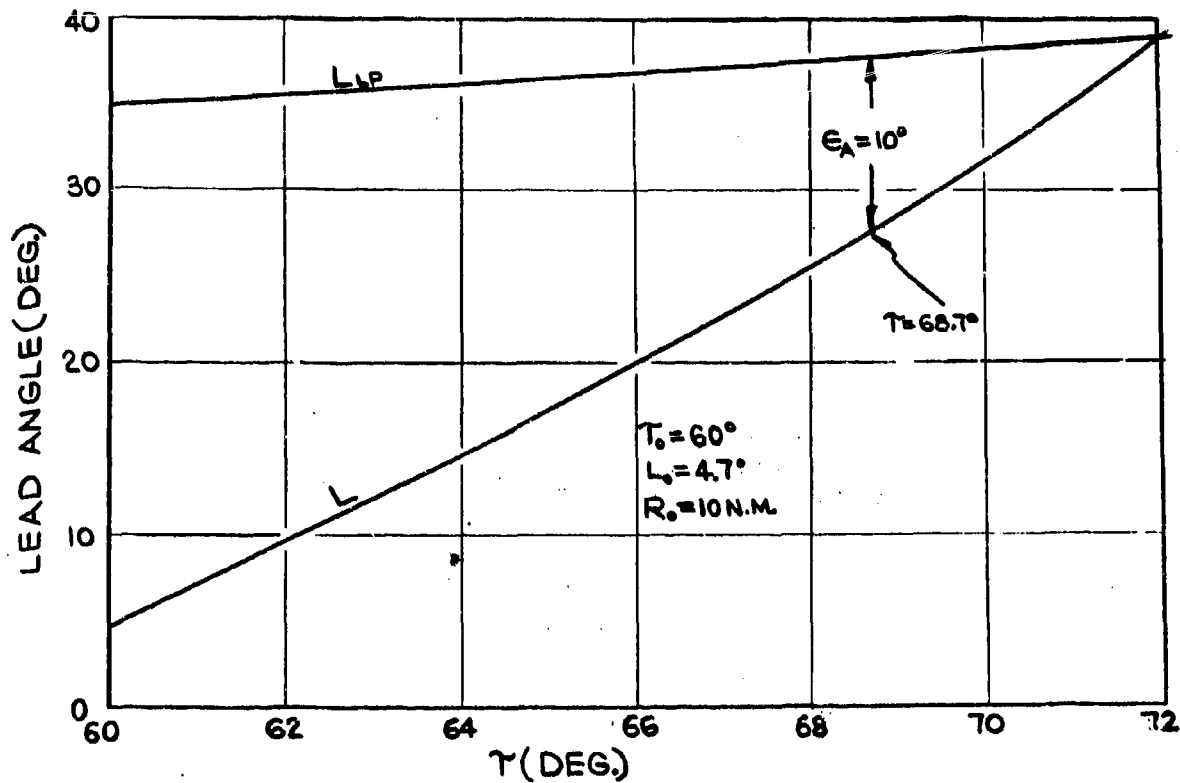


FIGURE 36 : LEAD ANGLES VS. γ ; $n_z = 5$

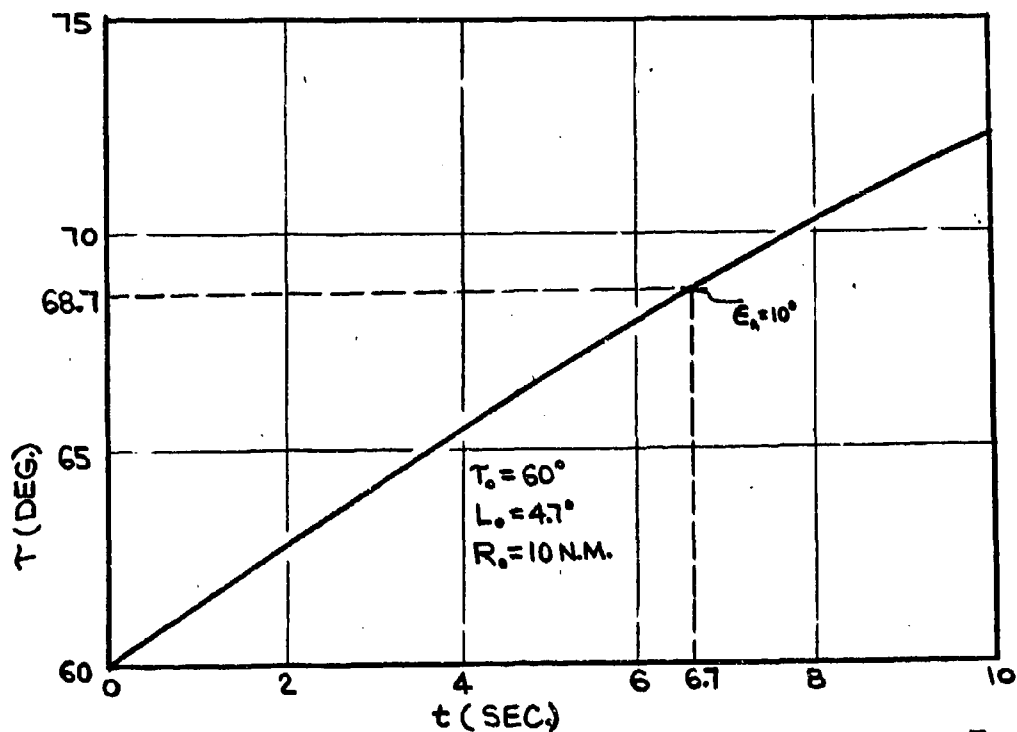


FIGURE 37 : ANGLE-OFF THE NOSE VS. TIME ; $n_z = 5$

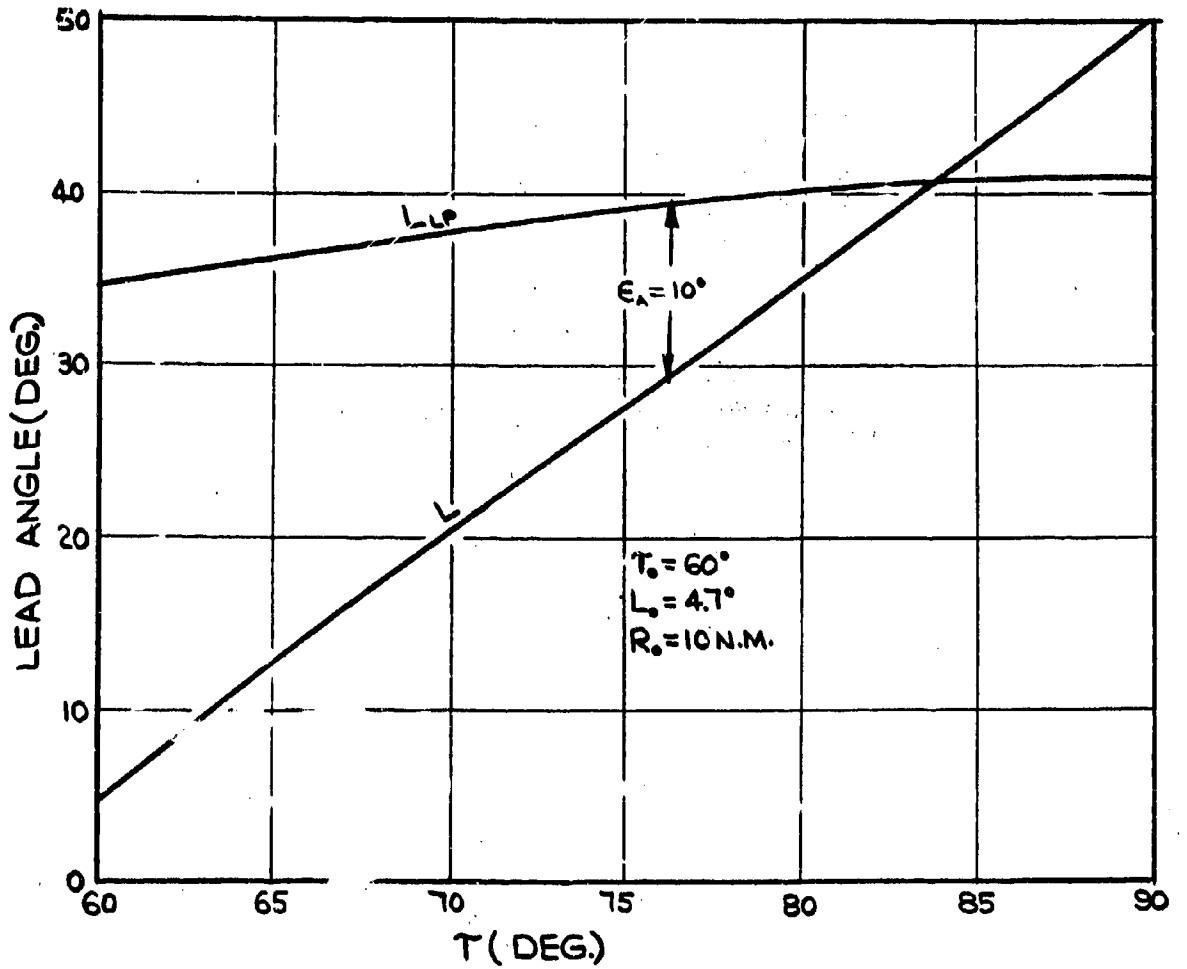


FIGURE 38: LEAD ANGLES VS. ANGLE-OFF THE NOSE ; $n_s = 4$

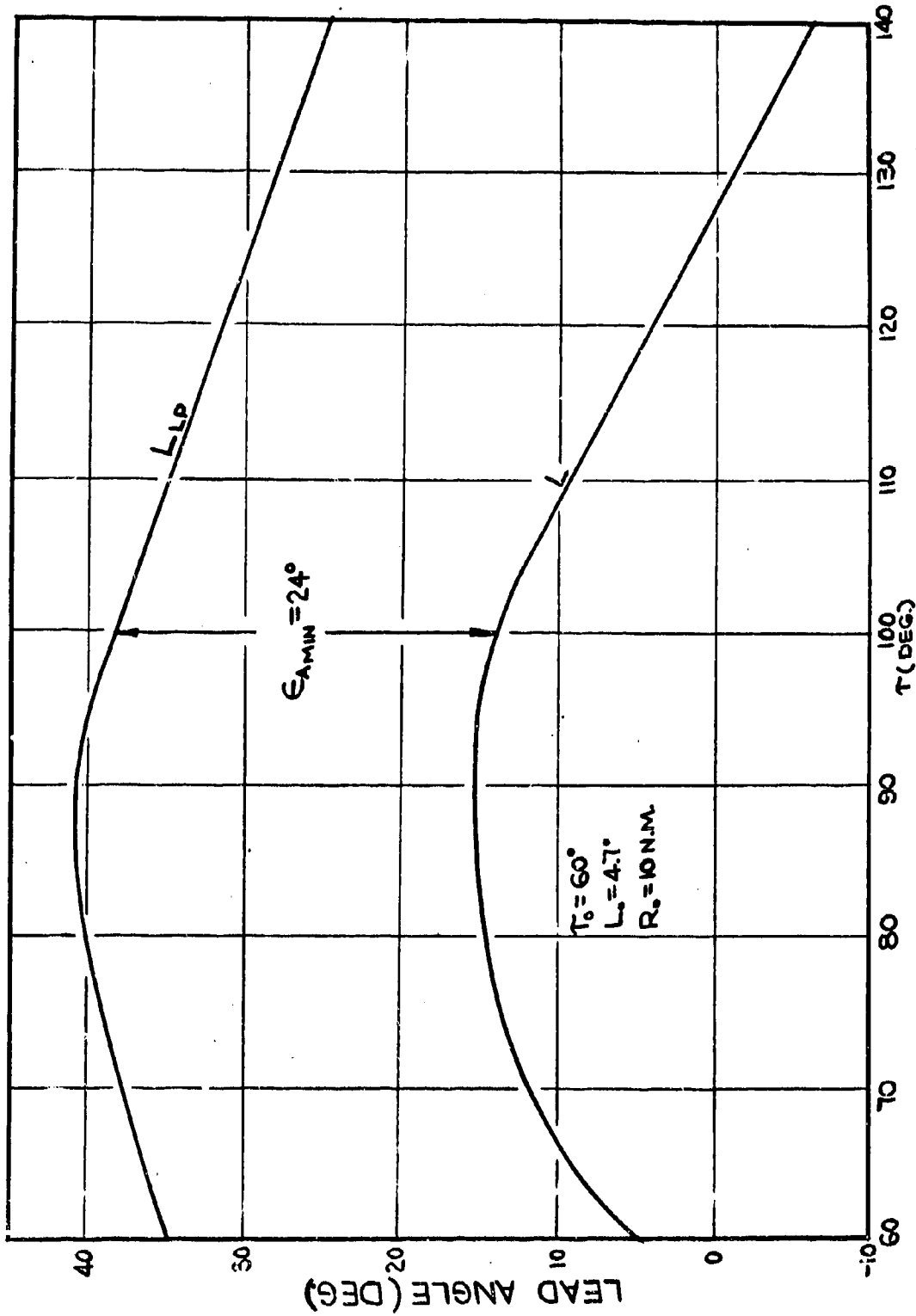


FIGURE 39 : LEAD ANGLES VS. ANGLE-OFF THE NOSE ; $n_z = 3$



APPENDIX IIT - PROBABILITY DISTRIBUTION OF SYSTEM STEERING ERROR AT LOCK-ON

The objective of this phase of the study was to determine the probability distribution of the system steering errors at lock-on when vectored to detection by a collision vectoring system. Converting this probability distribution into a cumulative probability yields design curves from which the expected initial errors versus the cumulative percent cases may be read. These design curves have significance in the design of error circuitry and the choice of system required settling time.

The assumptions made in this phase of the study were:

- (1) The lock-on from the pure collision course occurred at a constant range of 15 nautical miles at all angles, τ , the target's nose.
- (2) The target was flying straight and level.
- (3) Vectoring accuracy assumptions
 - (a) In this study, the interceptor was vectored onto one of four pure collision courses, either $\tau_0 = 20^\circ$, 30° , 40° or 60° ; where τ_0 was the initial angle of the target's nose.
 - (b) Parallel to each of these pure collision courses, we have a standard deviation, σ , of 3 nautical miles.
 - (c) The heading in all the courses comprising the distribution was the heading associated with the course at the center of the distribution.

The percent of interceptions which occur in one nautical mile increments about the pure collision course from 0 to 30 were obtained from a Gaussian distribution. The curve of this distribution function is shown in figure 40.

The headings of the interceptor for the pure collision and lead pursuit courses can be obtained from the following equations:

Pure Collision

$$(1) \quad \sin \lambda_{p.c.} = \frac{V_T}{V_F} \sin \tau_0$$

$$(2) \quad \psi_i = \lambda_{p.c.} + \tau_0$$

CONFIDENTIAL



Lead Pursuit

$$(3) \quad \sin \lambda_{L.P.} = \frac{V_T}{V_F} \left[\frac{1}{1 + \frac{V_T}{V_F}} \right] \sin \tau$$

$$(4) \quad \psi_2 = \lambda_{L.P.} + \tau$$

where $\psi_{1,2}$ are the interceptor headings on pure collision and lead pursuit respectively.

The difference in the heading of the interceptor on the pure collision course at the time of lock-on and the desired lead pursuit heading may be found from equation 5.

$$(5) \quad \epsilon = \psi_2 - \psi_1$$

The conditions used in this phase of the study were as follows:

Altitude of Interceptor - 50,000 ft.

$V_F = V_{F \text{ max}} = 1940 \text{ ft/sec.}$

$V_O = 1291 \text{ ft/sec.}$

$V_T/V_F = 1.0, 0.8, 0.45$

Having now obtained the heading error of the interceptor at lock-on, the cumulative sum of the percent of interceptions which were between 0° and +30° errors were obtained over increments of five degrees of error.

This cumulative sum is shown in figures 41 through 44, where the initial angle off the target's nose, τ_0 , was 20°, 30°, 40° and 60° respectively.

These curves indicate that there is a smaller distribution of errors for the lower speed ratios than for the higher speed ratios. For the cases considered, the percent of interceptions decreased as the angle τ_0 increased.

Since the body of this report was only concerned for the speed ratio of 1.0, the remainder of the discussion on these curves will be for this condition.

For all the cases, except $\tau_0 = 20^\circ$, over 50% of the interceptions had +15° or more error at lock-on. For this exception, 46% had +15° or more error.

The cases of $\tau_0 = 20^\circ$ and 30° had 14% and 18% of the interceptions which had +30° or more at lock-on. For $\tau_0 = 40^\circ$, there was 24% with an error of +30° or more and for the case where $\tau_0 = 60^\circ$, there was 48% of the interceptions with an error of +30° or more at lock-on.

CONFIDENTIAL

CONFIDENTIAL



REFERENCE: NRL Memorandum C-5309-387/57:1mm
Subject: "Classification of Vectoring Errors in Airborne Intercept".
Dated 14 May 1957, Confidential.

CONFIDENTIAL

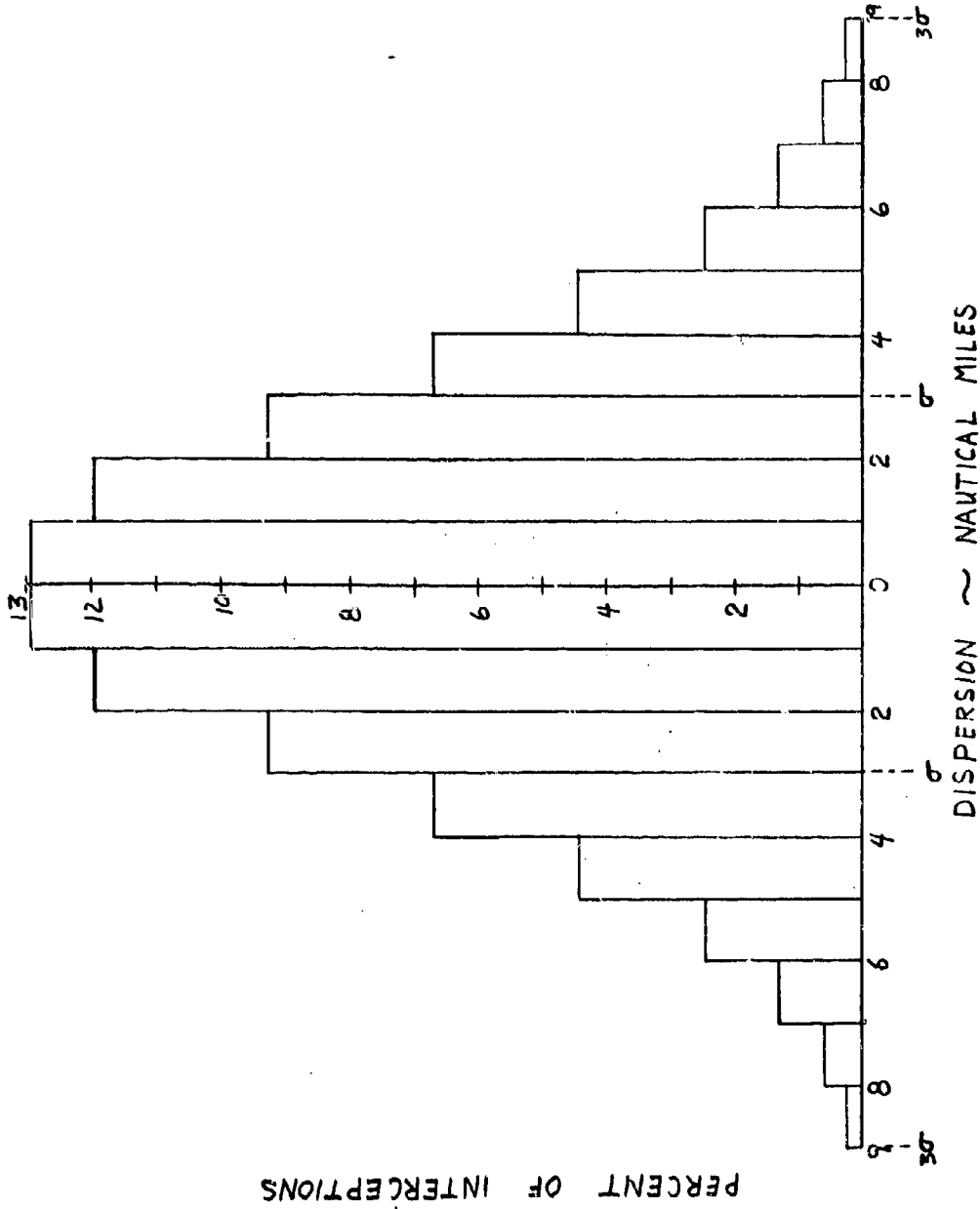
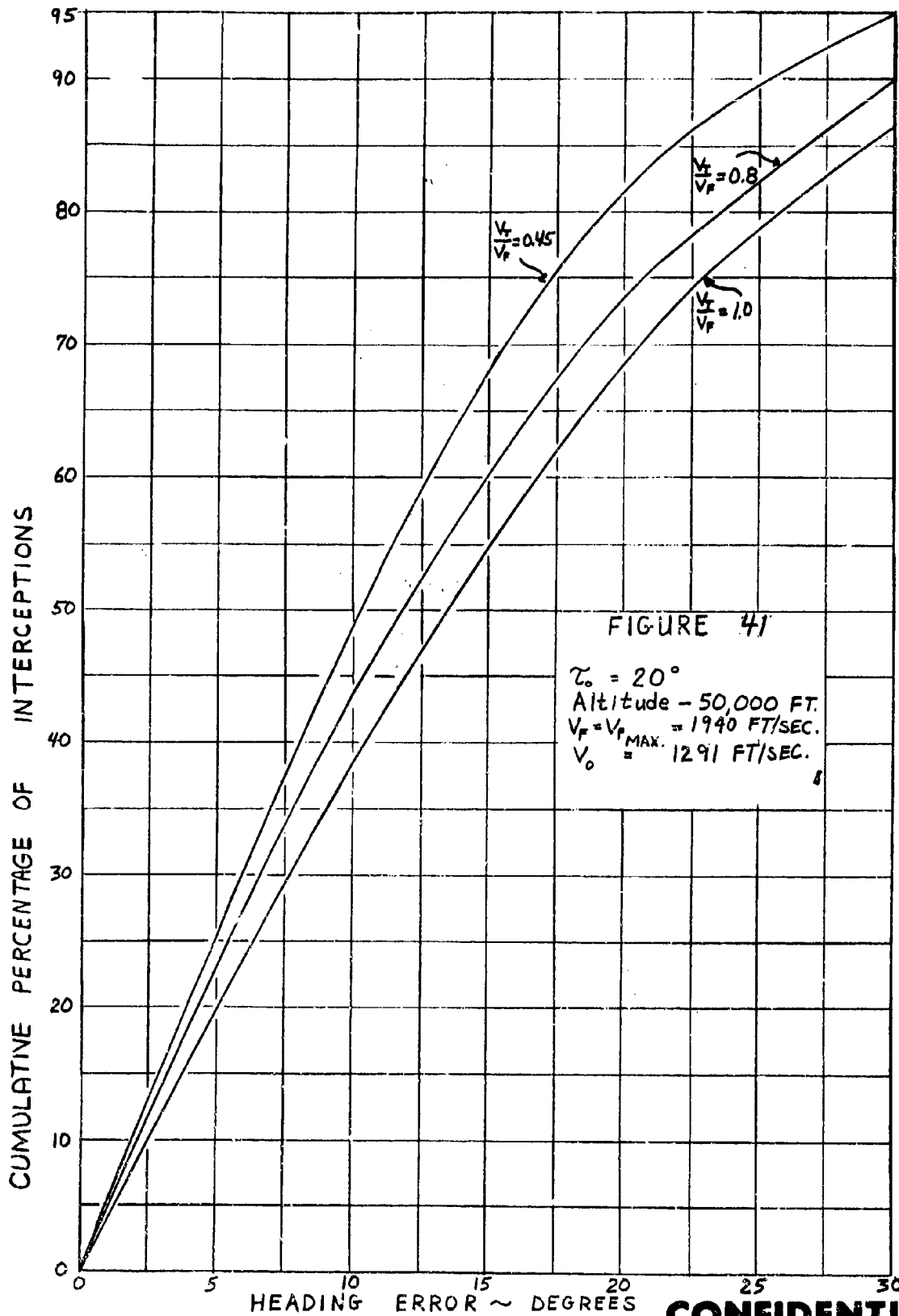


FIGURE 40



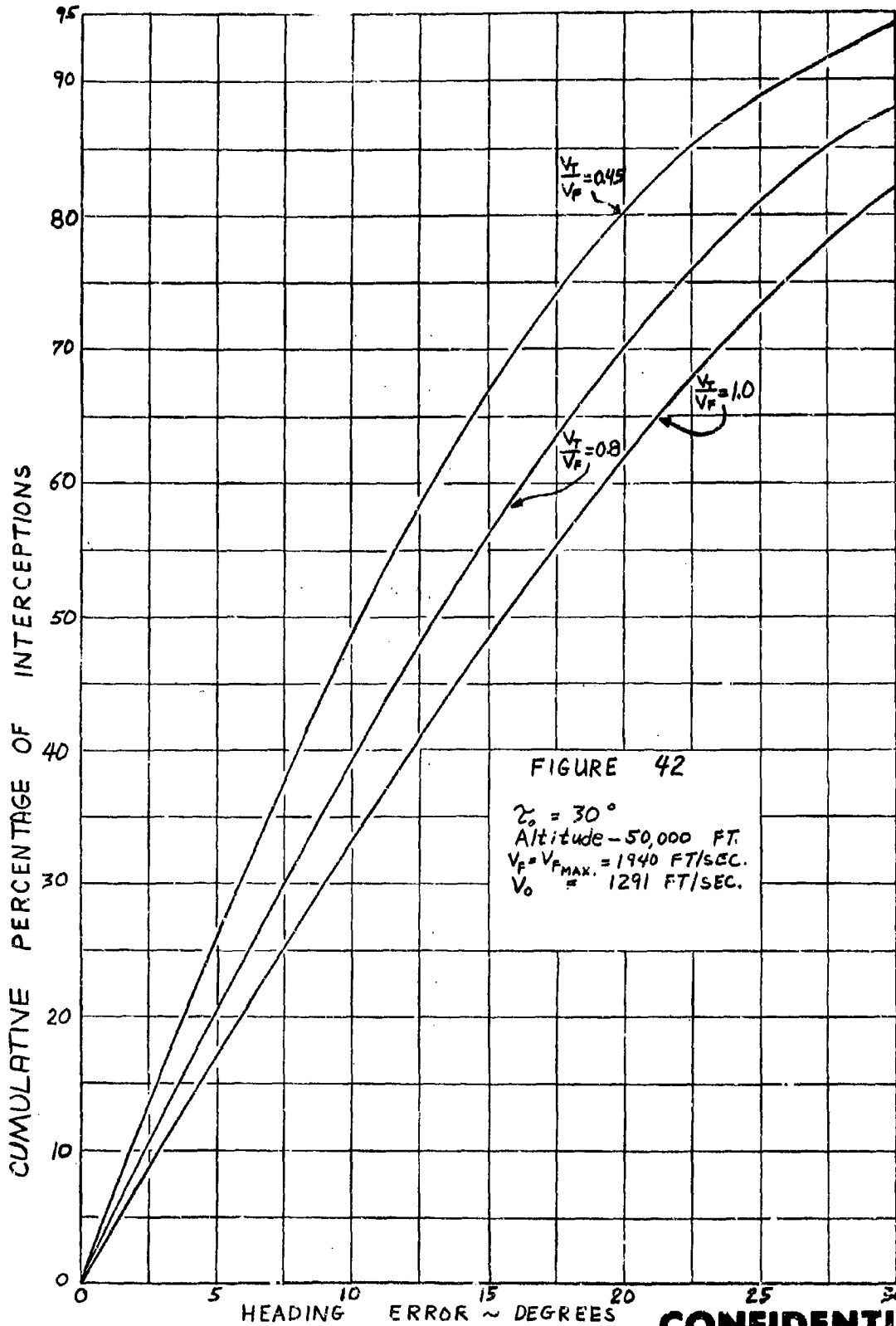


FIGURE 42

$\gamma_0 = 30^\circ$
Altitude - 50,000 FT.
 $V_F = V_{FMAX} = 1940$ FT/SEC.
 $V_0 = 1291$ FT/SEC.

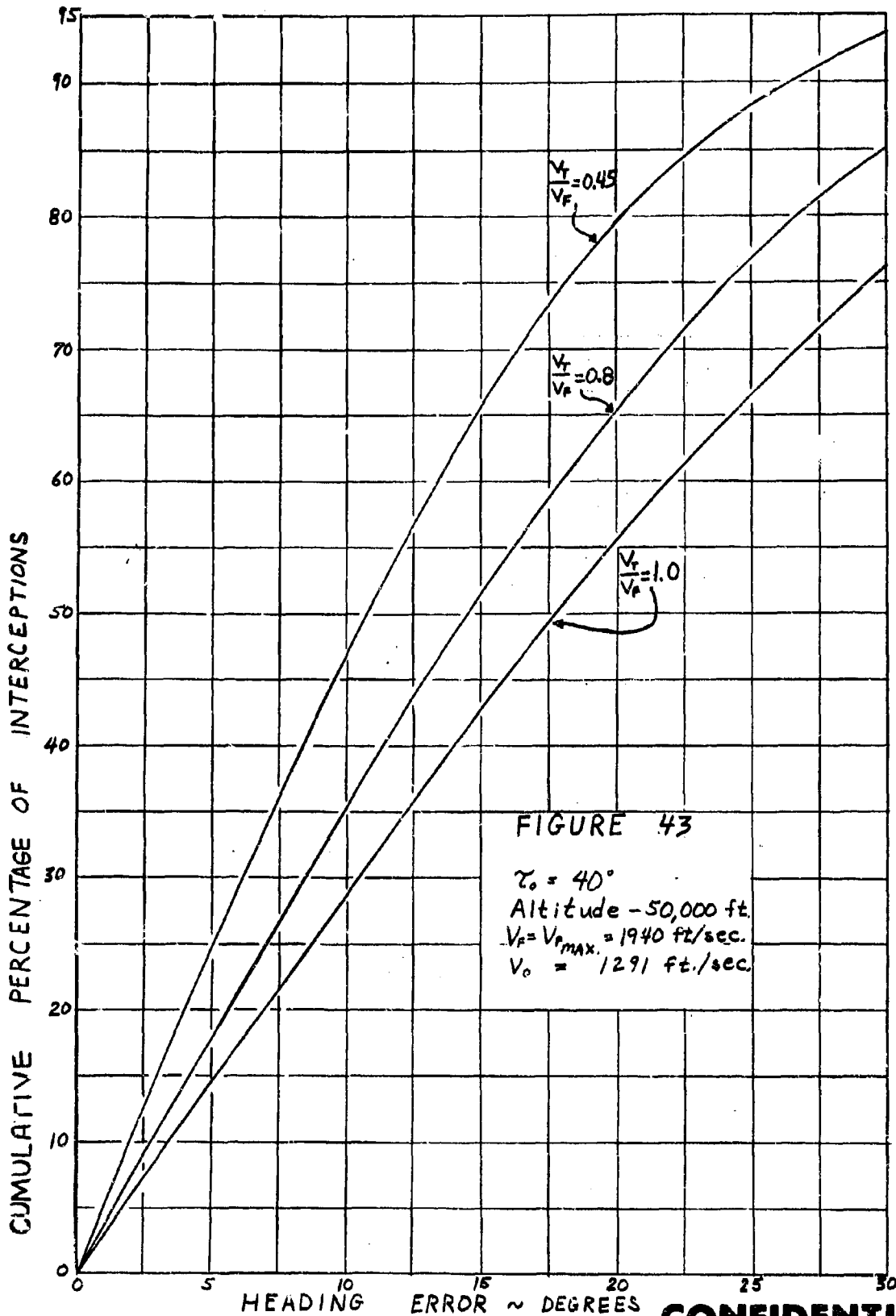
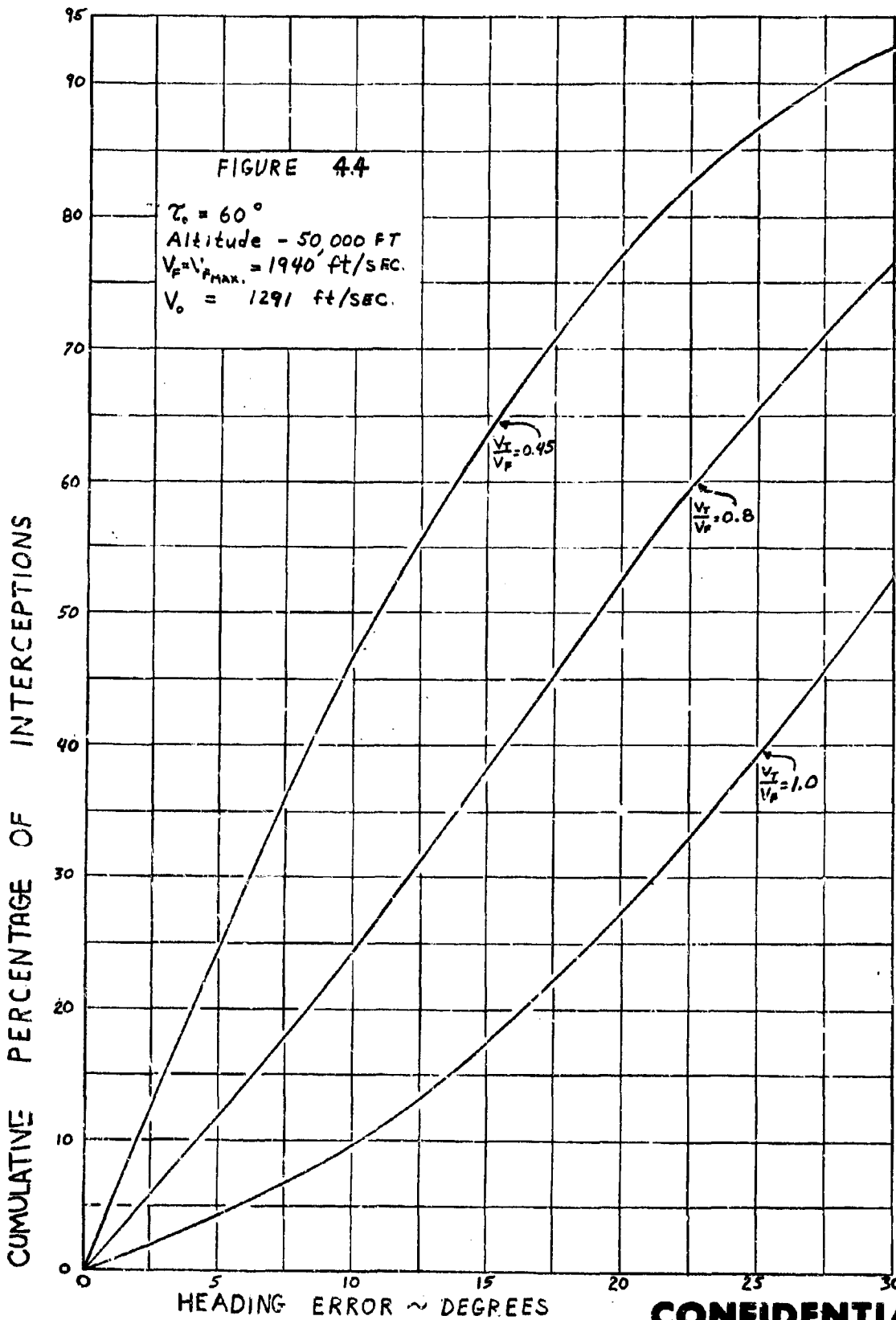


FIGURE 43

$\gamma_0 = 40^\circ$
Altitude - 50,000 ft.
 $V_F = V_{Fmax} = 1940$ ft./sec.
 $V_0 = 1291$ ft./sec.





DEFINITION OF SYMBOLS

- p, q, r - Interceptor angular rates in roll, pitch, and yaw respectively (deg/sec).
- $\delta_e, \delta_a, \delta_r$ - Interceptor elevator, aileron and rudder control surface deflections respectively (deg.).
- α, β - Incremental angles of attack and sideslip, respectively. (deg.).
- $\theta_i, \alpha_o, \lambda_e$ - Initial pitch angle, angle of attack, and elevation lead angle, respectively (deg.).
- ϕ, θ, ψ - Euler angles relating space coordinates to aircraft coordinates in roll, pitch and yaw, respectively (deg.).
- $\dot{x}_T, \dot{y}_T, \dot{z}_T$ - Target linear velocities with respect to space coordinates. (ft./sec.).
- $\dot{R}_x, \dot{R}_y, \dot{R}_z$ - Range rate components in aircraft coordinates. (ft./sec.).
- \dot{R} - Range rate (ft./sec.).
- $\omega_i, \omega_j, \omega_k$ - Roll, elevation and azimuth space rates of the line of sight (deg./sec.).
- Γ_P - Depression angle between armament control axis and aircraft principal axis (deg.).
- λ_a, λ_e - Azimuth and elevation antenna lead angles (deg.).
- $\epsilon_{Ta}, \epsilon_{Te}$ - Azimuth and elevation true errors (deg.).
- $\epsilon_{ai}, \epsilon_{ei}$ - Azimuth and elevation scope errors (deg.).
- V_I - Interceptor velocity (ft./sec.).
- V_T - Target velocity (ft./sec.).
- V_o - Projectile velocity (ft./sec.).
- R - Range to target (feet).
- R_x - Component of range in target direction (n.m.).
- R_y - Component of range perpendicular to target direction (n.m.).
- L - Azimuth lead angle on constant load factor course (deg.).



- L_{LP} - Azimuth lead angle on lead pursuit course (deg.).
- τ_0 - Angle-off the nose (deg.).
- ϵ_{A_0} - Initial azimuth error (deg.).
- g - Gravitational acceleration (ft/sec.²).
- n_z - Incremental normal acceleration (g's).
- $\dot{\psi}$ - Interceptor yaw rate (deg./sec.).
- τ_s - The prescribed length of time for which the radial error must be on or below a specified value. (sec.).
- N_{AZ}, N_{EL} - Shaped noise in azimuth and elevation channels, respectively.
- (₀) - Subscript denoting initial condition.
- (^o) - Superscript denoting differentiation with respect to time.
- t - Time (sec.).

$l_{sa}, l_p, l_v, l_{sr}, l_r$
 m_{sc}, m_w, m_f
 n_{sa}, n_{sr}, n_v, n_r
 z_{sc}, z_w, z_f
 y_{sr}, y_v, y_r, y_r

Interceptor aerodynamic constants obtained from aircraft manufacture's data.

- Median settling time - The time required to reduce the initial error on 50% of the runs to or below a specified value for a prescribed length of time.
- 85% settling time - The time required to reduce the initial error on 85% of the runs to or below a specified value for a prescribed length of time.

CONFIDENTIAL



Analytical Section Technical Memorandum No. 176

APPENDIX VII

**AN/AFQ-72 Improvements In Fair
Weather Environment**

Distribution

016 - G. E. McClellan
100 - D. J. Povejsil
103 - R. G. Clanton
103 - F. J. Riddleston
103 - S. Baida (20)
083 - A. A. Hiza
083 - J. G. Kolman
085 - Y. Cim

S. Baida

5-7-57/db

CONFIDENTIAL

CONFIDENTIAL



Abstract

This memo evaluates the effect of the currently proposed improvements on the fair weather detection range performance of the AN/APQ-72 radar.

CONFIDENTIAL



I. Introduction

Of the currently proposed improvements, the following are evaluated in terms of their effect on the detection range capability of the AN/APQ-72:

1. Triangle vectoring
2. Search Volume Optimization
3. Automatic Alarm
4. Improved Receiver Noise Figure
5. Bandwidth Switching
6. Bright Display

The improvements relating to ECM, clutter and foul weather will be treated separately in subsequent reports.

II. Triangle Vectoring

Triangle vectoring is intended to replace the presently used voice control. It will provide the pilot with sufficient information to analyze the tactical situation and act accordingly. The attack course will be entirely of the pilot's choosing. The proponents of triangle vectoring maintain that the pilot is in a better position to decide on an attack course.

Target information will be transmitted by digital means to the fighter's computer every two seconds. The computer will also receive continuous information pertaining to the fighter's motion. The inputs to the computer are:

- | | |
|--|---|
| 1. Relative displacement between the fighter and the target in rectangular coordinates | } Transmitted to the fighter every two seconds. |
| 2. Target speed | |
| 3. Target bearing | |
| 4. Wind velocity | } Determined by the fighter and continuously fed to the computer. |
| 5. Fighter speed | |
| 6. Fighter bearing | |

The search radars that will determine target information will be either shipborne or airborne. Table I lists some search radars that will be available in the 1960-1965 era.

Table I .. Search Radars

Type and Designation	Frequency	Range (N.M)	Scan Rate (rpm)	Power (watts)
Unstabilized				
SFS-12	L	80	1.5-2.5	
SFS-17	L	70	0-12	
Stabilized				
SFS-3	S	45	1, 2, 3, 5, 10	
SFS-13	S	180	3, 6	
SFS-26	S	120	10, 15	



Table I - Search Radars (Cont'd)

Type and Designation	Frequency	Range (N.M.)	Scan Rate (rpm)	Power (watts)
Stabilized BFS-3	-	40	0.8	
EW SPS-17	200 or 400 mops	200	10	750 kw
Airborne APS-20E	S	200	6-10	2.25 mw
APS-70	425 mops	250	-	2 mw
APS-45	X	-	-	450 kw

In the computer, both the fighter and target velocity vectors will be derived. Range to the target and the designated relative position of the target with respect to the fighter will be computed. The lead angle will also be computed and the antenna driven such that it is pointing at the target. The target designation point will be determined and presented to the pilot.

All presentation to the pilot will be made on the B-Scope. Here the fighter position will always be on the bottom of the scope (zero range) and in the center of the azimuth indication (zero azimuth angle). The pilot then will feed an arbitrary time-to-go setting into the computer. The scope presentation will then show both the fighter and target velocity vectors for the particular time-to-go setting. This is shown in Figure 1.

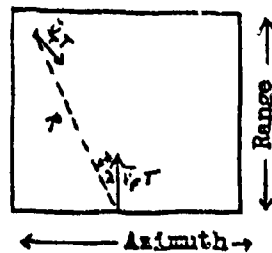


Figure 1

By adjusting the time-to-go setting, the velocity vectors will assume different lengths. The tactical situation is thus presented to the pilot to evaluate. Target bearing, the speed ratio, lead angle, angle off the target's tail and range are displayed or easily determined.

If the pilot wants to fly a collision course, then he maneuvers the fighter such that the two VT vectors intersect as shown in Figure 2.

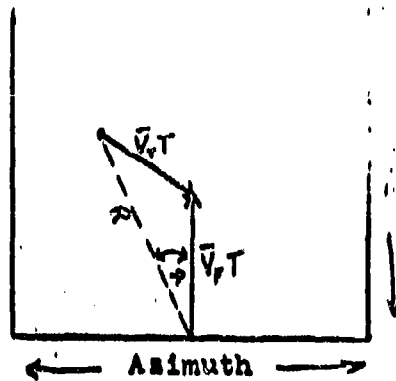


Figure 2

After the time-to-go setting is initially made, a time clock will run time-to-go down. The antenna is automatically pointed at the target.

Triangle vectoring can be applied to any desired course or tactic. If for example the fighter is approaching the target nose-on, but an anti-parallel course is desired, then the display will be altered to accommodate the developing geometry. This is shown in Figure 3.

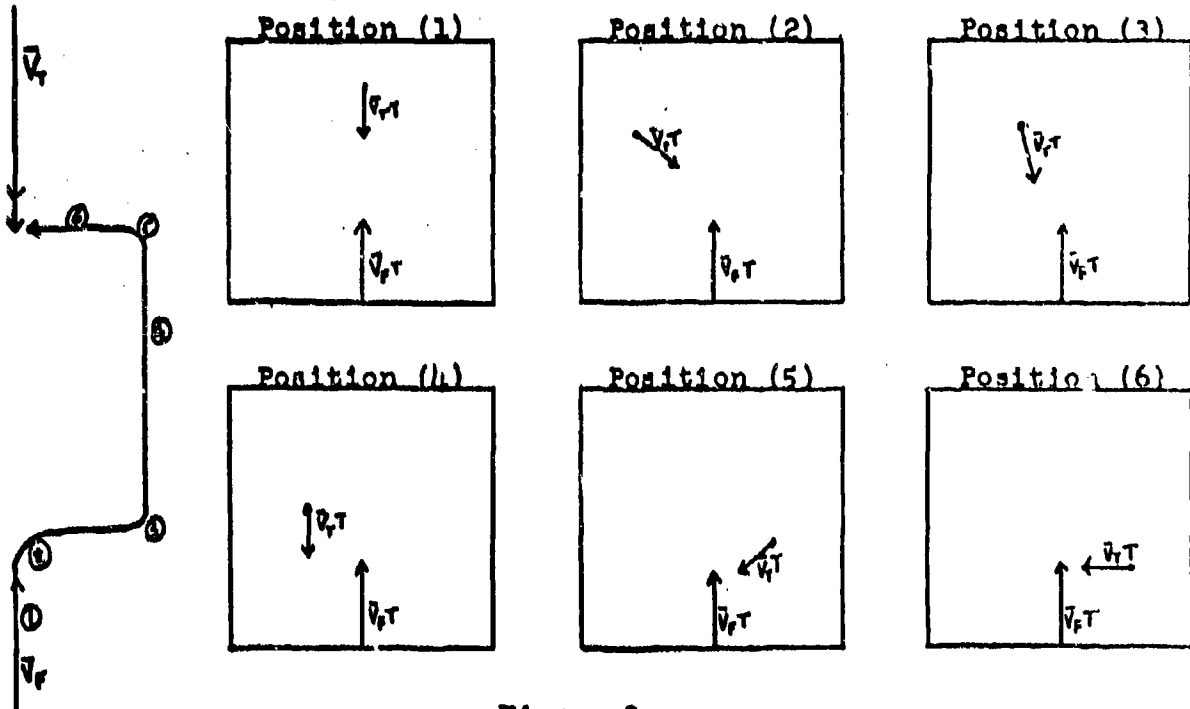


Figure 3



The accuracy with which triangle vectoring can establish the relative position of the target is 2 n.m. radius (rms) in azimuth and 1 n.m. radius (rms) in elevation. Estimates on the accuracy with which the target bearing angle can be determined vary from ± 10 degrees to ± 20 degrees. Significant improvements in AI detection and lock-on range can be made with the proper use of triangle vectoring because the search volume can be shortened with the result that either the number of hits / scan can be increased or the frame time decreased or both.

It is planned that flight tests conducted by NRL will start July 1, 1957. Data taking is to commence on September 1, 1957. It is hoped that the test program of triangle vectoring will be completed by June 1, 1958. The primary objection of the flight test program is to determine the accuracy of the system. It is estimated by NRL that due to lead time factors, triangle vectoring will not be available for the XIA system. Existing vectoring techniques must be used. The vectoring accuracy will still be the same as for triangle vectoring. Hence detection range improvement through optimization of the search area is still possible.

III. Search Area Optimization

The probability of detecting a target is the product of two probabilities.

1. The probability that a target is within the area scanned.
2. The probability distribution given that the target is within the scanned area.

To optimize the search area, the area scanned should include "much" of the area of uncertainty of target location. The ultimate criterion of an optimized search area is the detection range attainable with the particular scan pattern chosen. Vectoring inaccuracies will produce an area of uncertainty of 2 n.m. radius (rms) in azimuth and 1 n.m. radius (rms) in elevation. Since targets are assumed to be normally distributed about the designated target position, a search area of $12 \text{ n.m.} \times 6 \text{ n.m.}$ would provide 99% probability of a target lying within the area searched. If R is the detection range, then the angular area that should be scanned is $\frac{12 \times 57.3}{R} \times \frac{6 \times 57.3}{R} \text{ deg}^2$

Such a search area is not necessarily an optimum one. An estimate of target range will be available from vectoring information. Ideally, the area scanned should vary continuously with target range, but an alternative can be discrete changes in the area searched to be made either manually or automatically as the designated target range changes.

Detection range improvement as a result of a reduction in the area scanned arises from a reduction in the frame time or an increase in hits per scan or both. The improvement due to a reduction in frame time can be seen from figure 4 which shows the relationship between R/R_0 and $\Delta R/R_0$

where: R_0 = Idealized range
 R = Detection range for 85% and 50% cumulative probability of detection
 $\Delta R = R t_f$ \dot{R} = Closing rate
 t_f = Frame time



Figure 4 is derived for slowly scintillating target signals and an operator factor of 0.5.

Improvement in detection range as a result of an increase in hits per scan can be seen from figure 5 which shows R/R_0 as a function of hits per scan for various values of n (total number of noise variants in a false alarm time). Figure 4 is derived in reference 1. This relationship between R/R_0 and hits per scan was derived for constant amplitude target signals. If scintillation of target echoes is taken into account, then the detection range improvement that would result from increasing the hits per scan from n_1 to n_2 would be approximately

$$\left(\frac{n_2}{n_1}\right)^{0.115}$$

Optimization of the search area must consider both the probability of a target lying within the area searched and the probability distribution for a target within the area searched. For the XIA system, the most important case is the nose-on, high speed attack. It will be assumed that $R_0 = 40$ n.m. is attainable. This figure for R_0 can be justified and will be developed later. The closing rate is assumed as 0.6 n.m./sec. The optimum detection ranges for various search areas for these conditions are shown in figure 6a. This figure was derived by extrapolating AFQ-64 flight test results (reference 2) by the methods of reference 3. The optimum detection range for a given search area is the detection range optimized with respect to frame time.

For a given detection range, there exists an optimum search area. This is evident from figure 6a. Search areas greater than the optimum results in either an increase in frame time or a decrease in hits per scan or both. On the other hand, a reduction of the search area from the optimum will decrease the probability of a target lying within the area searched. No one particular search area is optimum for all detection ranges. A truly optimum search pattern is one that varies with target range. A compromise between system detection requirements and mechanization considerations can be made by considering that tactically 20-30 miles of detection range is needed. Hence a search pattern that covers 17 degrees by 8.5 degrees at long range and one that covers 23.6 degrees by 11.8 degrees (3 bar scan) at ranges below 24-26 miles will provide maximum probability of detection for the tactically required detection ranges. The cumulative probability of detection curves for this situation are shown as curves A and B of figure 6a. As additional information, the case where the vectoring accuracy is 3 n.m. (rms) in radius by 1 n.m. (rms) in radius is shown in figure 6b. Here curves A and B of figure 6a are degraded by the additional vectoring inaccuracy.

It has been assumed thus far that fighter bearing is known exactly and that the bearing inaccuracies lie entirely with the target. If this be the case, then the curves of figure 6a are valid. This is the exceptional case. If the bearing inaccuracies are divided between the fighter and the target, then the fighter's bearing inaccuracy must be included in the search pattern. From considerations of vectoring accuracies, it appears that 10 degrees need be added to the azimuth coverage. Under this condition, curves A and B of figure 6a would be altered to those as shown in figure 6c.



Effect of Frame Time
On
Detection Range

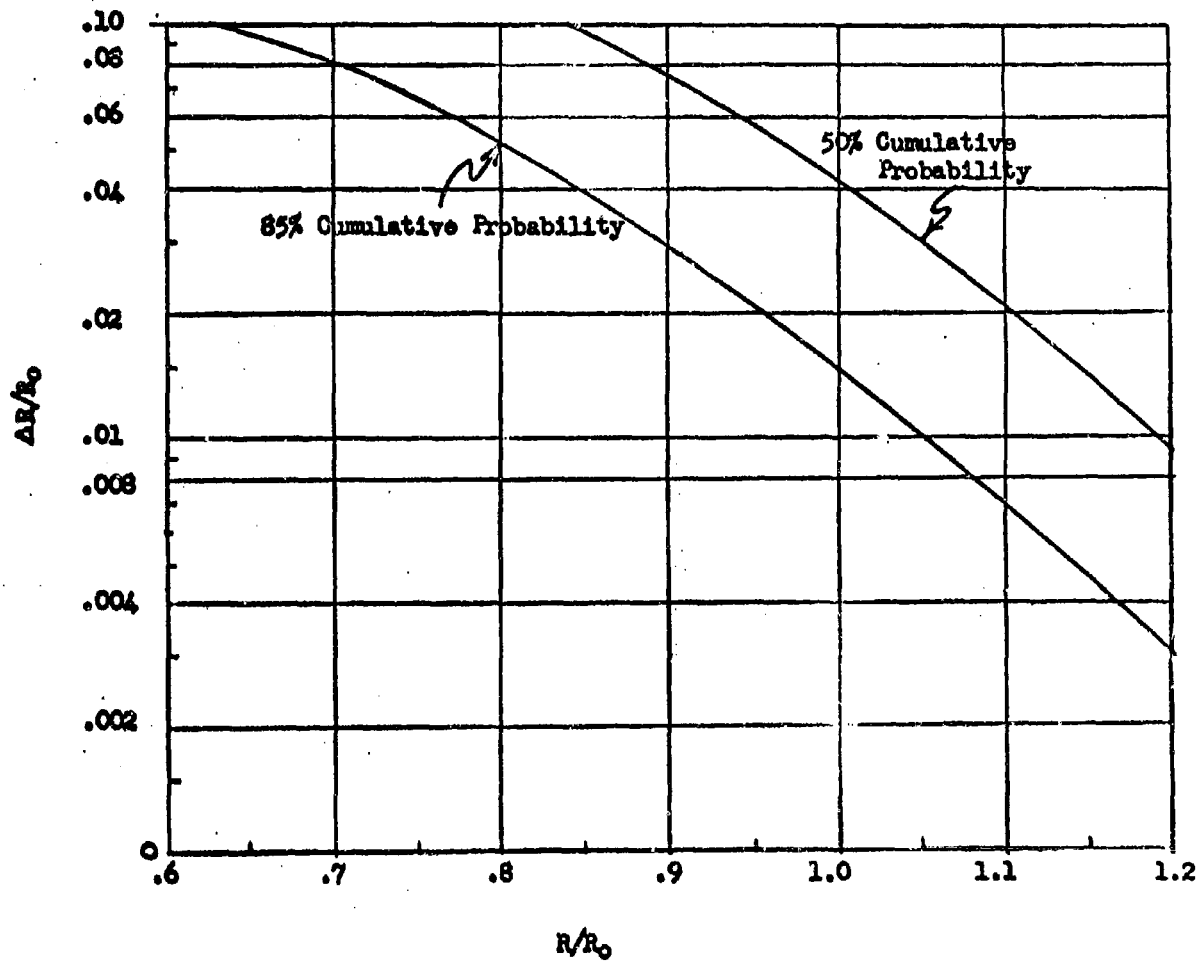


Fig. 4



**Effect of Hits/Scan
On
Detection Range
(90% Probability/Scan)**

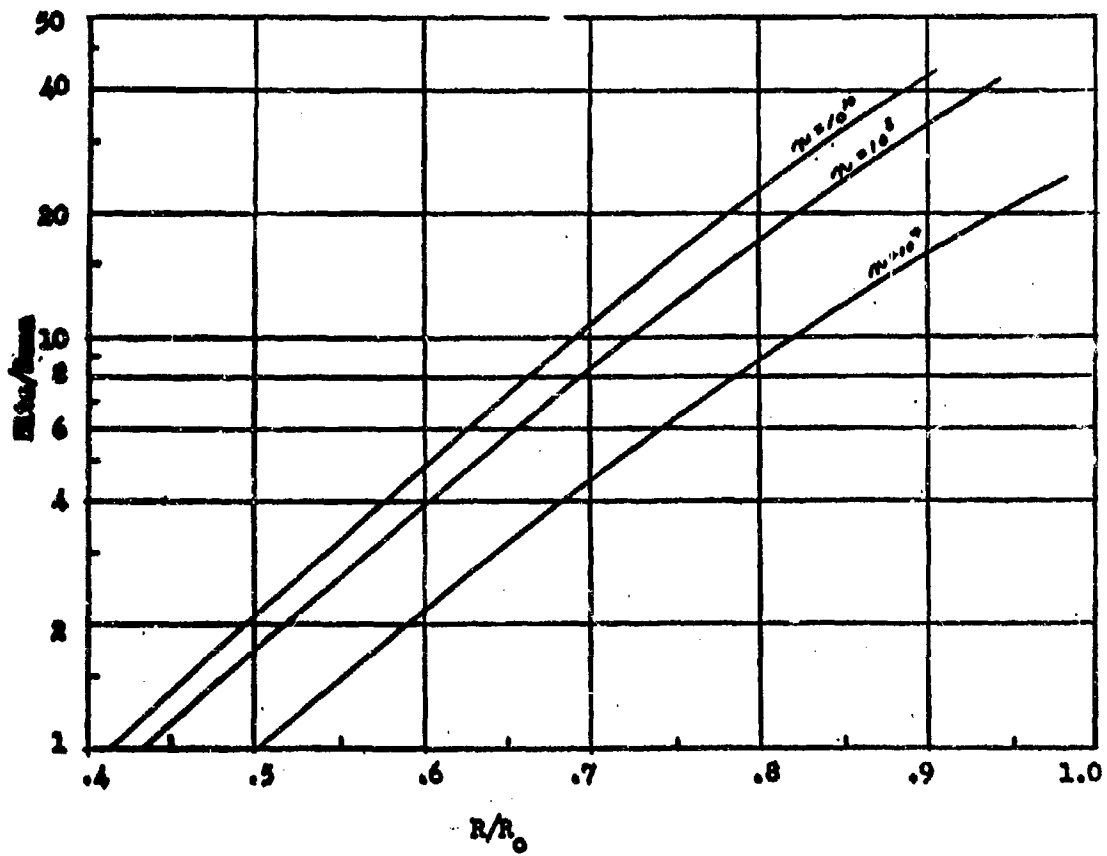


Fig. 5

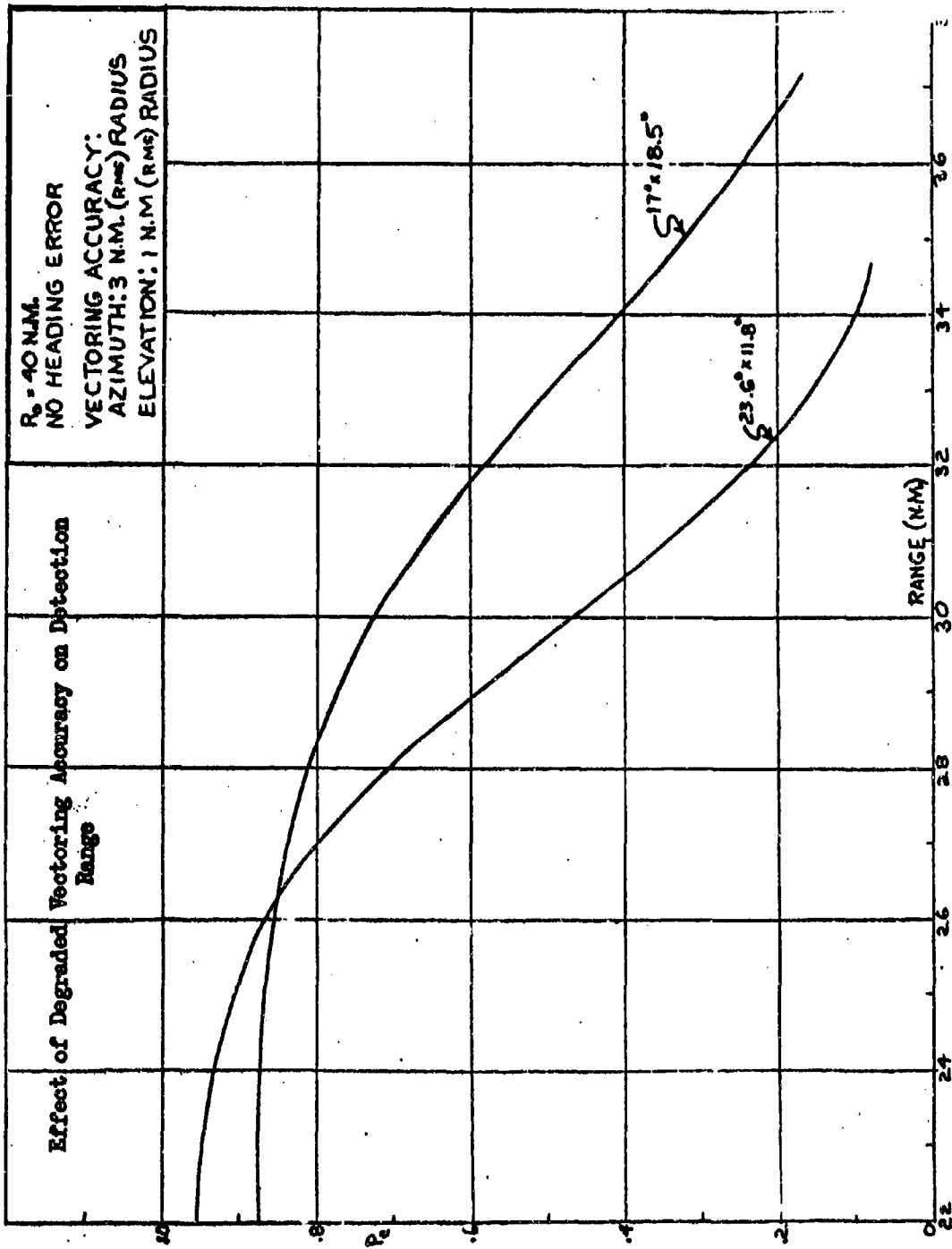


FIGURE 6b

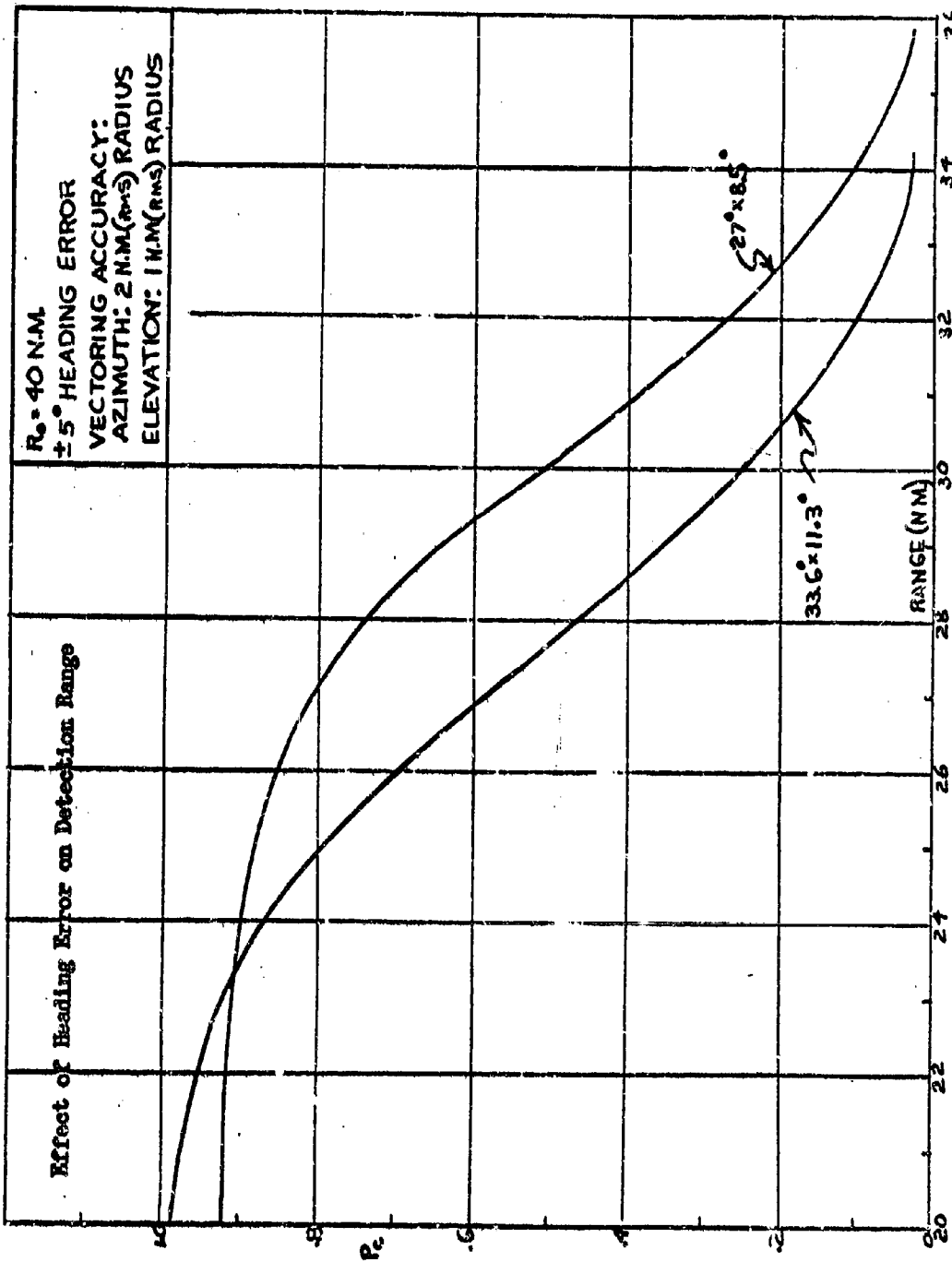


FIGURE 6C



For smaller R_0 e.g. $R_0 = 30$ n.m., the search pattern must be enlarged. Figure 7a shows detection ranges as a function of search area assuming no heading errors and a vectoring accuracy of 2 n.m. (rms) in radius in azimuth and 1 n.m. (rms) in radius in elevation. When 10 degrees of heading error are included, the curves of figure 7b results. From figure 7b it can be concluded that for smaller R_0 , a switch from $33.6^\circ \times 11.8^\circ$ to $40.2^\circ \times 15.1^\circ$ should occur at 16 n.m.

The area searched as a function of target range is tabulated below. The tabulation represents the optimum switching in search area that should occur in order to achieve maximum probability of detection for all ranges. Mechanization difficulties might rule out some switching. Hence the search area switching tabulated below cannot be recommended until mechanization considerations are investigated.

Range	Area Searched
Greater than 26 n.m.	$27^\circ \times 8.5^\circ$
16 - 26 n.m.	$33.6^\circ \times 11.8^\circ$
Less than 16 n.m.	$40.2^\circ \times 15.1^\circ$

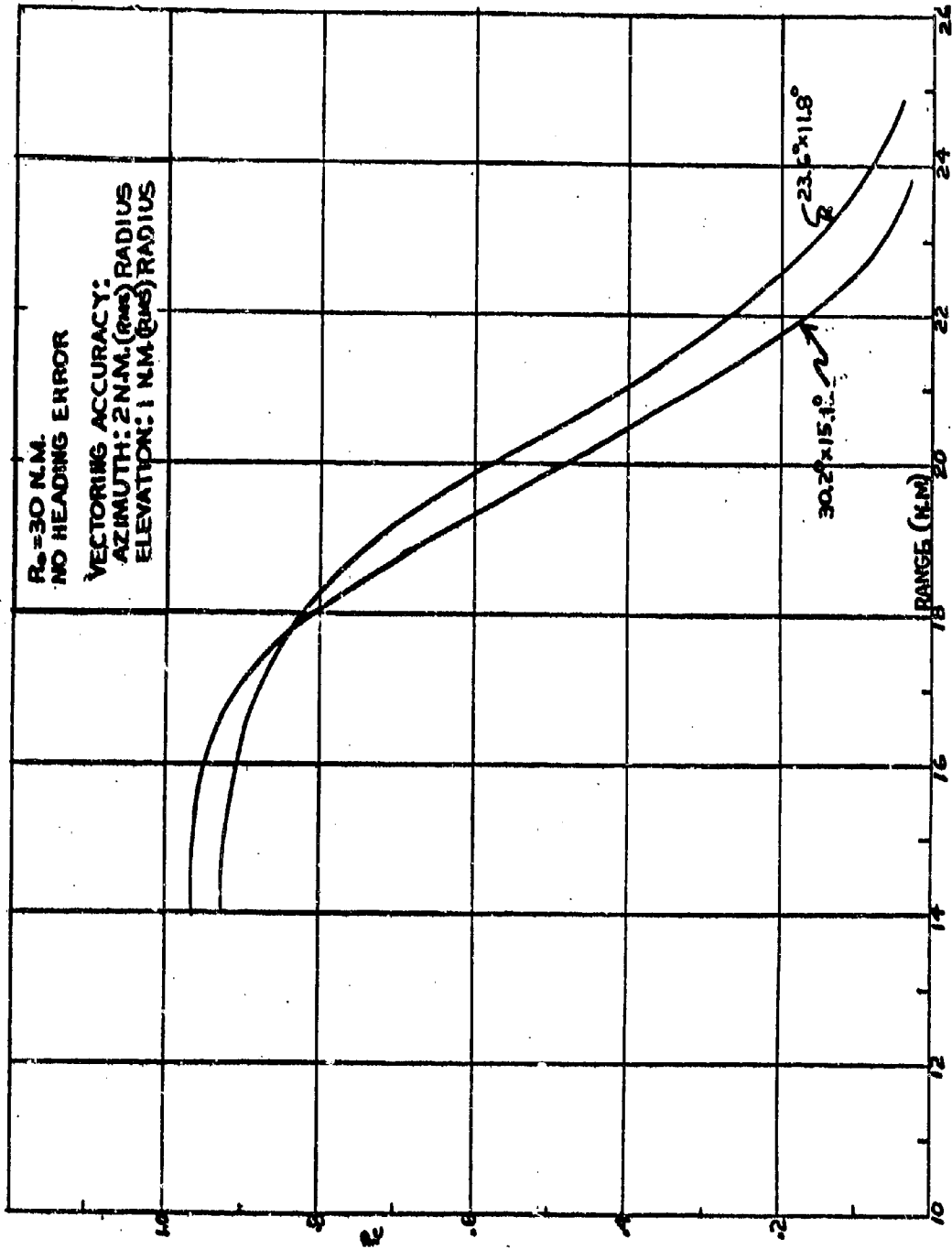


FIGURE 7a

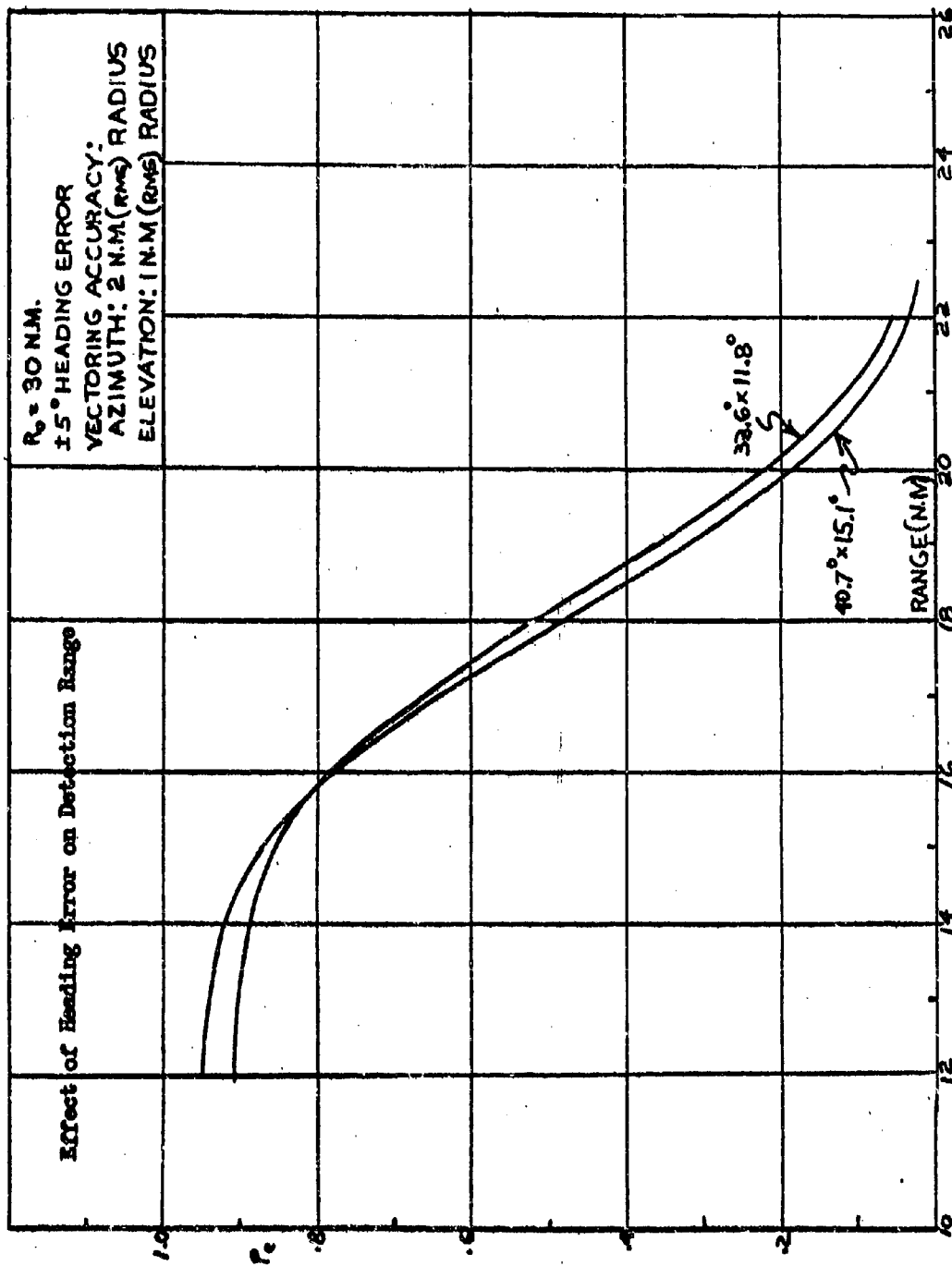


FIGURE 7b



IV. Automatic Alarm

The purposes of automatic alarm circuitry are to:

1. Increase the detection range by negating the deleterious effects of "operator factor".
2. Permit the pilot to concentrate on flying his aircraft.

The proposed automatic alarm system will activate an alarm when the system detects a target. "Operator Factor" degrades the detection range by virtue of the following factors.

1. The operator cannot concentrate on the detection problem.
2. The operator must encompass a large field of view for primary detection.
3. The detection time of the operator must include 1-2 additional frame times for target verification purposes.
4. Operator fatigue.

The proposed automatic alarm circuit for the AFQ-72 is shown in figure 8. The circuit is basically a two-step threshold detector. Delay line cancellation discriminates against large clutter signals. The primary detector responds to any single pulse whose amplitude exceeds a given threshold setting. The second detector responds only when the summation of the succeeding four pulses exceeds a second threshold setting. The false alarm time for the primary detector is 0.1 seconds. For the second detector, the false alarm time is 1800 seconds.

The video signals are applied to a two stage video amplifier. An AGC loop controlled by noise regulates the gain of the video amplifiers. This is necessary since the primary detector threshold is set at some level above the average noise. This level will be determined later.

The output of the second video amplifier is fed to an inverse log amplifier whose function is to make homogeneous clutter signals have a constant amplitude and well defined leading and lagging edges. (Homogeneous clutter is defined as clutter that is composite in the sense that the echo amplitude is the vector sum of many small echoes from individual targets scattered over an area determined by the beam-width and pulswidth. The individual echoes are so numerous in the illuminated area that even the largest is small compared to their sum and the phases of these echoes are independent). The inverse log amplifier is a high gain amplifier whose characteristics are such that the greater the amplitude of the input signal, the greater the gain of the amplifier, thus sharpening the edges of the clutter signal.

The output of the inverse log amplifier is then coupled into a limiter circuit which limits the input signal (to a clutter rejection circuit) to a constant amplitude. The clutter rejection circuit is a pulswidth discriminator. It consists of a delay line differentiator, a delay line and a summing amplifier. The pulswidth discriminator produces positive and negative pulses of equal amplitude and width. The pulswidths cannot exceed the delay time of the delay line discriminator. Consequently, pulswidths in excess of the delay time of the differentiator are cancelled out by reflections along the line and results in a dead zone between the positive and negative pulses. See figures 9 and 10.

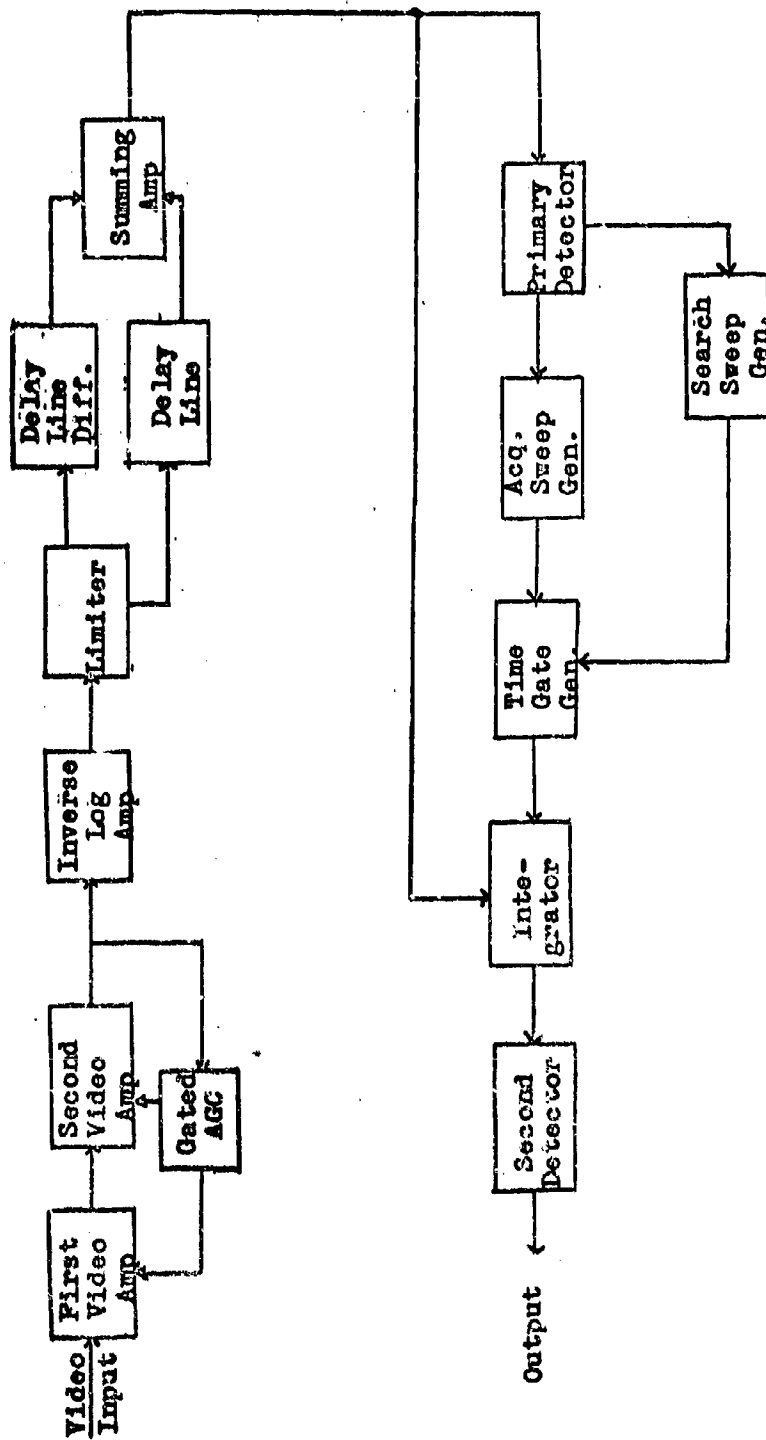
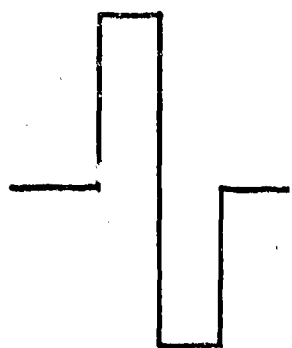
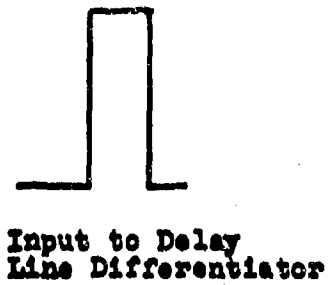
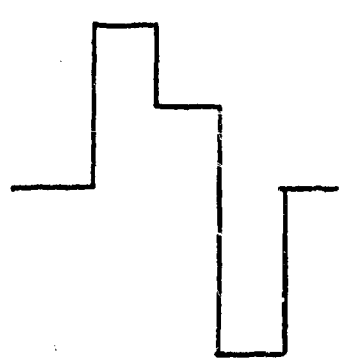
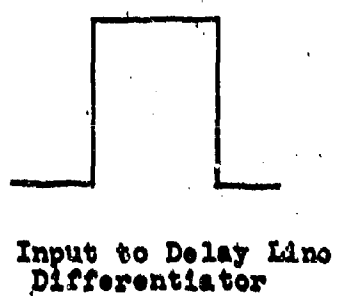


Figure 8



Signal Width Equal to Delay Time of Differentiator.

Figure 9

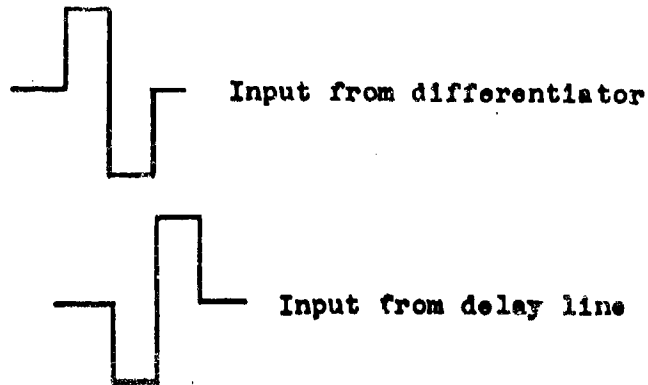


Signal Width Equal to Twice the Delay Time of Differentiator

Figure 10

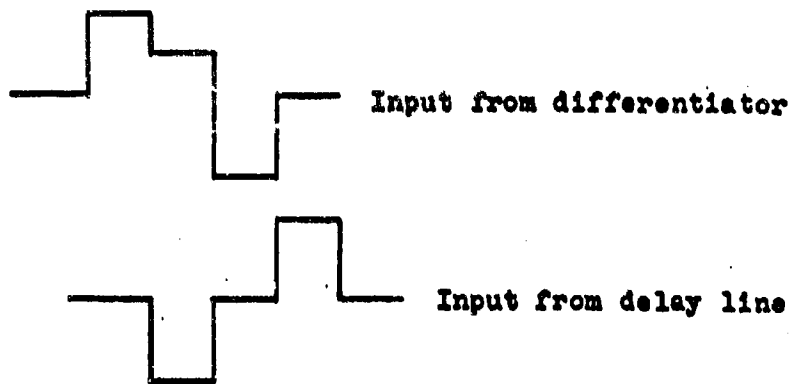


The output of the differentiator is sent to an input to a summing amplifier and into a delay line. The output of the delay line is sent to another input of the summing amplifier. The summing amplifier will develop an output if the signals to it from the differentiator and the delay line are in time coincidence and 180 degrees out of phase. Refer to figures 11 and 12.



Inputs to summing amplifier when signal width equals delay time of differentiator.

Figure 11

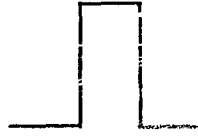


Inputs to summing amplifier when signal width exceeds twice delay time of differentiator.

Figure 12



Input to Delay Line Differentiator



Output of summing Amp.

Signal Width Slightly less Than Delay Time of Differentiator

Figure 13

For signal widths greater than the delay time of the differentiator, the dead zone between the positive and negative pulses increases, causing these pulses to move out of time coincidence resulting in a reduced width out of the summing amplifier. For signal widths greater than twice the delay time of the differentiator, there is no output of the summing amplifier. (Figure 13.)



Input to Delay Line Differentiator



Output of Summing Amp.

Signal Width Greater Than Twice The Delay Time of the Differentiator

The pulsewidth discriminator output is sent to an integrator and the primary detector. The primary detector generates a range gate. Pulses within the range gate are integrated for a number of repetition rates. If the integrated energy exceeds the threshold level of the second detector, an alarm is given.

Upon reception of the triggering signal, the search sweep's integrator starts integrating. The output increases until a suspected target signal triggers the primary detector. The primary detector holds the output of the search sweep at the level it had when the suspected target signal triggered the primary detector. The primary detector output initiates the acquisition sweep.

The acquisition sweep builds up a voltage with the aid of the reference voltage and the held output of the search sweep generates a range gate. After the first gate has been generated, the acquisition sweep holds this reference. The search sweep returns to zero, but the acquisition sweep holds its level. The search sweep now returns to sweeping. A gate is generated over the target whenever the sum of the search sweep output and the held acquisition sweep output cause the comparator to go into conduction. This will occur when the search sweep output is at target range. This will continue until a timing circuit which is triggered by the primary detector returns the circuit to its initial conditions.

For the APQ-72, the number of pulses in a pulse packet is (for no lobing of the antenna):

$$N^1 = \frac{Bfr}{W}$$

B = Beamwidth (half-power)
fr = PRF
W = Azimuth antenna rate

$$N^1 = \frac{3.67 \times 550}{100} \approx 20 \text{ pulses}$$

Lobing will reduce the effective number of pulses in the pulse packet to approximately 7.

Since the false alarm rate for the primary detector is 10 per second, the number of chances of getting a false alarm for the first threshold is

$$n = T_{fa} \cdot p$$

T_{fa} = false alarm time = 0.1 sec
fr = PRF = 550 pulses / sec
p = number of gates in a sweep.
p = 700 for a 100 mile sweep.

$$n = 3.85 \times 10^4$$

The probability of exceeding the first threshold can be determined from reference 1. Since the primary detector is a peak detector, the pertinent parameters in determining the probability of exceeding the first threshold are:

$$\begin{aligned} n &= 3.85 \times 10^4 \\ N &= 1 \\ \gamma &= 7 \end{aligned}$$

Let P_a be this probability for a given S/N.

After the first threshold has been exceeded, the next four pulses are integrated. If the resultant integration exceeds the second threshold, an alarm is given. For the second detector,

$$\begin{aligned} n &= T_{fa} \cdot fr \cdot p \\ &= 1800 \times 550 \times 1 = .99 \times 10^6 \end{aligned}$$

From Reference 1, the probability that K integrated pulses will exceed the second threshold (=P_{bk}) is determined. The pertinent parameters are:

$$\begin{aligned} n &= .99 \times 10^6 \\ \gamma &= N = K \end{aligned}$$



P_a and P_{bk} having been determined as a function of S/N , the joint probability of an alarm as a function of S/N is determined. The ways in which an alarm is given are.

1. The first pulse of the pulse packet can exceed the first threshold. That probability is P_a . The next four integrated pulses can exceed the second threshold. The probability is $P_a P_{b4}$.
2. The first pulse of the pulse packet exceeds the first threshold, but the next four integrated pulses fail to exceed the second threshold. That leaves two pulses. The sixth pulse can exceed the first threshold and the seventh pulse can exceed the second threshold. This probability is $P_a (1-P_{b4})P_b$.
3. The first pulse fails to exceed the first threshold, but the next pulse exceeds it and the succeeding four integrated pulses exceed the second threshold. This probability is $(1-P_a) P_a P_{b4}$.
4. The first two pulses fail to exceed the first threshold but the next pulse exceeds it and the succeeding four pulses exceed the second threshold. This probability is $(1-P_a)^2 P_a P_{b4}$.

Thus the joint probability of an alarm for a given S/N is

$$P = P_a P_{b4} + P_a P_{b1} (1-P_{b4}) + (1-P_a) P_{b4} + (1-P_a)^2 P_a P_{b4}$$

$$= P_a P_{b1} (1-P_{b4}) + P_a P_{b4} [1 + 1 - P_a + (1-P_a)^2]$$

It has been assumed thus far that the input pulses are constant amplitude pulses. To take into account scintillation of the target echo, it will be assumed that the target echoes are exponentially distributed.

The joint probability of an alarm as a function of S/N assuming target echo scintillation is shown in figure 14.

It has further been assumed that the percentage of time that the second detector has been integrating noise is negligible.

The cumulative probability of detection for the automatic alarm circuit is shown on figure 15. Two cases are considered: range separation between scans equal to 0.4 n.m. and 1.2 n.m. Extrapolation of AN/APQ-64 flight test results to those conditions gives the following detection ranges for comparison purposes. The idealized range is 40 n.m. These are for pilot operator detection rather than automatic alarm.

Range Separation Between Scans	Cumulative Probability of Detection	Detection Range (Pilot Operation)
0.4 n.m.	85%	25.1 n.m.
0.4 n.m.	50%	27.4 n.m.
1.2 n.m.	85%	21 n.m.
1.2 n.m.	50%	24.3 n.m.

(These detection ranges assume that the target lies within the area scanned)



For Soan Probability for Automatic Alarm

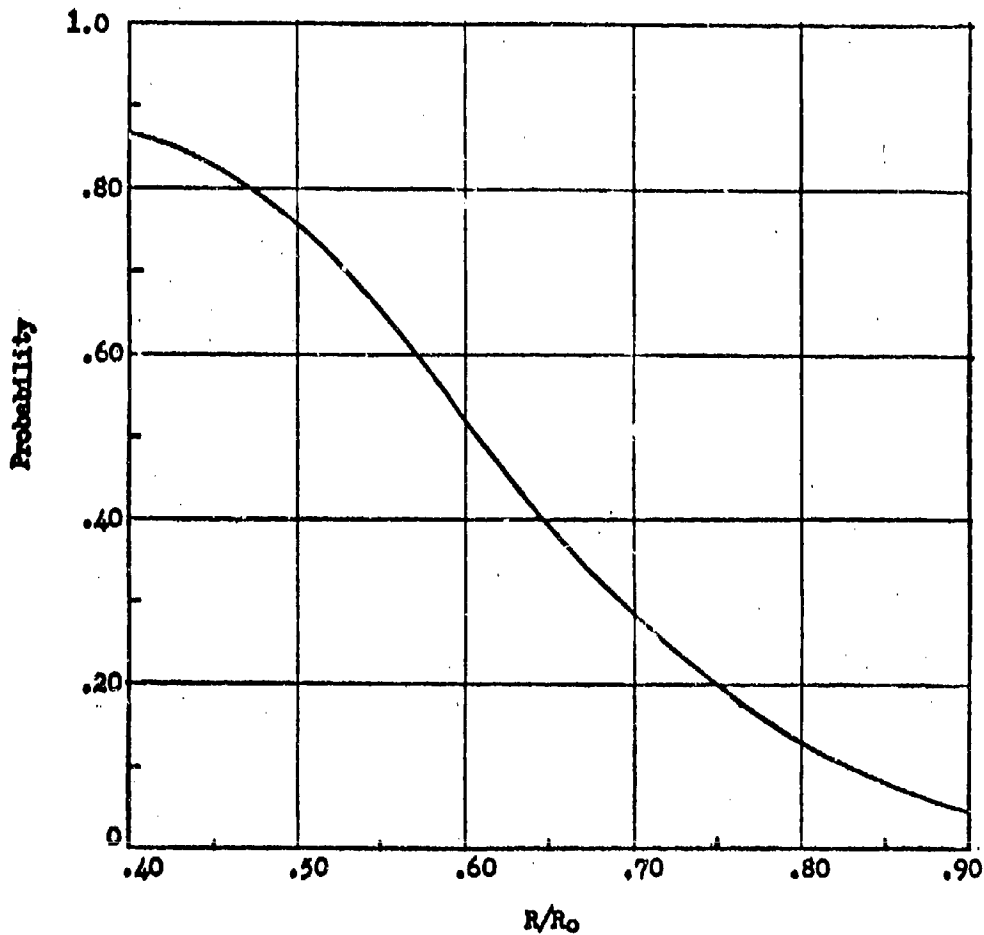


Fig. 14



Automatic Alarm Operator
Detection Capability
(By Distance)

$$d_0 = 40 \text{ n.m.}$$

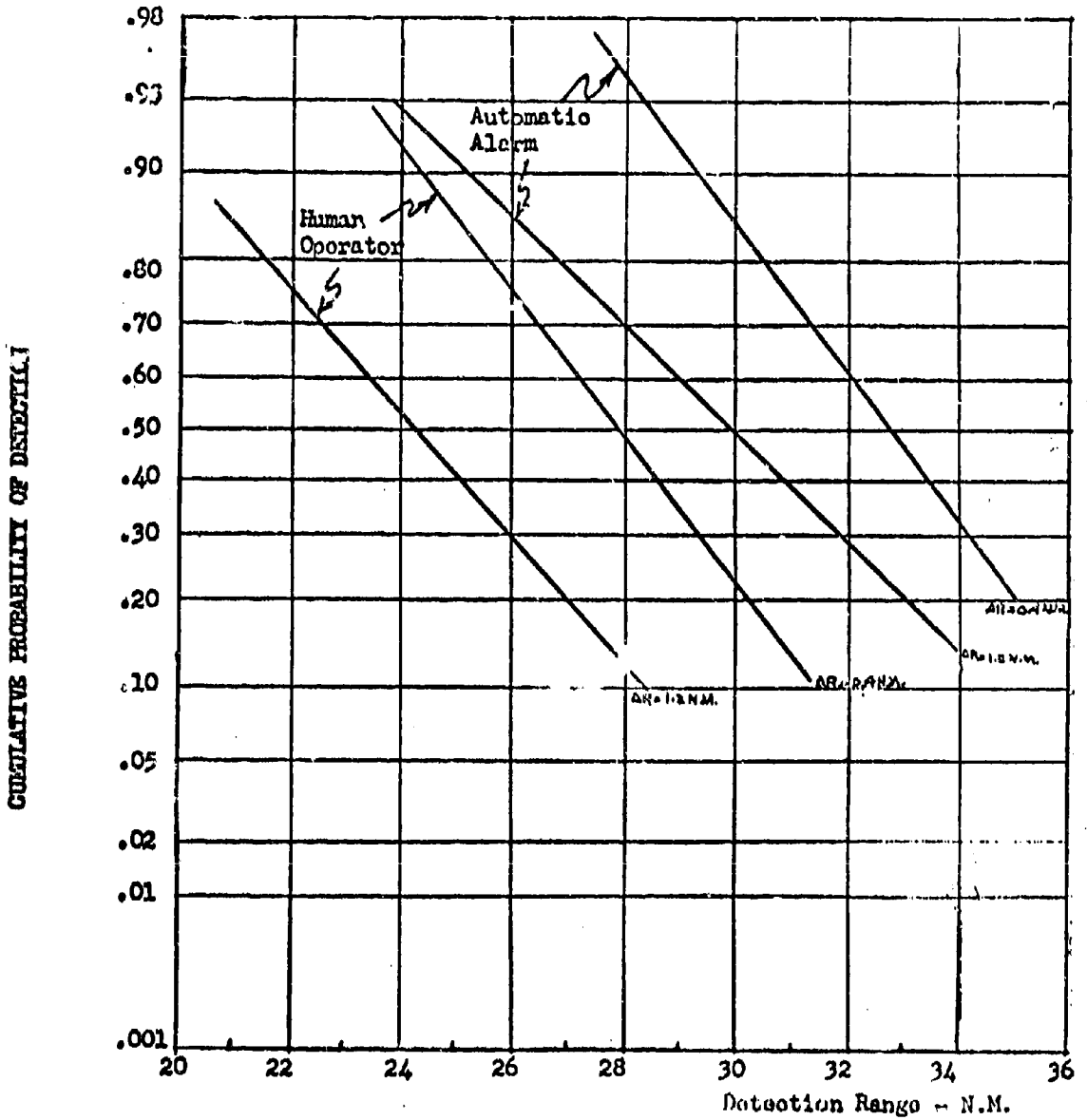


Fig. 15



It can therefore be concluded that in a clutter-free environment, the detection ranges attainable with automatic alarm will exceed that attainable by pilot operation.

The clutter rejection circuit of the proposed automatic alarm system will reject clutter whose width exceeds twice the transmitted pulse. Good clutter rejection is therefore attainable for homogeneous clutter. However discrete clutter returns will be passed by the system. Of particular concern is the altitude line and STAE clutter. Both of these are discrete clutter returns. Flight tests of the AN/APQ-50 reveal that the altitude line is approximately 1-2 times as wide as the transmitted pulse. These tests (Reference 4) were made for a 0.5 usec pulsewidth, but since the illuminated ground (or sea) area is proportional to pulsewidth, the same altitude line width dependence on transmitted pulsewidth holds for the wide pulse (1.75 usec). The altitude line is characterized by a sharply defined leading edge and an approximately exponential decay from its peak amplitude. The trailing edge will have more or less hash superimposed on it depending on the type of terrain or the sea state. The altitude line width measurements are at a point when its amplitude is 37% of its peak. Table II lists the altitude line measurements made with the AN/APQ-50.

Table II - Altitude Line Measurements

(Flight Test Data)

Altitude = 20,000 ft.

Antenna Angle (degree)	Peak Power (dbm)	Width (Fraction of Pulsewidth)
0	-72	.88
+20	-55	1.76
+44	-70	3.04
-20	-56	1.64
-40	-55	1.44

Altitude = 10,000 ft.

0	-60.5	2.26
+20	-34.5	1.12
+44	-65.5	1.53
-20	-50	1.12
-40	-55	1.44

Altitude = 5,000 ft.

0	-52.5	1.83
+20	-32.5	1.68
+44	-56	1.88
-20	-56	1.29
-40	-57	1.1

As stated previously, the false alarm time for the primary detector is 0.1 seconds. The threshold level for the primary detector can be determined from the approximate relationship

$$N \left(\gamma_b - N \cdot P_0 \right) \approx \frac{1}{n} \approx \frac{1}{3.35 \times 10^4}$$

where: N = Number of pulses integrated
 γ_b = Bias level
 P_0 = Probability that noise alone will not exceed the bias level
 n = Total number of noise variants in a false alarm time

This equation is derived in reference 5. For the primary detector,

$$\begin{aligned} N &= 1 \\ P_0 &= 0.5 \\ n &= 3.35 \times 10^4 \end{aligned}$$

Hence the bias level, $\gamma_b = 8$ db
 The average noise power = $NFKT\Delta f$
 For the APQ-72, $NF \approx 10.5$ db
 $\Delta f \approx 1.2$ mcps

Hence the average noise power ≈ -104 dbm. From the flight test data, it can be expected that altitude line signals will be passed by the pulsewidth discriminator and the automatic alarm circuits. Conceivably, the problem of the altitude line causing alarms can be eliminated by gating out the altitude line. The entire clutter picture can be considerably eased by flying the fighter at a lower altitude than the target. Whether tactics should be altered to ease a radar problem is beyond the scope of this memo.

Since much clutter encountered in a detection problem will be of a discrete nature, the usefulness of automatic alarm is of dubious quality unless some means of eliminating discrete clutter can be found.

V. Improved Receiver Noise Figure

The overall receiver noise figure is given by

$$NF = L_x (t_x + IF_{NF} - 1) + L_o$$

where L_x = Crystal conversion loss
 t_x = Crystal noise ratio
 IF_{NF} = IF noise figure
 L_o = Duplexer losses

The overall receiver noise figure is determined primarily by the crystal of detector. The 1N230 crystal which is used in the AN/APQ-50 has values of L_x and t_x of 6 db and 2.0 (ratio) respectively. For representative IF noise figures and duplexer losses of 1.5 db and 0.7 db respectively, the overall receiver noise figure is 10.5 db. Improvement in receiver noise figure can be attained by using the 1N23F or the 1N23E (not available in quantity at present) crystals. Comparative receiver noise figures attainable with these crystals are tabulated below



Noise Figure Estimates by Crystal Manufacturer

<u>Crystal</u>	<u>L_x</u>	<u>t_x</u>	<u>Receiver Noise Figure</u>	
1N23C	6.0 db	2.0	10.5 db	IFNF = 1.5 db
1N23D	5.0 db	1.7	8.9 db	L _D = 0.7 db
1N23E	4.8 db	1.3	7.8 db	

The present AN/APQ-72 has an average noise figure of 10.7 db. Measurements of the comparison between the 1N23C and 1N23E crystals leads to an estimate of 8.5-9.0 db (average) attainable with a redesigned front end. CW injection losses would add an approximate 1.6 db loss in noise figure. In addition the losses due to the isolator would come to approximately 0.5 db. The average noise figure for the improved receiver including losses due to CW injection and the isolator would therefore be approximately 10.5-11 db.

VI. Bandwidth Switching

Present plans call for a reduction in the IF bandwidth from the present 4 mcps to 1-1.2 mcps in search. Improvement in detection range arises from the resultant decrease in noise power. Not all of this improvement is realized in detection range since IF bandwidth reduction was accomplished at the cost of a reduction in the visibility factor. The net improvement in detection range would therefore be by a factor of

$$\frac{f(\Delta f_2)}{f(\Delta f_1)} \left[\frac{\Delta f_1}{\Delta f_2} \right]^{1/4} = 1.16$$

VII. Optimized Display

NEL estimates that the detection range improvement that would result from optimizing the scope presentation would be on the order of 0.5 db in range.

VIII. Fair Weather Detection Range

The search parameters of the AN/APQ-72 will be:-

Peak Power (at the directional coupler) = P = 200,000 watts
 Dish Diameter = D = 24 inches
 Wavelength = λ = 3.2 cm
 Pulse Repetition Frequency = PRF = 550 pps
 Pulsewidth = τ = 1.75 usec
 IF Bandwidth = 1.2 mcps
 Receiver Noise Figure = 10.5 db
 Losses = 0.7 db
 Field Degradation = 10 db
 Scan Type: 3 bar Palmer Scan - 33.6° x 11.8°
 Azimuth Scanning Rate = ω = 100 degrees/sec.

CONFIDENTIAL



The idealized range is 38 n.m. The detection range contour (85% cumulative probability of detection) against a B-47 type target is shown in Figure 16. The search pattern was optimized for the nose-on case.

References:

1. Marcum - "A Statistical Theory of Target Detection by Pulsed Radar"
2. AA-1140 - "Final Report, Detection Range - Phase I - AN/APQ-64
Flight Test Program"
3. ANTM-25 - "Revised Radar Range Report"
4. Flight Test Report #7
5. AA-1006 - "Detection Probability With a Square Law Detector"

CONFIDENTIAL

CONFIDENTIAL



AN/APQ-72 DETECTION RANGE (85% CUMULATIVE PROBABILITY)
FAIR WEATHER, NO CLUTTER, NO E.C.M.

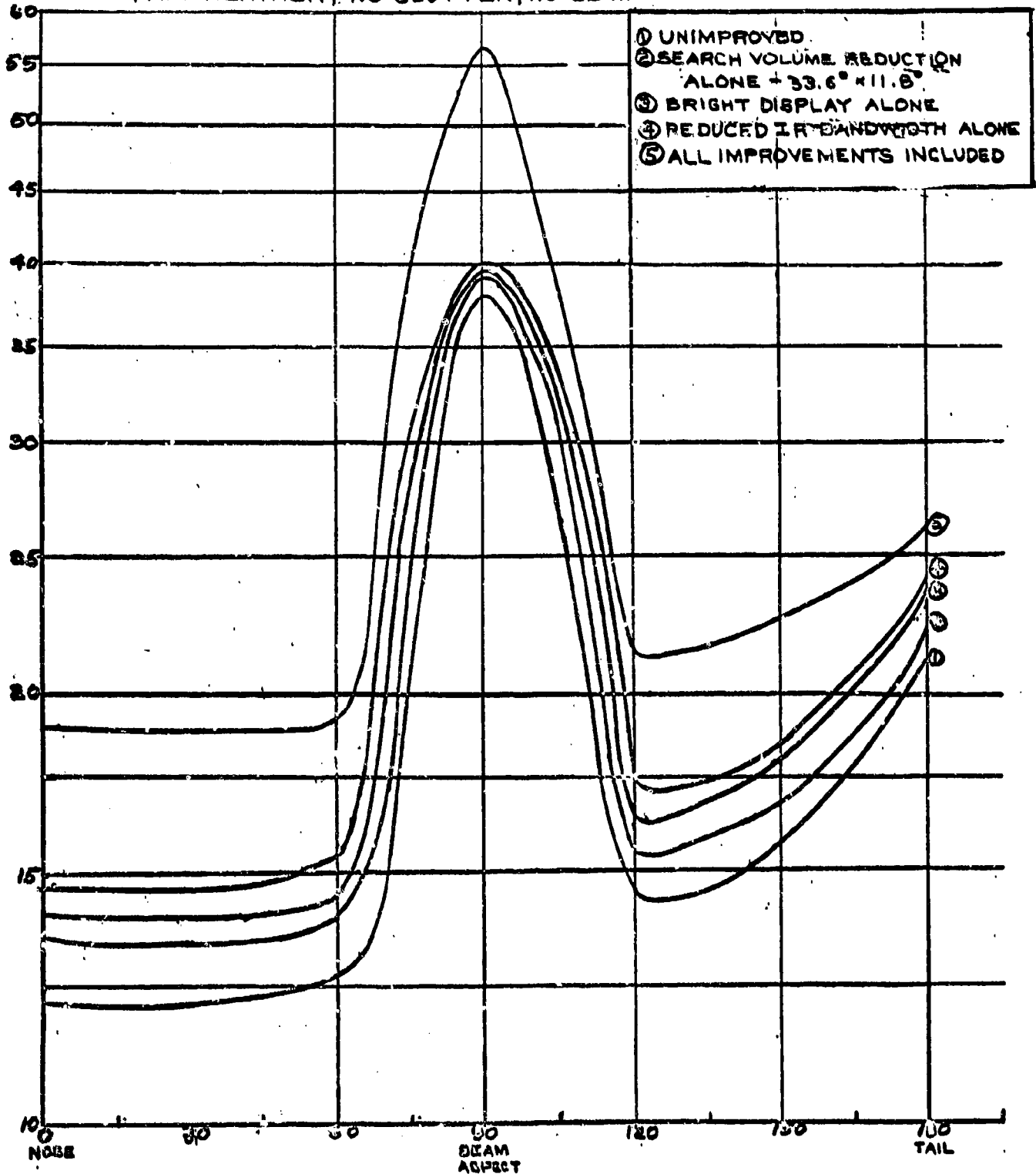


FIGURE 16

CONFIDENTIAL

**Naval Research Laboratory
Technical Library
Research Reports Section**

DATE: February 26, 2001
FROM: Mary Templeman, Code 5227
TO: **Code 5300 Paul Hughes**
CC: Tina Smallwood, Code 1221.1 *ts 3/8/01*
SUBJ: Review of NRL Reports

Dear Sir/Madam:

1. Please review NRL Report MR-754 Volumes I, II, III, IV, VII, VIII, IX, X, XI, XII, XIII, XIV, XV, MR-1372 and MR-1289 for:

- Possible Distribution Statement
 Possible Change in Classification

Thank you,



Mary Templeman
(202)767-3425
maryt@library.nrl.navy.mil

The subject report can be:

- Changed to Distribution A (Unlimited)
 Changed to Classification _____
 Other:


Signature

3-8-01
Date

** MAY CONTAIN EXPORT CONTROL DATA **

03/8/101
Page 1

Record List

AN (1) AD- 367 907/XAG
FG (2) 010100
010303
160401
170900
CI (3) (U)
CA (5) NAVAL RESEARCH LAB WASHINGTON D C
TI (6) SUMMARY OF NAVY STUDY PROGRAM FOR F4H-1 AND F8U-3 WEAPON SYSTEMS. VOLUME II.
APPENDICES.
DN (9) Memo. rept.
RD (11) 01 May 1957
PG (12) 136 Pages
RS (14) NRL-MR-754-VOL-2-APP
RC (20) Unclassified report
NO (21) See also Volume 9, AD-345 945.
AL (22) Distribution: DoD only: others to Naval Research Lab., Washington, D.
C.20390.
DE (23) (*jet fighters, naval research)
performance(engineering), data (u) stability, aerodynamic characteristics,
airspeed, altitude, force(mechanics), moments, equations of motion, angle of
attack, air to air missiles, drag, lift, maneuverability, aerodynamic loading,
thrust, climbing, interception, range(distance), time, guided missile
trajectories, aircraft fire control systems, search radar, radar tracking
DC (24) (U)
ID (25) an/apq-72, f-4 aircraft, sparrow
IC (25) (U)
DL (33) 04
CC (35) 251950

APPROVED FOR PUBLIC
RELEASE - DISTRIBUTION
UNLIMITED